Inelastic Photoproduction of J/ψ Mesons at HERA

David John Lamb

Thesis submitted for the degree of

Doctor of Philosophy

School of Physics and Space Research
Faculty of Science
University of Birmingham

June 2001

Abstract

Inelastic charmonium production has been an active area of theoretical and experimental interest over the past decade. Experimental results for charmonium production at the Tevatron collider disagreed with the predictions of the existing model (known as the Colour Singlet model) by more than order of magnitude. This stimulated the development of a new model (known as the Colour Octet model) which included additional production mechanisms. Despite explaining the Tevatron results, doubts about the universality of the new model remain and it needs to be tested in different physics processes.

An analysis of the inelastic photoproduction of J/ψ mesons in electron-proton collisions at the HERA collider is presented in this thesis. The data was recorded using the H1 detector and correspond to an integrated luminosity of 20.81 pb^{-1}. Measurements of the cross-sections and differential cross-sections in the inelasticity variable, z, and transverse momentum of the J/ψ squared, $p^2_{t,J/\psi}$, are presented in two kinematic regions. Previous preliminary results are confirmed, the kinematic range covered is extended, and comparisons with the predictions of both the old and new models are made.

A note on the author's contribution

Whilst this thesis is entirely written by myself, the collaborative nature of experimental high-energy physics is such that the work presented would not have been possible without the input of very many people from the H1 collaboration. This section serves to highlight the contribution I have made to the H1 collaboration during my PhD.

The analysis of inelastic J/ψ production presented here is entirely my own work. Several tools used in the analysis (e.g. the muon identification software) already existed and in all cases some optimisation was performed.

In addition to the work presented here, I also participated in the 1998, 1999 and 2000 data taking runs. I was part of a team responsible for the maintenance and running of the Forward Muon Detector. I had particular responsibility for maintaining the quality of the data recorded by this detector component.

Between October 1997 and September 2000, this work was supported financially by the UK Particle Physics and Astronomy Research Council (P.P.A.R.C.).

A Note on Units

In this work, a system of natural units will be used, whereby $\hbar = c = 1$

Acknowledgements

I would first like to thank PPARC and the Particle Physics group at the University of Birmingham for the wonderful opportunity they have given me in allowing me to work on the H1 experiment. I would like to thank several people without whom my time would not have been as productive or enjoyable. Firstly, my supervisor Dr Ian Kenyon who has been consistently helpful and supportive and has provided many useful insights. The various Birmingham post-docs have all been helpful. Dr Paul Newman has always made time to help when asked and the cricket wasn't on. Dr Lee West and Dr Paul Sutton gave me a good introduction to both the working and social life in Hamburg. Their places were taken by Dr Eram Rizvi and Dr Paul Thompson, who have continued the good work.

The H1-UK group provided a good, cooperative working environment in Hamburg. The sharing of ideas and problems enabled much more to be achieved. Particular thanks for this should go to Dr's Mehta, Heinemann, Phillips and Waugh as well as the Birmingham post-docs and the various students that were members of the H1-UK group. The Heavy Flavours working group provided an opportunity for regular scrutiny of my work. Without this regular input, my work would have suffered. Members of the group who were particularly helpful included Chris Hilton, Daniel Pitzl, Ralf Gerhards, Yorgos Tsipolitis, Beate Naroska and Katja Krueger.

A large thank you must go the Dr Michael Kraemer. He has been very helpful and was always willing to answer any questions on the theory that I had, no matter how basic they were. He was very kind in allowing me to use the results of his calculations prior to their forthcoming publication in ‘Progress in Particle and Nuclear Physics’.

My fellow students deserve particular thanks for either putting up with me or, occasionally, being helpful. Jon (who’s worked out how the economy works), Glen, Mike and Dan (none of whom have yet) made Hamburg fun. The Zeus-UK group (Alex, Rod, Dave, Eileen, Gavin and co.) took up the cause of their experiment and attempted to sabotage my work with many long nights out around Hamburg. They were partly successful and my bank manager would now like a word with them. Thanks also to the many Birmingham students (Alun, Giorgio, Mike, Paul, Carrie, Yves, Yves and Ethan).

Many friends have made me aware that there is life outside physics. Steve (who just found the title funny) and John (who took even longer to do his) not only lived with me for the first year but were stupid enough to let me move back in when I returned from Hamburg! Thanks also to: the Zoo boys, Mark ’Tory Boy’ Hill (good work with the election), Sam, Mark D, Mark G, and Andy (we’ve suffered together). Thanks to Anne and George for being there and brightening up the last few months. Finally, thanks to my parents and family for their support over the years.

Contents

List of Figures

List of Tables

Chapter 1

Introduction

The field of Particle Physics is the study of matter at its most fundamental level. The goal is a full understanding of the basic constituents of matter and their interactions. The *Standard Model* of particle physics has proved remarkably successful in this for over two decades. It successfully explains all the fundamental interactions, with the exception of gravity, and has passed the tests posed by numerous experiments. Only a few minor deviations from the expectations have been found, all at the level of a few standard deviations or less.

It was therefore somewhat surprising that the production of Charmonium in hadronic interactions proved difficult to incorporate into the theory. Charmonium is a bound state of charm and anti-charm quarks and, at first glance, would appear to pose no significant difficulties due to the heavy mass of the charm quark. However, the cross-section for the production of Charmonium at large transverse momentum, in protonantiproton collisions at the Tevatron collider, was found to be more than an order of magnitude greater than predictions. The predictions were based on the *Colour Singlet* model which was previously thought to describe Charmonium production successfully.

A new theoretical approach, within the Standard Model, was proposed by Bodwin, Braaten and Lepage. This placed the theory of Charmonium production on a more solid basis and used a new factorisation formalism based on non-relativistic Quantum Chromodynamics (NRQCD), an effective field theory formalisation of Quantum Chromodynamics (QCD) in which the quarks are treated non-relativistically. In contrast to the Colour Singlet model, this approach includes colour octet mechanisms and so has become known as the *Colour Octet* model.

The Colour Octet model successfully explains the Tevatron data and can be applied to Charmonium production in many different processes. One such process is the inelastic photoproduction of J/ψ mesons in electron-proton collisions at the HERA collider. The Colour Octet model contains several free non-perturbative parameters which are the matrix elements describing the transition of a charm-anticharm pair to the bound state of the J/ψ mesons. These cannot be calculated at present but can be extracted from the experimental data. Therefore, the measurement of Charmonium production cross-sections in several different processes would provide a crucial test of the universality of the Colour Octet model.

This thesis presents a study of the inelastic photoproduction of J/ψ mesons at the electron-proton collider, HERA. The analysis is split into two regions, defined in terms of the inelasticity variable z, which is the fraction of the photon energy transfered to the

J/ψ in the proton rest frame. The medium-z analysis covers the region $0.3 < z < 0.9$, which has mostly been investigated previously. This thesis investigates this region in more detail, with more data, and over a larger $W_{\gamma p}$ range than previously. The low-z analysis covers the range $0.07 < z < 0.45$, a region for which no results existed when this thesis was started. Since the work on which this thesis is based was started, one set of preliminary results has become available in this region [1].

The structure of this thesis is as follows: An overview of the general theoretical background is given in chapter 2. This includes a detailed description of the Colour Singlet and Colour Octet models, and a discussion on the current experimental and theoretical situation.

Chapter 3 presents a description of the HERA accelerator and the H1 detector. The major detector components and the trigger system are presented in detail.

The procedure for selecting and identifying J/ψ's produced inelastically in photoproduction events is presented in chapter 4. The J/ψ's are identified via the muonic decay $J/\psi \to \mu^+\mu^-$. Hence a detailed description of the procedure for identifying muons is presented. Additionally, the crucial process of triggering is discussed.

The reconstruction of the event properties and kinematics is presented in detail in chapter 5. Reconstruction is of vital importance because the measurement is made as a function of and in regions defined by the event kinematics. Furthermore, a discussion of the choice of kinematic regions for the measurements is presented.

Chapter 6 presents a crucial step of the analysis - the correction of the data. This is a necessary step in order to convert raw numbers into an accurate measurement. A discussion of the measurement of the various efficiencies and acceptances is presented. The measurements are made using both data events and Monte Carlo simulations of the events. Monte Carlo methods are used to correct the data and the determination of the various correction factors necessary in order to make the Monte Carlo simulations agree with the data is described. Finally systematic effects are discussed and the systematic errors evaluated.

The results of the medium-z analysis are presented in chapter 7, with the results of the low-z analysis presented in chapter 8. The results are compared with predictions from the Colour Octet model at leading-order, and the Colour Singlet model at leading-order and next-to-leading order.

The final chapter summarises the results and conclusions of the thesis.

Chapter 2

Theoretical Background

The use of scattering experiments to probe the structure of matter has a long history. Since Rutherford's famous experiment [2], in which the measurement of the angular distribution of α particles scattered off gold atoms led to the discovery of the atomic nucleus, probes of ever higher energy have been used to investigate the structure of matter in ever greater detail, yielding new insights with each new experiment. In particular, electron-proton scattering has led to important new insights. For example, the first direct experimental evidence for sub-structure within the proton was provided by electron-proton deep inelastic scattering at SLAC [3]. The HERA experiment has taken electron-proton scattering into new kinematic regions, probing the structure of matter down to distances as small as $\sim 10^{-18}$ m. This chapter will give a brief overview of the general theoretical background to physics at HERA, followed by a more detailed description of the theoretical background for inelastic J/ψ production at HERA.

2.1 The Standard Model

The *Standard Model* of particle physics was developed in the last half of the twentieth century. It is a set of gauge theories, based on *Quantum Field Theory*, which successfully describe all the known elementary particles and their interactions (excluding gravity) within a single theoretical framework. The known elementary particles are split into three groups: *Quarks*, *Leptons* and *Gauge Bosons*. There are six flavours of quarks (up, down, strange, charm, bottom and top), six leptons (electron, electron neutrino, muon, muon neutrino, tau and tau neutrino) and five gauge bosons (photon, $W^{\pm}$, Z^0 and the gluon). The quarks and leptons can be grouped together into three generations, each a heavier version of the previous, and each containing two quarks (e.g. up and down) and two leptons (e.g. electron and electron neutrino). The interactions included in the Standard Model are the electromagnetic, weak and strong forces. The electromagnetic and weak interactions unify at high energy and are described by a gauge theory known as the *Electroweak Theory* [4]. The strong interaction is described by a gauge theory known as *Quantum Chromodynamics* (QCD) [5]. The forces are mediated by the exchange of virtual Gauge Bosons. For the electromagnetic interaction the exchanged gauge boson is the photon (γ), in the weak interaction it is the $W^{\pm}$ or Z^0, and in the strong interaction it is the gluon (g).

The quark structure of matter was revealed via two sources of experimental information: Hadron Spectroscopy and Deep Inelastic Scattering. Many strongly interacting particles, known as hadrons, were discovered and their masses and quantum numbers could be grouped in a spectroscopic manner. The structure of hadron spectroscopy can be explained by invoking substructure in the form of quarks [6]. Deep Inelastic Scattering at SLAC unambiguously revealed substructure within the proton [3]. The experimental results were consistent with the proton containing point-like objects. These were called partons. It was subsequently shown that the quarks and the partons are the same object. Within the Standard Model, hadrons are modelled as either a bound three quark (qqq) state (baryons) or a bound quark-antiquark ($q\bar{q}$) state (mesons). The Quark-Parton Model (QPM) [7, 8] views the quarks as non-interacting spin-1/2 particles. Within QCD, the quarks interact and they cannot be seen in isolation because they carry *colour charge*, leading to strong inter-quark forces. QCD describes the colour force (i.e. the force between particles carrying colour charge) which increases with the distance of separation of two colour charged objects but decreases to zero as the separation decreases to zero. These extremes are known as *colour confinement* and *asymptotic freedom* respectively. The process by which quarks ejected from a hadron form bound states of observable particles is known as *Hadronisation.*

In the Standard Model, the proton is viewed as containing three valance quarks within a sea of gluons, quarks and antiquarks. The sea arises due to the exchange of gluons between the valance quarks, which can fluctuate into $q\bar{q}$ pairs of any species (sea quarks). Therefore, there is a distribution of all quark flavours and of gluons within the proton.

2.2 Deep Inelastic Scattering

The Deep Inelastic Scattering (DIS) process $ep \to e(\nu)X$, where X is anything, can be considered as taking place in two stages. Firstly, there is an elastic scattering between the electron and a parton[1] from within the proton. Secondly there is the hadronisation of the struck parton and the proton remnant, which occurs as a result of colour confinement. The DIS process involves an electroweak interaction between the electron and the struck parton. If the exchanged boson is neutral (i.e. a γ or a Z^0), the interaction is known as a Neutral Current (NC) interaction. If it is charged (i.e. a $W^\pm$), it is known as a Charged Current (CC) interaction. The DIS cross-sections depend on the electron-parton elastic scattering cross-sections and the partonic content of the proton, which is expressed in terms of structure functions.

2.2.1 HERA Kinematics

A schematic diagram of a deep inelastic electron-proton (e-p) interaction is shown in figure 2.1. The incoming electron emits a gauge boson (either a γ, Z^0 or $W^\pm$) which then interacts with a parton from within the proton to produce the hadronic final state. The interaction $ep \to e(\nu)X$ can be described by two independent Lorentz invariant scalars Q^2 and x. Q^2 is given by

$$Q^2 \equiv -q^2 = -(k - k')^2, \tag{2.1}$$

---

[1] parton will be used to refer to a constituent of the proton, i.e. a quark or gluon.

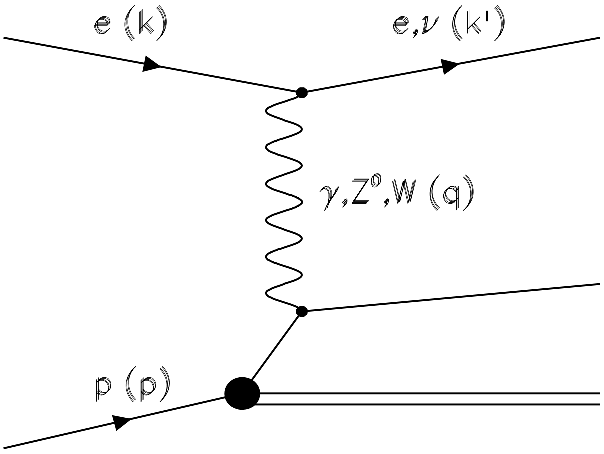

Figure 2.1: *Schematic diagram for deep inelastic scattering. The particle types and their 4-momenta are indicated.*

where k and k' are the 4-momenta of the incoming electron and outgoing electron (or neutrino in CC interactions) respectively, and q is the 4-momentum of the exchanged gauge boson. Note that the exchanged gauge boson is virtual and so q^2 is negative. x is given by

$$x \equiv \frac{Q^2}{2P.q}, \tag{2.2}$$

where P is the 4-momentum of the incoming proton. In the Quark-Parton Model (QPM) [7, 8], x is Bjorken-x, the fraction of the proton's momentum carried by the struck parton. Another Bjorken scaling variable is y, given by

$$y \equiv \frac{P.q}{P.k}. \tag{2.3}$$

In the proton rest frame, y is the fraction of the incoming electron's energy transferred to the hadronic final state and so is often known as the inelasticity variable. At HERA, the particle masses are small compared with the beam energies and can therefore be neglected. Neglecting masses, these three variables are related by

$$Q^2 = sxy, \tag{2.4}$$

where s is the centre-of-mass energy squared of the interaction, given by

$$s \equiv (k + P)^2 \simeq 4E_eE_p, \tag{2.5}$$

where E_e and E_p are the electron and proton beam energies respectively, and the proton and electron masses have been neglected. Therefore, for fixed $\sqrt{s}$, only two of x, Q^2 and y are independent. The interaction can also be viewed as being between the exchanged gauge boson and the proton. The centre-of-mass energy, $W_{\gamma p}$, of this interaction is given by

$$\begin{aligned} W_{\gamma p}^2 &= (P + q)^2 \\ &= Q^2(\frac{1}{x} - 1) + m_p^2 \\ &= ys - Q^2 + m_p^2, \end{aligned} \tag{2.6}$$

where m_p is the mass of the proton.

A useful variable is rapidity, η, which is a measure of the polar angle of a particle. It is defined as

$$\eta = \frac{1}{2} \ln \left(\frac{E + p_L}{E - p_L} \right), \tag{2.7}$$

where E is the energy of the particle, and p_L is the longitudinal component of the particle's momentum. Rapidity is particularly useful because it only changes by a constant when undergoing a Lorentz boost along the interaction axis. Therefore, the difference between the rapidity of two particles is a Lorentz invariant quantity.

2.2.2 Deep Inelastic Scattering Cross Section

The Born cross-section for the interaction shown in figure 2.1 can be expressed in terms of a propagator term and two structure functions, $F_1(x, Q^2)$ and $F_2(x, Q^2)$. The structure functions describe the partonic structure of the proton. For the neutral current process, the Born cross-section is given by

$$\frac{d^2\sigma}{dxdQ^2} = \frac{4\pi\alpha^2}{xQ^4}\Big[y^2xF_1(x, Q^2) + (1-y)F_2(x, Q^2)\Big], \tag{2.8}$$

where $\alpha = e^2/4\pi$ is the fine structure constant. In the Quark-Parton Model the structure functions are functions of x only, an effect first predicted by Bjorken and now known as *Bjorken scaling* [9]. They are also related by the Callan-Gross relation $F_2 = 2xF_1$ [10], which is a direct consequence of the QPM assuming the proton consists of point-like non-interacting massless spin-1/2 particles. These features (Bjorken scaling and agreement with the Callan-Gross relation) were observed in early e-p experiments [3] and provided the crucial evidence for the existence of point-like particles within the proton.

Quantum Chromodynamics (QCD), the gauge theory of the strong interaction, de-

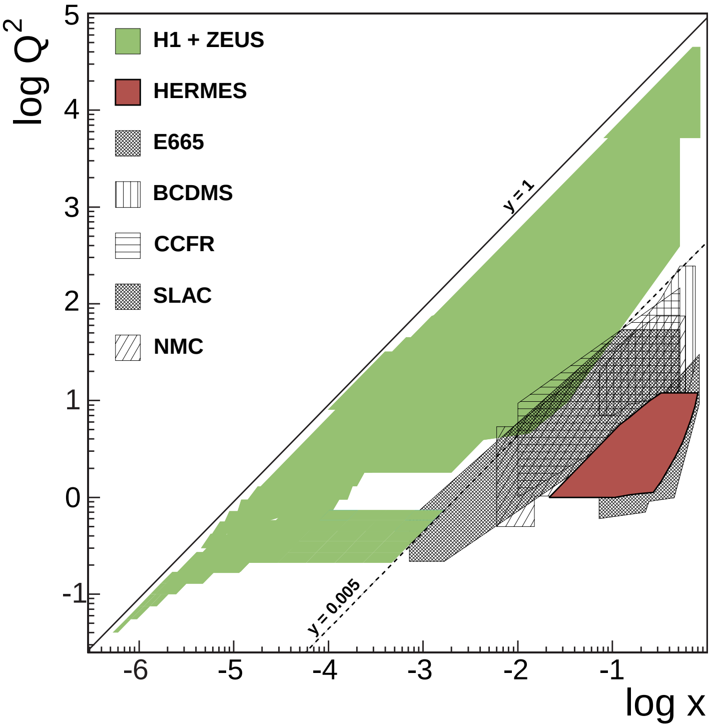

Figure 2.2: *Kinematic region covered by the HERA experiments (H1, ZEUS and HERMES) and previous fixed target experiments. The line $y = 1$ represents the kinematic limit for H1 and ZEUS. The plot illustrates how HERA has extended the kinematic region covered by two orders of magnitude in x and Q^2, compared with previous fixed target experiments.*

scribes how the partons interact. QCD predicts a slow evolution of the structure functions with Q^2, an effect which is known as *scaling violations*, and the violation of the Callan-Gross relation. The violation of the Callan-Gross relation requires the introduction of the longitudinal structure function $F_L(x, Q^2)$, given by $F_L = F_2 - 2xF_1$. The Born cross section can then be re-written as

$$\frac{d^2\sigma}{dxdQ^2} = \frac{2\pi\alpha^2}{xQ^4}\Big[(1 + (1-y)^2)F_2(x,Q^2) - y^2 F_L(x,Q^2)\Big]. \tag{2.9}$$

The evolution of the structure functions with Q^2 is parameterised in QCD by the

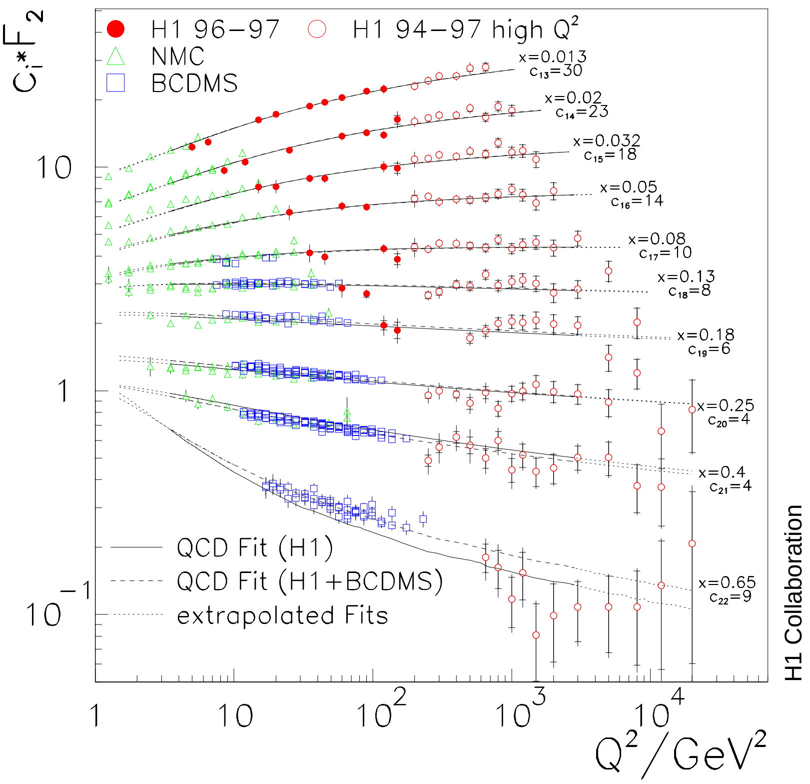

Figure 2.3: *Proton structure function $F_2(x, Q^2)$ as measured by H1 [12] and the fixed target muon-proton scattering experiments NMC [13] and BCDMS [14]. The curves are fits to the H1 data (solid lines) and the H1 and BCDMS data (dashed lines). Figure is taken from [12].*

evolution equations of Dokshitzer, Gribov, Lipatov, Altarelli and Parisi (DGLAP) [11]. Using the DGLAP equations, the structure function can be evolved to any value of x and Q^2 once the x dependence at one fixed value of Q^2 has been measured.

The centre-of-mass energy at HERA is an order of magnitude greater than previous fixed target experiments and this has opened up new kinematic regions of deep inelastic scattering. Figure 2.2 compares the Q^2 vs. x regions accessible to previous experiments and those accessible to the H1 and ZEUS experiments at HERA. HERA has extended the range covered by two orders of magnitude in Q^2 and x. The structure function $F_2(x, Q^2)$ has therefore been measured over a wide range of x and Q^2 by the H1 experiment. Figure 2.3 shows a sample of such measurements, in the region of relatively large x [12], and compares the results with previous measurements from fixed target muon-proton scattering experiments [13, 14]. The figure shows that Bjorken scaling is valid for $x \sim 0.1$, and that scaling violations occur away from $x \sim 0.1$. $F_2(x, Q^2)$ rises as x decreases, which can be attributed to the increasing gluon density as x decreases. The fits shown were performed using the QCD evolution mentioned previously, showing that the HERA data confirms the validity of QCD over a huge kinematic range.

2.2.3 Physics Processes at HERA

There are several different types of physics processes that can occur and are studied at HERA. Each has different characteristics which can be used to identify them and each can give a useful insight into proton structure and features of QCD. This section will give a brief overview of some of these processes.

High-Q^2 Deep Inelastic Scattering

As mentioned above, DIS events are classified into two types; Neutral Current ($ep \to eX$) and Charged Current ($ep \to \nu X$). The signature for a high-Q^2 neutral current (NC) event is an electron scattered through a large angle, whilst the signature for a high-Q^2 charged current (CC) event is missing transverse momentum due to the undetected neutrino (ν). The exchanged particle in a neutral current interaction is either a photon (γ) or a Z^0. Equations 2.8 and 2.9 are for photon exchange, and the propagator term has a $1/Q^4$ dependence as the photon is massless. The Z^0, however, is

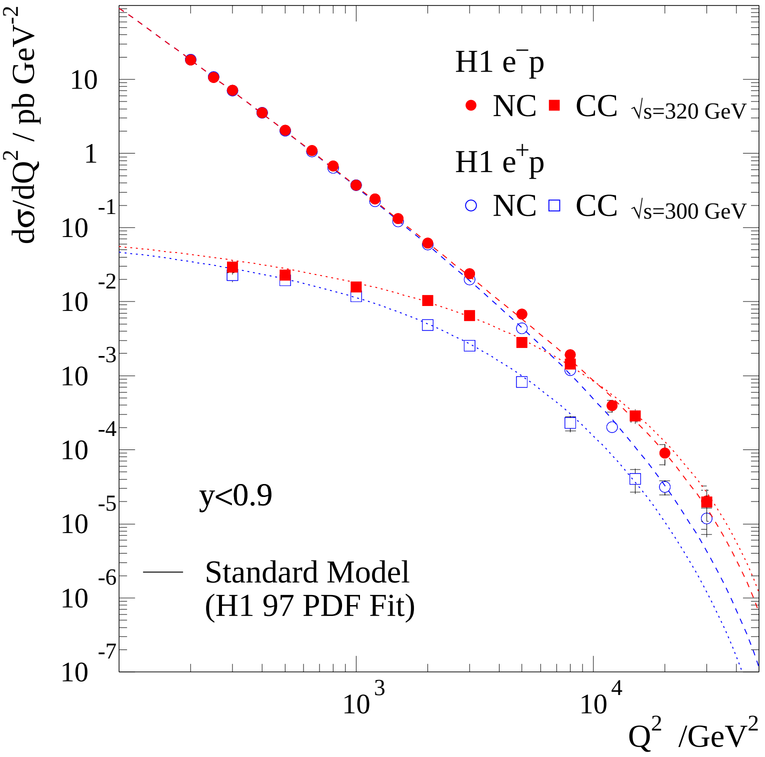

Figure 2.4: *The cross section $d\sigma/dQ^2$ for NC and CC scattering in electron-proton and positron-proton collisions. The plot shows the H1 measurements and theoretical predictions.*

massive, hence for Z^0 exchange, the propagator term has a $1/(Q^2+M_Z^2)^2$ dependence, where M_Z is the mass of the Z^0. The exchanged particle in a charged current interaction is the $W^\pm$ which is massive, and hence the propagator term has a $1/(Q^2+M_W^2)^2$ dependence, where M_W is the mass of the $W^\pm$. The CC events are therefore suppressed relative to NC events by a factor of order

$$\sim \left(\frac{Q^2}{Q^2+M_W^2}\right)^2. \tag{2.10}$$

Hence the CC cross-section is small compared to the NC cross-section until $Q^2 \sim M_W^2$. This has been confirmed experimentally [15], as shown in figure 2.4.

Diffraction

The simplest form of diffractive event is one in which the exchanged virtual photon converts to a real particle with the same quantum numbers, $\mathrm{J}^{\mathrm{PC}} = 1^{--}$, as the photon (e.g. a J/ψ or ρ meson, or a real photon) and the proton remains intact. (e.g. $ep \rightarrow eJ/\psi p$). In general, diffractive events are of the form $ep \rightarrow eXY$, where X and Y are two separate hadronic systems with a large gap in the rapidity distribution, of the particles in the event, between the two systems. One system (Y) originates from the proton (in the simplest form mentioned above, it is the proton) and the second (X) from the exchanged particle (in the simplest form, it could be a J/ψ, ρ or a photon for example).

The gap in the event's rapidity distribution indicates that there is little or no interaction between the two hadronic systems X and Y, and so they develop independently. Therefore, there must have been no net colour flow from the proton to the hadronic system X. Hence, a diffractive event is interpreted as the result of the exchange of a colour singlet object with the quantum numbers of the vacuum. This is commonly identified as the Pomeron. HERA data has led to a much improved understanding of the Pomeron and its partonic structure [16].

Photoproduction

The interaction of a real photon with the proton is known as photoproduction. That is, photoproduction interactions occur at low Q^2 ($Q^2 < \mathcal{O}(1\ \mathrm{GeV}^2)$), and the total

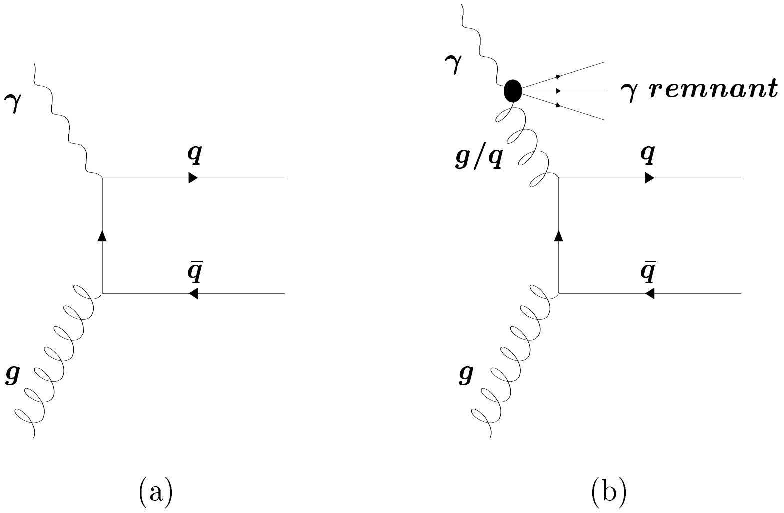

(a) (b)

Figure 2.5: *Schematic diagram of (a) direct and (b) resolved boson-gluon fusion.*

photoproduction cross-section is large due to the $1/Q^4$ term in the cross-section (see equations 2.8 and 2.9). A photoproduction interaction can be interpreted as a photon-proton (γ-p) interaction.

At HERA, photoproduction events where there is a hard scale (e.g. a high p_t jet or a heavy quark) are dominated by the *Boson-Gluon Fusion* (BGF) interaction. Q^2 and x are related by equation 2.4, hence low Q^2 implies that the event occurs at low x as well. The gluon content of the proton rises rapidly as x decreases [12], and hence the low x interactions are dominated by gluons. The photon can interact with the gluon in one of the two ways illustrated by figure 2.5. In (a) 'direct' photoproduction, the photon interacts with the gluon directly to produce the hadronic final state. In (b) 'resolved' photoproduction, the photon fluctuates into a hadronic state (e.g. a $q\bar{q}$ pair) and the gluon interacts with a parton from within the photon. Both types of interactions have been studied at HERA and have produced new insights into QCD, proton structure

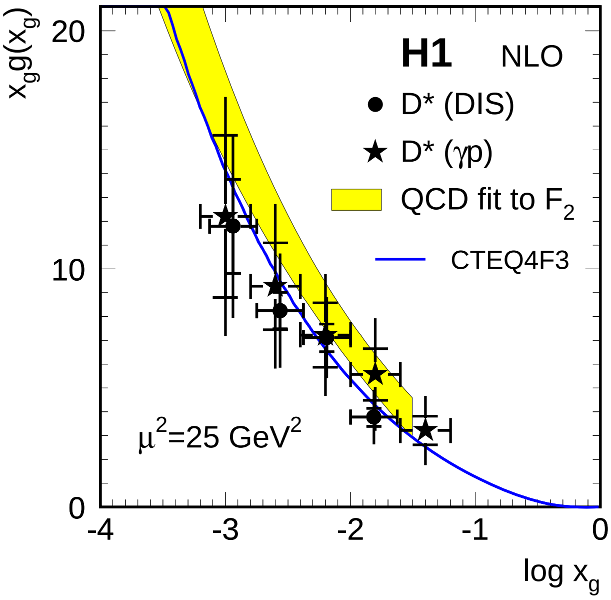

Figure 2.6: *Gluon density of the proton obtained from* D^* *meson production in DIS and photoproduction interactions [18]. The results are compared to the results from a QCD analysis of* $F_2(x, Q^2)$ *measurements [19] (light shaded band) and the CTEQ4F3 [20] parameterisation. The factorisation scale was* $\mu^2 = 25\ \mathrm{GeV}^2$.

and photon structure.

Heavy Flavour Production

Heavy flavour physics refers to the study of the production of the heavier quark flavours (i.e. c, b and t). Heavy flavour production provides a useful testing ground for QCD because the heavy quark mass sets the scale for the perturbative expansion of QCD calculations in terms of the strong coupling constant, $\alpha_s(m_q)$, thus making calculations reliable. At HERA, this has been restricted mainly to the study of charm, with first results on bottom production recently published [17]. Charm quarks have a mass of

$m_c \sim 1.3$ GeV and are therefore produced in large numbers at HERA. The study of bottom production is limited by low statistics due to its high mass ($m_b \sim 4.2$ GeV). The top quark is not accessible at HERA energies due to its large mass ($m_t \approx 174$ GeV).

Charm quarks can be produced, in $c\bar{c}$ pairs, in all the processes described above. The $c\bar{c}$ pair then either bind to form a meson such as a J/ψ, which is known as hidden charm production, or form separate charmed hadrons, known as open charm production. The dominant production method for charm is boson-gluon fusion. Hence, by studying charm production, the gluon content of the proton can be accessed directly. H1 has performed such a measurement by studying D^* production, and extracted the gluon content of the proton [18]. The result is shown in figure 2.6, where it is compared with an extraction from measurements of $F_2(x, Q^2)$ [19] and the parameterisation of the CTEQ4F3 parton density functions [20]. The results confirm the validity of the boson-gluon fusion picture and illustrate the consistency of gluon density extractions from this and other techniques.

Beyond the Standard Model

The HERA experiments investigate new regions of phase space and so it is wise to search for new phenomena or particles which would indicate the discovery of new physics. These searches have been performed and, although no new physics processes have been detected, many limits have been placed on new physics. For example, a search for quark sub-structure has revealed none with the present statistics, and placed an upper limit on the size of the light quarks of $R_q < 1.7 \times 10^{-18}$ m at 95%

confidence limit [21]. The most significant signal of possible new physics has been the observed excess, over standard model predictions, of events with a single isolated muon and missing transverse momentum [22]. It will be interesting to see what the HERA experiments observe after the forthcoming luminosity upgrade (see section 3.10).

2.3 J/ψ Production at HERA

2.3.1 Charmonium

The J/ψ particle was discovered independently by two separate experiments during 1974, in what is now known as the 'November Revolution' of particle physics. A narrow resonance in the invariant mass spectrum of e^+e^- pairs, produced in the interaction

$$p \; + \; Be \; \rightarrow \; e^+ \; e^- \; X,$$

was discovered at $m_{e^+e^-} \sim 3.1$ GeV by Aubert et. al. at Brookhaven [23]. At the same time, a resonance in the cross section for the interaction

$$e^+ \; + \; e^- \; \rightarrow \; \text{Hadrons},$$

was discovered at a centre-of-mass energy of $\sqrt{s} \sim 3.1$ GeV by Augustin et. al. at SLAC [24]. The SLAC experiment subsequently discovered a second resonance at $\sqrt{s} \sim 3.7$ GeV [25]. This marked the discovery of the charmonium family of particles, and the fourth quark flavour - charm.

The particle discovered with a mass $\sim$ 3.1 GeV was named the 'J' particle by the Brookhaven experiment and the 'ψ' particle by the SLAC experiment. It is now known as the J/ψ particle, and has been identified as the lightest vector meson in the charmonium family. Charmonium particles are bound states of a charm (c) and an anti-charm ($\bar{c}$) quark. The quantum numbers of the J/ψ can be determined from the production mechanism. As J/ψ's are produced in large numbers in e^+e^- annihilations, it can be concluded that the J/ψ has the same quantum numbers as the photon i.e. $\mathrm{J^{PC}} = 1^{--}$. The second resonance is now recognised as the first radial excitation of the J/ψ, the ψ(2S). Since the November Revolution, the detailed spectrum of charmonium states has been revealed.

The mass of the J/ψ particle is now known much more accurately. The current world average is [26]:

$$m_{J/\psi} \ = \ 3.09687 \pm 0.00004 \text{ GeV}.$$

An unusual property of the J/ψ is its extremely narrow decay width of [26]:

$$\Gamma_{J/\psi} \ = \ 87 \pm 5 \text{ keV}.$$

This is unusual because it is several orders of magnitude smaller than other typical hadronic decay widths. The narrow width indicates that the J/ψ must have a long lifetime and the 'easiest' decay channels must be heavily suppressed or forbidden. The most obvious decay channel would be into two charmed mesons (D mesons). However, the lightest D meson (the D^0) has a mass of $m_{D^0} = 1.865$ GeV and therefore this decay is forbidden due to energy conservation.

Any J/ψ decay involving the strong interaction must involve the charm and anti-charm quarks annihilating. This produces disconnected quark lines, which suppresses the decay according to the OZI rule [27]. Furthermore, any hadronic decay must involve at least three gluons due to the conservation of colour charge and C-parity.

Due to the above reasons, the electromagnetic decay channels of the J/ψ have significant branching ratios. The current world average for the branching ratios into e^+e^- and $\mu^+\mu^-$ is [26]:

$$\begin{aligned} BR(J/\psi \to e^+e^-) &= 5.93 \pm 0.10\% \\ BR(J/\psi \to \mu^+\mu^-) &= 5.88 \pm 0.10\% \end{aligned}$$

The narrow width and significant leptonic branching ratios make the J/ψ a very convenient experimental signal for the production of charm quarks in particle collisions.

2.3.2 Production Processes at HERA

Six papers have been published on the production of J/ψ and ψ(2S) mesons by the H1 collaboration [28]-[33]. The J/ψ can be produced in both deep inelastic scattering ($Q^2 \gtrsim 1$ GeV^2) and photoproduction ($Q^2 \sim 0$ GeV^2) events. In both cases, the J/ψ can be produced in both a *diffractive* and an *inelastic* way. In diffractive production, the hadronic final state contains just the J/ψ, in addition to the proton which either remains intact (elastic), or dissociates into a low mass state (proton dissociation). In inelastic production, the hadronic final state typically contains many other particles accompanying the J/ψ, and the proton dissociates into a high mass state. Inelastic production is described in the next section in the context of photoproduction, a description which is also valid for production in DIS events.

A useful variable for discriminating between the various production methods is the Lorentz invariant inelasticity variable z. This is defined in a similar manner to the Bjorken scaling variable y and is defined as

$$z \equiv \frac{p_{J/\psi}.P}{q.P}, \tag{2.11}$$

where $p_{J/\psi}$ is the 4-momentum of the J/ψ. In the proton rest frame, z is the fraction of the photon energy transferred to the J/ψ. Whilst there is some overlap, the different production mechanisms are dominant in different regions of z. Diffractive production where the proton remains intact occurs at $z = 1$ by definition. Diffractive production with proton dissociation dominates at $z \gtrsim 0.95$ and inelastic production dominates at $z \lesssim 0.9$. The details of the transition from diffractive to inelastic production is not well understood at present.

2.4 Theory of Inelastic Photoproduction of J/ψ's

This section presents the recent developments in and the current theoretical understanding of the inelastic photoproduction of J/ψ's. The description will follow a roughly historical order, beginning with the *Colour Singlet* (CS) model, then results on charmonium production at the Tevatron will be presented, the *Colour Octet* (CO) model will then be described, and finally recent experimental and theoretical developments are discussed.

2.4.1 Colour Singlet Model

The first model to make quantitative predictions for charmonium production in many physical interactions was the *Colour Singlet* model. Credit for the development of the model is difficult to ascribe as many physicists were involved in early work on it. The first use of the model in the photoproduction of charmonium was by Berger and Jones [34]. Other early uses included the analysis of the decay $Z^0 \rightarrow c\bar{c} + \gamma$ by Guberina et. al. [35], and inclusive charmonium production in e^+e^- annihilation by Keung and by Kuhn and Schneider [36]. For a review of the application of the Colour Singlet model see [37].

Within the Colour Singlet model the production of the charmonium particle is factorised into two stages: the production of a $c\bar{c}$ pair in a colour singlet state (i.e. a state with no net colour) and with the same quantum numbers as the charmonium, and the transition of the $c\bar{c}$ pair into the bound charmonium state. The amplitude for the first stage is given by a matrix element which describes the production of a $c\bar{c}$ pair in a short distance process of range $\sim 1/m_c$. The matrix element can be calculated reliably in perturbative QCD. The second stage contains all the non-perturbative dynamics involved in the formation of the bound state factorised into a single long distance factor.

In this formalism, the production cross section for the process $\gamma p \to J/\psi X$ can be written as [38]

$$d\sigma(J/\psi + X) \;=\; d\hat{\sigma}(c\bar{c}(\underline{1},{}^{3}\mathrm{S}_1) + X)|R_{J/\psi}(0)|^2, \qquad (2.12)$$

where $d\hat{\sigma}(c\bar{c}(\underline{1},{}^{3}\mathrm{S}_1) + X)$ is the cross-section for the production of a final state which includes a $c\bar{c}$ pair in a colour singlet state (denoted by $\underline{1}$, a colour octet state would be denoted by $\underline{8}$) and with the same quantum numbers as the J/ψ (in spectroscopic notation ${}^{2\mathrm{S}+1}\mathrm{L}_\mathrm{J} \;=\; {}^{3}\mathrm{S}_1$). This short distance part of the cross-section can be calculated using a perturbative expansion in terms of $\alpha_s(m_c)$. The long distance part is approximated by $|R_{J/\psi}(0)|^2$, where $R_{J/\psi}(0)$ is the radial wavefunction of the J/ψ at the origin. $R_{J/\psi}(0)$ can be determined from the electronic decay width of the J/ψ, Γ_{ee}, given at leading order by

$$\Gamma_{ee} \equiv \Gamma(J/\psi \to e^+e^-) \simeq \frac{4\alpha^2}{9m_c^2}|R_{J/\psi}(0)|^2. \qquad (2.13)$$

Equation 2.12 can be generalised and used to describe the inclusive production of any charmonium meson in any physical interaction. The short distance part becomes $d\hat{\sigma}(c\bar{c}(\underline{1},{}^{2\mathrm{S}+1}\mathrm{L}_\mathrm{J}) + X)$ where S, L and J are the quantum numbers of the charmonium meson. The long distance part is related to the L'th derivative of the radial wavefunction at the origin of the charmonium meson.

The Colour Singlet model has enormous predictive power. The cross-section can be calculated for any high energy physics process in terms of one non-perturbative parameter for each orbital angular momentum multiplet in the charmonium family, provided

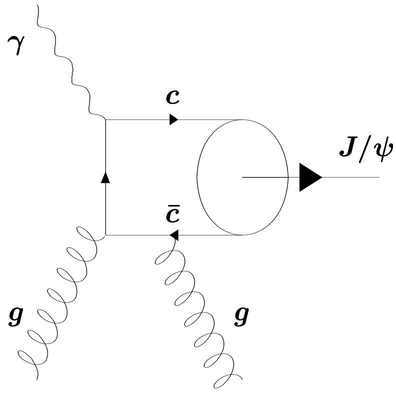

Figure 2.7: *Leading order diagram for the production of a* J/ψ *meson via boson-gluon fusion in the Colour Singlet model.*

the cross-section for $c\bar{c}$ production can be calculated. Moreover, this parameter can be determined from charmonium decays (see equation 2.13, for example). Despite this, it is only a model. There is no theorem that guarantees the factorisation used above is valid, and it is incomplete since it ignores colour octet $c\bar{c}$ states which could form a bound state via soft gluon emission.

The Colour Singlet model has been successfully applied to J/ψ production at HERA in the range $0.45 < z < 0.9$. The leading order process, shown in figure 2.7, is $\gamma g \to J/\psi g$, which is at $\mathcal{O}(\alpha\alpha_s^2)$. The final state gluon is required in order to produce a $c\bar{c}$ pair with the same quantum numbers as the J/ψ. Additionally, the gluon must have relatively high p_t (a "hard" gluon) in order to ensure the applicability of the perturbative expansion. This restricts the kinematic regions in which calculations are reliable to $z < 0.9$ [34]. Figure 2.8 shows results from HERA [39, 40] which are successfully described by a next-to-leading order calculation [41].

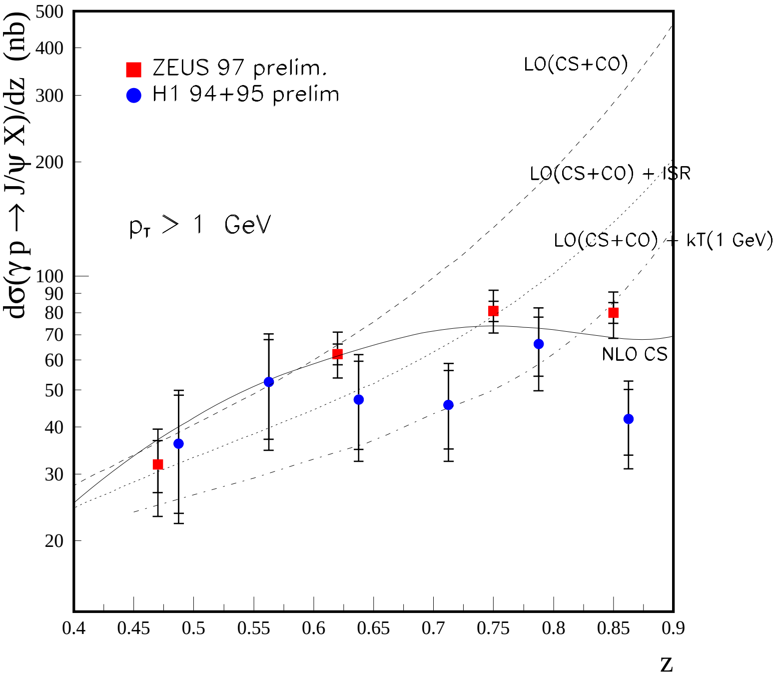

Figure 2.8: *Differential cross-section $d\sigma/dz$ for the inelastic photoproduction of J/ψ mesons at HERA [39, 40]. The line is the result of a next-to-leading order Colour Singlet model calculation [41]. The dashed lines are leading order Colour Octet model calculations with various additional affects [42].*

2.4.2 Tevatron Results on Charmonium Production

Despite the enormous predictive power of the Colour Singlet model, it has several known problems. The most obvious problem is the presence of infra-red divergences in the cross-sections for the production of P-wave charmonium states [38]. Similar divergences in the decay rates were known about as early as 1976. Barbieri et. al. [43] discovered that the decay rate for $\chi_{cJ} \rightarrow q\bar{q}g$ depends logarithmically on the minimum energy of the gluon. This problem was avoided phenomologically by imposing an ad hoc cut-off on the gluon energy, although this was without any real justification. Ex-

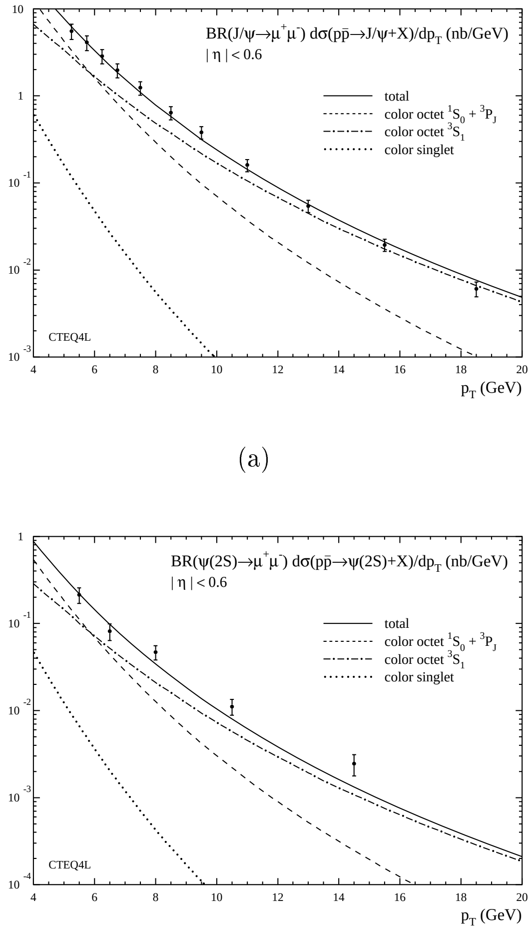

(a)

(b)

Figure 2.9: *Data and theoretical predictions for (a) J/ψ and (b) $\psi(2S)$ production in $p\bar{p}$ collisions at $\sqrt{s} = 1.8$ TeV. The data are from the CDF collaboration [46, 47]. The theoretical predictions and plots are taken from [53].*

perimentally, the UA1 collaboration had found discrepancies between measurements and the predictions of the Colour Singlet model in $p\bar{p}$ collisions at $\sqrt{s} = 630$ GeV [44]. The Colour Singlet model was finally shown to be incomplete when results on charmonium production where obtained at the Tevatron (which studies proton (p)-antiproton ($\bar{p}$) collisions at $\sqrt{s} = 1.8$ TeV) which were completely incompatible with the Colour Singlet model.

The CDF and D0 collaborations have studied J/ψ and $\psi(2S)$ production at the Tevatron in detail [45]-[52]. The production processes include indirect charmonium production via the production and decay of B-mesons, as well as "prompt" production. In "prompt" production, the contribution from b-quark decays has been excluded by requiring that the charmonium was produced at the primary event vertex. It is in "prompt" production where the failure of the Colour Singlet model is most prominent, as shown in figure 2.9. The figure shows the results from the CDF collaboration on prompt (a) J/ψ and (b) $\psi(2S)$ production [46, 47], and the Colour Singlet model prediction (dotted line) [53]. The Colour Singlet model predicts cross-sections which are a factor of up to ~ 50 too small for J/ψ's and $\psi(2S)$'s produced with large transverse momentum (p_t). Prior to these observations, J/ψ production at large p_t was expected to be dominated by B-hadron decay with some contribution from χ_{c1} and χ_{c2} decay [38]. Indeed, this assumption was used by CDF to extract a value for the b-quark production cross section from their data on J/ψ and χ_c production [45], which was subsequently shown to be too large by about a factor of 2 when more data became available [54]. The data from the Tevatron therefore required a new model in order to understand charmonium production.

2.4.3 Colour Octet Model

A model which successfully explains the results from the Tevatron, and solves many of the known problems of the Colour Singlet model, has been developed since 1992 and is known as the *Colour Octet* model. The first steps in the development of the model were made by Bodwin, Braaten and Lepage [55]. They realised that the infra-red divergences in the decay rate for $\chi_{cJ} \to q\bar{q}g$ arise when the final state gluon is soft (low p_t). They found that by allowing initial state gluon radiation, so that the initial $c\bar{c}$ pair are in a colour octet state, a second term is added to the decay amplitude which successfully describes the contribution to the decay rate causing the divergence. A similar solution was found for the production rate [56]. This approach was subsequently generalised by Bodwin, Braaten and Lepage [57] into a full theoretical framework for the calculation of the inclusive annihilation and production of heavy quarkonium. The theory is now known as the Colour Octet model, because it includes intermediate states where the $c\bar{c}$ is in a colour octet configuration (i.e. a state with net colour) in contrast to the Colour Singlet model which does not. For a thorough review of the Colour Octet model, reference [58] is recommended.

An important feature of the Colour Octet model developed by Bodwin, Braaten and Lepage is the use of the velocity scaling rules of non-relativistic QCD (NRQCD) [59]. NRQCD is an effective field theory formulation of QCD in which the heavy quark and anti-quark are treated non-relativistically. In the case of charmonium, potential model calculations indicate that the relative quark-antiquark velocity squared within the bound state is $v^2 \sim 1/3$ (in bottomonium $v^2 \sim 1/10$) [38]. Therefore, a perturbative expansion of the calculation in powers of v^2 could also be possible, in addition to the already possible expansion in terms of $\alpha_s(m_c)$.

Within the Colour Octet model, the inclusive cross section for producing a charmonium state H has the form

$$d\sigma(H+X) \;=\; \sum_n d\hat{\sigma}(c\bar{c}(n)+X)\langle\mathcal{O}_n^H\rangle, \tag{2.14}$$

where $d\hat{\sigma}(c\bar{c}(n)+X)$ is the inclusive cross section for the production of a $c\bar{c}$ pair in a colour and angular momentum state n, and $\langle\mathcal{O}_n^H\rangle$ is a matrix element related to the probability for a $c\bar{c}$ pair in a state n to form the charmonium state H. Thus, the cross section factorises into short and long distance parts in an analogous manner to the Colour Singlet model. The short distance part is $d\hat{\sigma}(c\bar{c}(n)+X)$, which is calculable perturbatively as an expansion in $\alpha_s(m_c)$, and the long distance part is $\langle\mathcal{O}_n^H\rangle$ which describes the non-peturbative evolution of the $c\bar{c}$ pair into the bound charmonium state. The sum is over all the possible colour and angular momentum states n of the $c\bar{c}$ pair. Hence the model explicitly includes $c\bar{c}$ pairs produced in a colour octet state, as well as those in a colour singlet state. Note that the only dependence on the final state is in $\langle\mathcal{O}_n^H\rangle$, whilst the only dependence on the production method resides in the short distance part.

Equation 2.14 contains a sum over an infinite number of intermediate states n. Hence its application would appear to be difficult as this would mean an infinite number of non-perturbative terms $\langle\mathcal{O}_n^H\rangle$. However, the higher angular momentum states involve higher powers of v^2 in the matrix element and so are correspondingly suppressed. The velocity scaling rules of NRQCD thus reduce the number of terms needed to a manageable level. The scaling of the matrix element $\langle\mathcal{O}_n^H({}^{2\mathrm{S}+1}\mathrm{L}_\mathrm{J})\rangle$ with v^2 can be determined from the number of electric dipole and magnetic dipole moments required to transform the meson H to a state $|c\bar{c}(\underline{n}, {}^{2S+1}L_J) + \text{gluons}\rangle$. There is an overall factor of v^{3+2L}, with an additional factor of v^2 for each electric dipole transition and v^4 for each magnetic dipole transition. Therefore, the relative importance of each state n in the factorisation formula given by equation 2.14 is determined by two factors: the order in v^2 of the matrix element $\langle \mathcal{O}_n^H \rangle$ and the order in $\alpha_s(m_c)$ of the parton cross section $d\hat{\sigma}(c\bar{c}(n) + X)$. Hence the charmonium cross-section can be calculated with arbitrary precision using a double expansion in terms of $\alpha_s(m_c)$ and v^2. Figure 2.9 illustrates the success of the Colour Octet model in explaining the Tevatron results [53].

2.4.4 Colour Octet Model Matrix Elements

The Colour Octet model is undoubtably successful in explaining the Tevatron results. However this requires fitting the model to the experimental data. This is because the matrix elements, $\langle \mathcal{O}_n^H \rangle$, cannot be calculated in QCD due to their non-perturbative nature. The non-perturbative matrix elements must therefore be determined either experimentally or from lattice QCD calculations [60][2]. If the factorisation used in equation 2.14 is correct, the matrix elements are universal i.e. they are independent of the production mechanism. Therefore, their measurement using several different mechanisms for charmonium production, will be a crucial test of the theory. For a recent, more detailed review of the extraction of the matrix elements, see [62]. The conclusions reached in [62] are identical to those presented here.

---

[2] No results are yet available for the production matrix elements from lattice QCD calculations due to theoretical problems [61].

This section will only consider the matrix elements for J/ψ production. The following notation will be used: $\langle\mathcal{O}_n^{J/\psi}(^{2S+1}\mathrm{L_J})\rangle$ is the matrix element for the formation of a J/ψ from a $c\bar{c}$ pair in a colour state n ($\underline{1}$ for colour singlet, $\underline{8}$ for colour octet) and an angular momentum state $^{2S+1}\mathrm{L_J}$, where standard spectroscopic notation is used. The matrix elements are extracted from fits to experimental data on J/ψ production, with the following constraint; the heavy quark spin symmetry present in NRQCD requires that the J dependent matrix elements satisfy the relation

$$\langle\mathcal{O}_{\underline{8}}^{J/\psi}(^3\mathrm{P_J})\rangle \;=\; (2\mathrm{J}+1)\langle\mathcal{O}_{\underline{8}}^{J/\psi}(^3\mathrm{P_0})\rangle. \tag{2.15}$$

The matrix element $\langle\mathcal{O}_{\underline{1}}^{J/\psi}(^3\mathrm{S_1})\rangle$ is equivalent to the long distance part of the cross-section in the Colour Singlet model and so can be determined independently as it is related to the electronic decay width of the J/ψ (see equation 2.13). A QCD improved [63] relation is

$$\Gamma_{ee} = \frac{8\pi\alpha^2 e_c^2}{9m_{J/\psi}^2}\Big(1 - \frac{16}{3}\frac{\alpha_s(m_{J/\psi})}{\pi}\Big)\langle\mathcal{O}_{\underline{1}}^{J/\psi}(^3\mathrm{S_1})\rangle, \tag{2.16}$$

where $e_c = 2/3$ is the fractional charge of the charm quark.

Several authors have extracted matrix elements by fitting the model to the Tevatron data. Despite the constraints, the best that can be achieved is relationships between some of the matrix elements. The matrix elements important for J/ψ production at the Tevatron are $\langle\mathcal{O}_{\underline{1}}^{J/\psi}(^3\mathrm{S_1})\rangle$, $\langle\mathcal{O}_{\underline{8}}^{J/\psi}(^3\mathrm{S_1})\rangle$, $\langle\mathcal{O}_{\underline{8}}^{J/\psi}(^1\mathrm{S_0})\rangle$, and $\langle\mathcal{O}_{\underline{8}}^{J/\psi}(^3\mathrm{P_0})\rangle$ [53] which are defined in [57]. It turns out that, due to the parton production cross sections

$d\hat{\sigma}(c\bar{c}(n) + X)$ having similar p_t dependences, the p_t distribution of the cross section at low p_t is sensitive only to a combination of $\langle \mathcal{O}_{\underline{8}}^{J/\psi}({}^1\mathrm{S}_0)\rangle$ and $\langle \mathcal{O}_{\underline{8}}^{J/\psi}({}^3\mathrm{P}_0)\rangle$, given by

$$M_k^{J/\psi} \;=\; \langle \mathcal{O}_{\underline{8}}^{J/\psi}({}^1\mathrm{S}_0)\rangle + \frac{k}{m_c^2}\langle \mathcal{O}_{\underline{8}}^{J/\psi}({}^3\mathrm{P}_0)\rangle, \tag{2.17}$$

whilst $\langle \mathcal{O}_{\underline{8}}^{J/\psi}({}^3\mathrm{S}_1)\rangle$ is dominant at large p_t [53]. By choosing a suitable value for k (3 is chosen in [64], 3.5 in [53], for example), the Tevatron data can be fitted with just two free phenomenological parameters, $\langle \mathcal{O}_{\underline{8}}^{J/\psi}({}^3\mathrm{S}_1)\rangle$ and $M_k^{J/\psi}$.

There are several theoretical uncertainties connected with the extraction: the choice of parton density function (PDF) for the proton, the intrinsic transverse momentum (k_t) of the partons, the mass of the charm quark and the choice of factorisation scale. Mizukoshi [65] is one of several authors who have extracted the matrix elements using several different PDF's, namely MRS(R2) [66], CTEQ 4L [20] and GRV 94 LO [67]. His values for $\langle \mathcal{O}_{\underline{8}}^{J/\psi}({}^3\mathrm{S}_1)\rangle$ and $M_k^{J/\psi}$ (with $k = 3$) are shown in table 2.1. As can be seen, the choice of PDF's leads to an uncertainty of approximately a factor of two. This is supported by other studies, see [53] for example.

The effect of the intrinsic transverse momentum (k_t) of the partons on the extracted matrix elements has been studied by several authors. In an initial fit to the data, where intrinsic k_t was ignored, Cho and Leibovich [64] extracted the values

$$\langle \mathcal{O}_{\underline{8}}^{J/\psi}({}^3\mathrm{S}_1)\rangle \;=\; (6.6 \pm 2.1) \times 10^{-3}\ \mathrm{GeV}^3 \quad \text{and} \tag{2.18}$$

$$M_k^{J/\psi} \;=\; (66 \pm 15) \times 10^{-3}\ \ \mathrm{GeV}^3, \tag{2.19}$$

Author	PDF	$\langle \mathcal{O}_{\underline{8}}^{J/\psi}({}^3\mathrm{S}_1)\rangle$	$M_k^{J/\psi}$	k
Mizukoshi [65]	CTEQ 4L	0.54 ± 0.12	2.28 ± 0.55	3
	GRV(1994)LO	0.57 ± 0.12	2.07 ± 0.53	3
	MRS(R2)	0.70 ± 0.17	4.85 ± 0.95	3
Beneke and Kramer [53]	CTEQ 4L [20]	1.06 ± 0.14	4.38 ± 1.15	3.5
	GRV(1994)LO [67]	1.12 ± 0.14	3.90 ± 1.14	3.5
	MRS(R2) [66]	1.40 ± 0.22	10.9 ± 2.07	3.5
Cho and Leibovich [64]	MRSD0 [70]	0.66 ± 0.21	6.6 ± 1.5	3
Braaten, Kniehl and Lee [71]	MRST98(LO) [74]	0.44 ± 0.07	8.7 ± 0.9	3.4
	CTEQ 5L [75]	0.49 ± 0.07	6.6 ± 0.7	3.4
Kniehl and Kramer [72]	CTEQ 4M [20]	0.273 ± 0.045	0.572 ± 0.184	3.54
Cano-Coloma and Sanchis-Lozano [68]	CTEQ2L [76]	0.33 ± 0.05	1.44 ± 0.21	3
	MRSD0	0.21 ± 0.05	1.32 ± 0.21	3
	GRV(1994)HO [67]	0.34 ± 0.04	0.60 ± 0.12	3
Sanchis-Lozano [73]	CTEQ2L	0.96 ± 0.15	1.32 ± 0.21	3
	MRSD0	0.68 ± 0.16	1.32 ± 0.21	3
	GRV(1994)HO	0.92 ± 0.11	0.45 ± 0.09	3

Table 2.1: *Values of* $\langle \mathcal{O}_{\underline{8}}^{J/\psi}({}^3\mathrm{S}_1)\rangle$ *and* $M_k^{J/\psi}$ *in units of* 10^{-2} GeV^3 *extracted from the Tevatron data by various authors.*

for $k = 3$. However, it was subsequently shown that the intrinsic k_t of the partons can have a large effect on the extracted matrix elements [68]. Using the Monte Carlo program PYTHIA [69] to simulate intrinsic k_t in the partons, Cho and Leibovich obtained the values

$$\langle \mathcal{O}_{\underline{8}}^{J/\psi}({}^3\mathrm{S}_1)\rangle = (2.1 \pm 0.5) \times 10^{-3}\ \mathrm{GeV}^3 \text{ and} \tag{2.20}$$

$$M_k^{J/\psi} = (13.2 \pm 2.1) \times 10^{-3}\ \mathrm{GeV}^3, \tag{2.21}$$

where $k = 3$ and the MRSD0 [70] PDF was used in each case. Hence, neglecting the intrinsic k_t of the partons can lead to a significant overestimation of the colour octet matrix elements.

Many authors have extracted the matrix elements from the Tevatron data using various PDF's and theoretical assumptions, such as the choice of charm quark mass. A summary of several of these results is given in table 2.1. As can be seen, there is no consistent picture emerging. The extracted values are sensitive to the PDF and theoretical assumptions used. Hence they can at present only be considered accurate to order of magnitude.

There are results from other experiments which can be used to constrain the matrix elements further. For example, from fixed target hadroproduction, the relation

$$\langle \mathcal{O}_{\underline{8}}^{J/\psi}(^1\mathrm{S}_0)\rangle + \frac{7}{m_c^2}\langle \mathcal{O}_{\underline{8}}^{J/\psi}(^3\mathrm{P}_0)\rangle \;=\; 3\times 10^{-2}\ \mathrm{GeV}^3. \tag{2.22}$$

has been obtained by Beneke and Rothstein [77]. From the B-meson decay $B \to J/\psi X$, Beneke et. al. [78] obtained the constraint

$$\langle \mathcal{O}_{\underline{8}}^{J/\psi}(^1\mathrm{S}_0)\rangle + \frac{3.6}{m_c^2}\langle \mathcal{O}_{\underline{8}}^{J/\psi}(^3\mathrm{P}_0)\rangle \;<\; 2.8\times 10^{-2}\ \mathrm{GeV}^3. \tag{2.23}$$

A very clean extraction of the matrix elements could be obtained from the LEP experiments using the decay $Z \to J/\psi X$, which would remove the uncertainty arising from the choice of PDF, for example. However, this has only been performed so far for a combination of the matrix elements for several different charmonium states, weighted by branching ratios [79]. This is due to the experimental limitations of low statistics and an inability to separate feed-down from χ_c's and $\psi(2\mathrm{S})$'s.

HERA data can also be used to extract the matrix elements. Unfortunately, results for J/ψ photoproduction only exist in a region most sensitive to the colour singlet

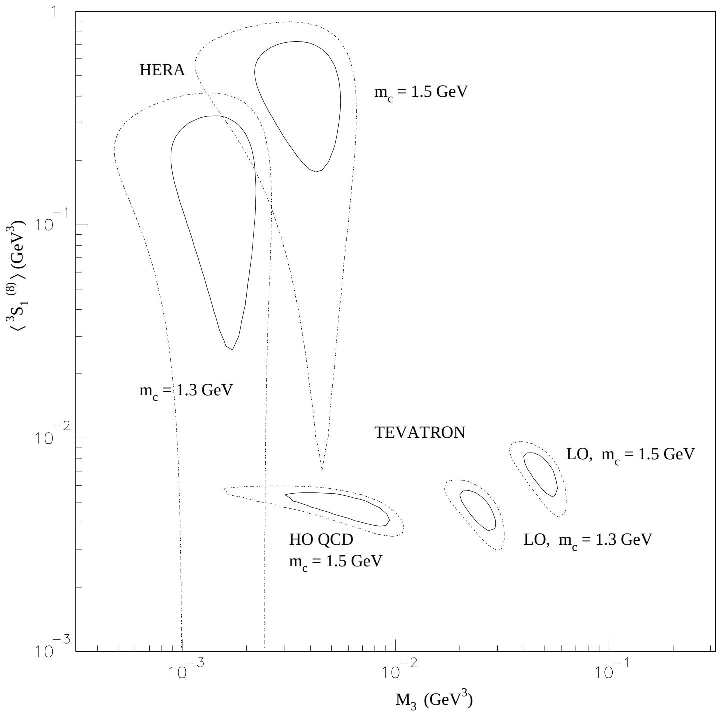

Figure 2.10: *Parameter space for the matrix elements* $\langle \mathcal{O}_{\underline{8}}^{J/\psi}({}^3\mathrm{S}_1)\rangle$ *and* $M_k^{J/\psi}$, *for* $k = 3$, *extracted using HERA or Tevatron data. The bounds on the extracted values are at* 68% *confidence limit (solid lines) and at* 95% *confidence limit (dashed lines). The plot is from [65].*

matrix element, $\langle \mathcal{O}_{\underline{1}}^{J/\psi}({}^3\mathrm{S}_1)\rangle$, and the matrix elements most sensitive to higher order corrections at the Tevatron [80]. As can be seen in figure 2.8, the Colour Singlet model can describe the HERA data. The Colour Octet model calculation [42] predicts a rise as $z \to 1$ which is not observed in the data. However, this is the region in which the model begins to break down as it corresponds to the transition from inelastic to diffractive production which is poorly understood. Hence, it cannot yet be concluded that the HERA data implies the non-universality of the matrix elements. Additionally, attempts to extract the matrix elements from the HERA data alone produces large errors. This is illustrated by figure 2.10, which shows the matrix elements extracted by Mizukoshi [65]

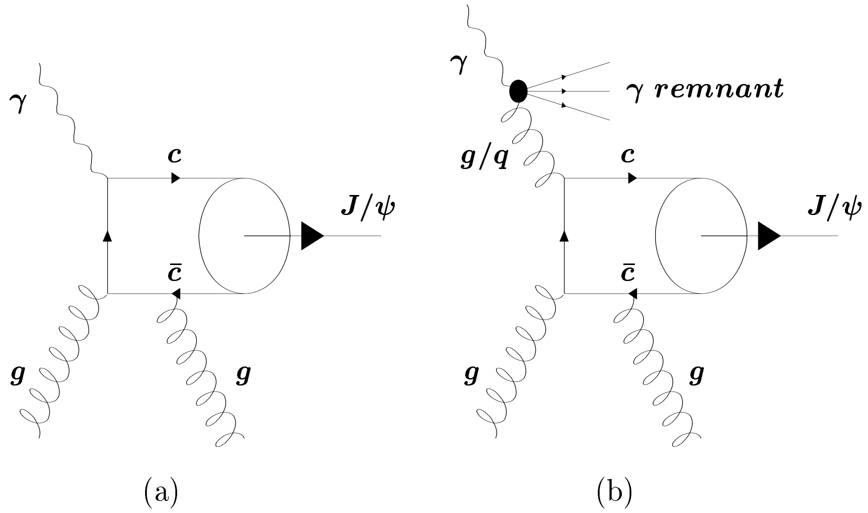

Figure 2.11: *Diagrams for (a) direct and (b) resolved photoproduction of J/ψ's at HERA.*

from both HERA and Tevatron data independently and their associated uncertainty. The two experiments appear to require different matrix elements. However the figure also illustrates both the large uncertainty arising from the use of the HERA data and the theoretical uncertainties arising from the choice of value for the charm quark mass and from higher order corrections. Extending the HERA results into new kinematic regions, such as the low-z region, would reduce the uncertainty on extractions from the HERA data.

2.4.5 Inelastic J/ψ Production

The inelastic photoproduction of J/ψ's at HERA proceeds through one of two processes mentioned previously: direct or resolved boson-gluon fusion. The two processes are illustrated by figure 2.11. In direct boson-gluon fusion, the incoming electron emits a photon which interacts with a parton (usually a gluon) from within the proton to produce the J/ψ. In resolved events, the photon fluctuates into a hadronic state and a parton from within the 'photon' interacts with a parton from within the proton. Direct photoproduction dominates at high z ($z \gtrsim 0.4$) whilst resolved photoproduction dominates at low z ($z \lesssim 0.3$), as shown by figure 2.12(a).

The HERA J/ψ production cross-section is dominated by the same matrix elements as for the Tevatron, i.e. $\langle\mathcal{O}_{\underline{1}}^{J/\psi}(^3\mathrm{S}_1)\rangle$, $\langle\mathcal{O}_{\underline{8}}^{J/\psi}(^3\mathrm{S}_1)\rangle$, $\langle\mathcal{O}_{\underline{8}}^{J/\psi}(^1\mathrm{S}_0)\rangle$, and $\langle\mathcal{O}_{\underline{8}}^{J/\psi}(^3\mathrm{P}_0)\rangle$. Beneke, Kramer and Vanttinen [78] have studied the inelastic photoproduction of J/ψ's within the Colour Octet model. At the parton level, they considered the direct photon mechanisms

$$\begin{aligned} \gamma + g &\rightarrow c\bar{c} + g \\ \gamma + q/\bar{q} &\rightarrow c\bar{c} + q/\bar{q} \end{aligned}$$

where the $c\bar{c}$ subsequently forms a J/ψ and the processes are at order $\mathcal{O}(\alpha\alpha_s^2)$. They also included the resolved photon mechanisms

$$\begin{aligned} g + g &\rightarrow c\bar{c} + g \\ g + q/\bar{q} &\rightarrow c\bar{c} + q/\bar{q} \\ q + \bar{q} &\rightarrow c\bar{c} + g \end{aligned}$$

where one initial parton originates from the photon and one from the proton, and the $c\bar{c}$ subsequently forms a J/ψ. The processes are at $\mathcal{O}(\alpha_s^3)$.

For the matrix elements, two scenarios were compared in order to estimate the theoretical uncertainty. In both cases, $\langle\mathcal{O}_{\underline{1}}^{J/\psi}({}^3\mathrm{S}_1)\rangle$ was set to 116×10^{-2} GeV^3 and $\langle\mathcal{O}_{\underline{8}}^{J/\psi}({}^3\mathrm{S}_1)\rangle$ to 1.06×10^{-2} GeV^3, the latter coming from a fit to the Tevatron data at large p_t [53]. The two scenarios differed in the method for extracting the components of $M_k^{J/\psi}$. In one scenario, $\langle\mathcal{O}_{\underline{8}}^{J/\psi}({}^3\mathrm{P}_0)\rangle$ was set to 0 with $\langle\mathcal{O}_{\underline{8}}^{J/\psi}({}^1\mathrm{S}_0)\rangle$ set to 3.0×10^{-2} GeV^3. In the second scenario, $\langle\mathcal{O}_{\underline{8}}^{J/\psi}({}^1\mathrm{S}_0)\rangle$ was set to 0 with $\langle\mathcal{O}_{\underline{8}}^{J/\psi}({}^1\mathrm{S}_0)\rangle/m_c^2$ set to 1.0×10^{-2} GeV^3. These values were obtained using constraints extracted from the Tevatron data [53], fixed target data [77] and B-meson decays, and the authors used the GRV LO [67, 81] PDF's for both the proton and the photon. The results of their study are shown in figure 2.12.

2.5 Summary and Status

Charmonium production remains an active area of both theoretical and experimental interest. Despite the success of the Colour Singlet model in explaining the HERA data, it has been found to be completely inconsistent with results from the Tevatron. A new theoretical model has been developed, based on NRQCD, which is more refined and general, and is known as the Colour Octet model. This model is able to explain the large J/ψ and $\psi(2\mathrm{S})$ production cross-sections observed at the Tevatron and solves known theoretical problems of the Colour Singlet model. Despite this, the Colour Octet model has problems when applied to the HERA data. Using matrix elements extracted from the Tevatron data, it predicts a rapid rise in the cross-section as $z \to 1$ which is not observed in the data. Furthermore, the matrix elements extracted from the HERA

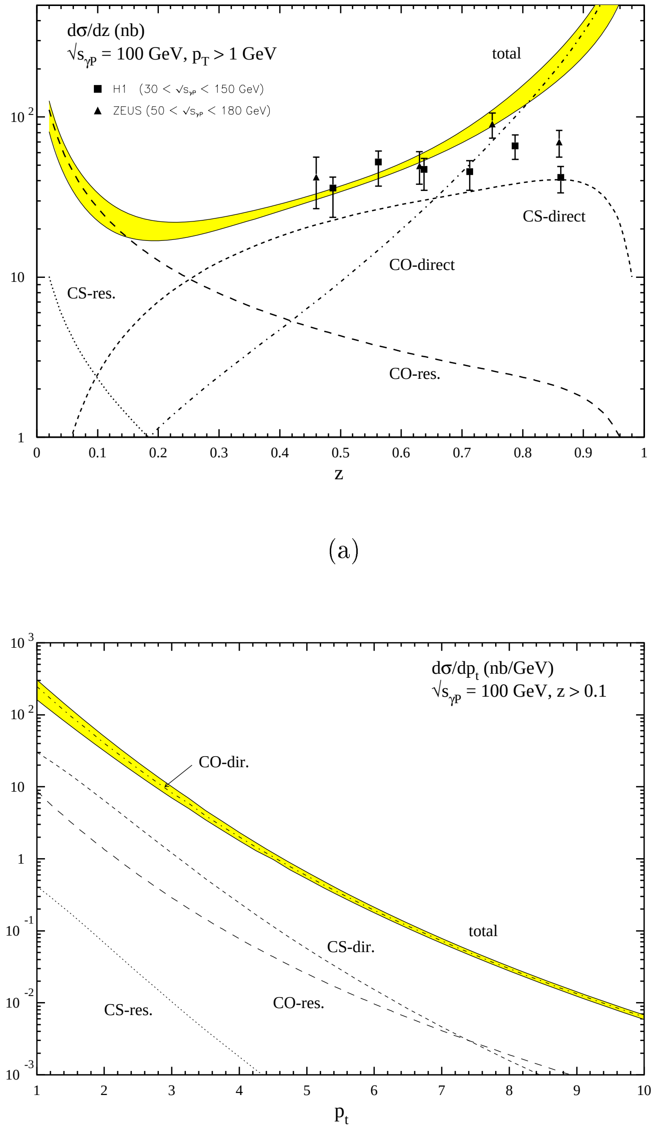

(a)

(b)

Figure 2.12: *Colour Singlet (CS) and Colour Octet (CO) contributions to the cross-section at HERA, arising from direct and resolved photon interactions, as a function of (a) z and (b)* $p_{t.J/\psi}$. *The shaded area represents the uncertainty arising from a variation of the colour octet matrix elements. The calculations are for a photon-proton centre-of-mass energy of 100 GeV and are compared in (a) to HERA data [30, 40]. The calculations and plots are from [78].*

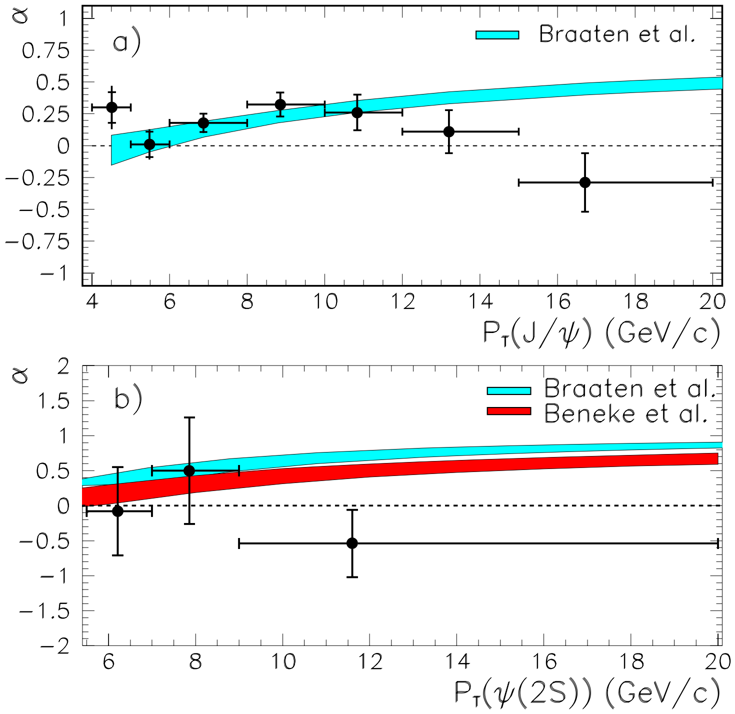

Figure 2.13: *The polarisation of prompt (a)* J/ψ *and (b)* $\psi(2S)$ *mesons, produced in* $p\bar{p}$ *collisions at* $\sqrt{s} = 1.8$ *TeV, as measured by the CDF collaboration [50]. The shaded bands represent Colour Octet model predictions for (a)* J/ψ *[71] and (b)* $\psi(2S)$ *[53, 71] polarisation.*

data disagree with those extracted from the Tevatron data. However, due to the large uncertainty in the extraction from the HERA data and theoretical uncertainties (e.g. higher order corrections, the charm quark mass), no conclusion about the universality of the matrix elements can yet be drawn.

Recently there have been both experimental and theoretical developments which complicate the picture further. The CDF collaboration has measured the polarisation of charmonium produced in $p\bar{p}$ collisions at $\sqrt{s} = 1.8$ TeV [50]. The results, shown in figure 2.13, disagree with the predictions of the Colour Octet model [53, 71] at large

p_t. A recent theoretical development has been a study of the hadroproduction of χ_{cJ}'s within the k_t factorisation approach by Hagler et. al. [82]. This takes into account the intrinsic transverse momentum of the colliding partons in a new way and is found to give good agreement with data. The authors have also recently extended this approach to study the direct hadroproduction of J/ψ's at the Tevatron [83]. Their results indicated a reduced contribution due to the $\langle \mathcal{O}_{\underline{8}}^{J/\psi}(^3\mathrm{S}_1)\rangle$ matrix element and a reduced polarisation. The extension of this approach to cover all charmonium production could be interesting.

2.6 Event Simulation

In order to correct the data for the effects of the experimental cuts, detector resolution etc., Monte Carlo simulated events are used. The Monte Carlo generators simulate a particular physics process and deliver the four-momenta of all particles produced with lifetimes longer than $\sim$ 8 ns. The particles are then passed through a GEANT [84] based application which tracks the particles through a simulation of the detector and simulates effects such as secondary particle production and shower development. All aspects of the H1 detector (see chapter 3) are simulated in full, including the trigger system. The output produced is very similar to that for a real data event, and this is then passed through the full reconstruction and analysis software. Two Monte Carlo generators are used in this analysis: EPJPSI and DIFFVM.

The Monte Carlo generator EPJPSI [85] is used to simulate the events under study here. EPJPSI is able to simulate J/ψ production in a variety of processes in γp, ep, μp, $p\bar{p}$, and pp collisions. It is used here for the simulation of direct and resolved photoproduction events separately. The resolved events are generated according to a leading order Colour Singlet model calculation, whilst the direct events are generated using a calculation involving both Colour Singlet and Colour Octet contributions at leading order. Relativistic corrections are included for the Colour Singlet terms [86]. The hadronisation is performed using the LUND string fragmentation in JETSET [69]. The events were generated using the MRS(Ap) PDF's [87] as implemented in PDFLIB [88].

The DIFFVM Monte Carlo generator [89] is used to simulate J/ψ's and ψ(2S)'s produced in diffractive interactions. This is a contribution to the background to the inelastic J/ψ signal. The DIFFVM programme simulates diffractive vector meson production within the framework of Regge Theory [90] and the Vector Dominance Model (VDM) [91]. Both elastic and proton dissociative diffractive vector meson production can be simulated.

Chapter 3

The H1 Experiment

3.1 Introduction

The H1 detector is one of four multipurpose detectors which use the HERA accelerator. It is designed to investigate all aspects of e-p scattering. This chapter will describe the HERA accelerator and the H1 detector. The first section will give an overview of the HERA accelerator, then an overview of the H1 detector will be given, with the individual parts subsequently described in more detail. For a more detailed description of the H1 detector, see [92].

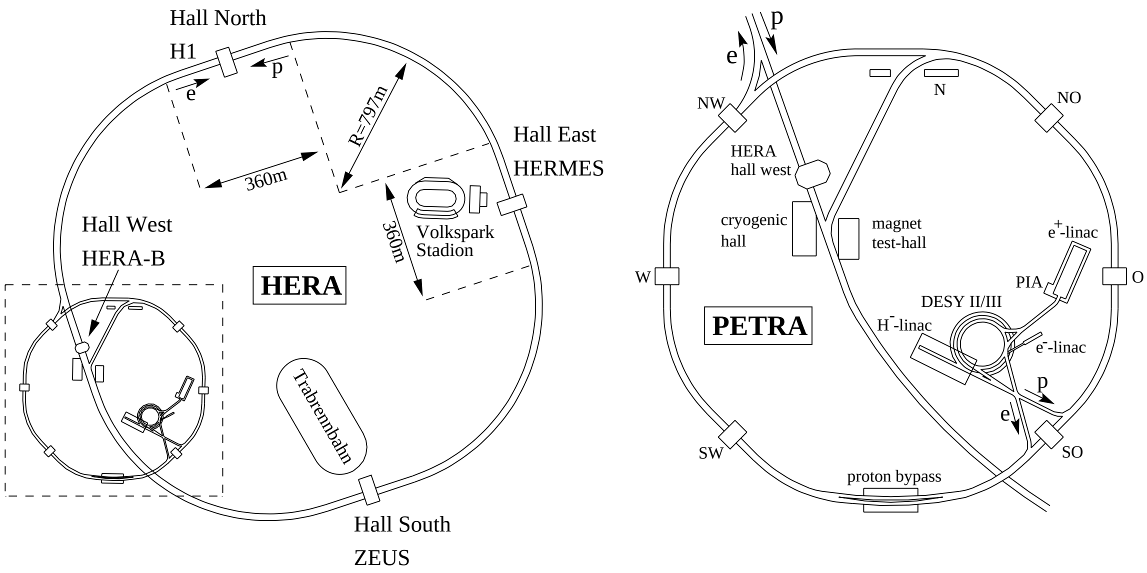

Figure 3.1: *Layout of HERA and its pre-accelerators.*

3.2 The HERA Accelerator

The **H**adron **E**lectron **R**ing **A**nlage (HERA) collider at DESY is the world's first electron[1]-proton (e-p) collider. There are two independent storage rings and several pre-accelerators, the layout of which is shown in figure 3.1. One of the storage rings accelerates and stores 820 GeV protons[2], whilst the other accelerates and stores 27.5 GeV electrons.

The beams are collided at two interaction points, at each of which is situated a multipurpose detector (H1 and ZEUS), each designed to study electron-proton collisions. The collisions are at a total centre-of-mass energy of $\sqrt{s} \sim 300$ GeV. This is an order of

---

[1] HERA can, and has, run with either electrons or positrons. From here onwards the leptons in the beam will be referred to as electrons.

[2] In 1998 the proton beam energy was increased to 920 GeV. However, this analysis only uses data taken with a proton beam energy of 820 GeV, so this energy will be used throughout.

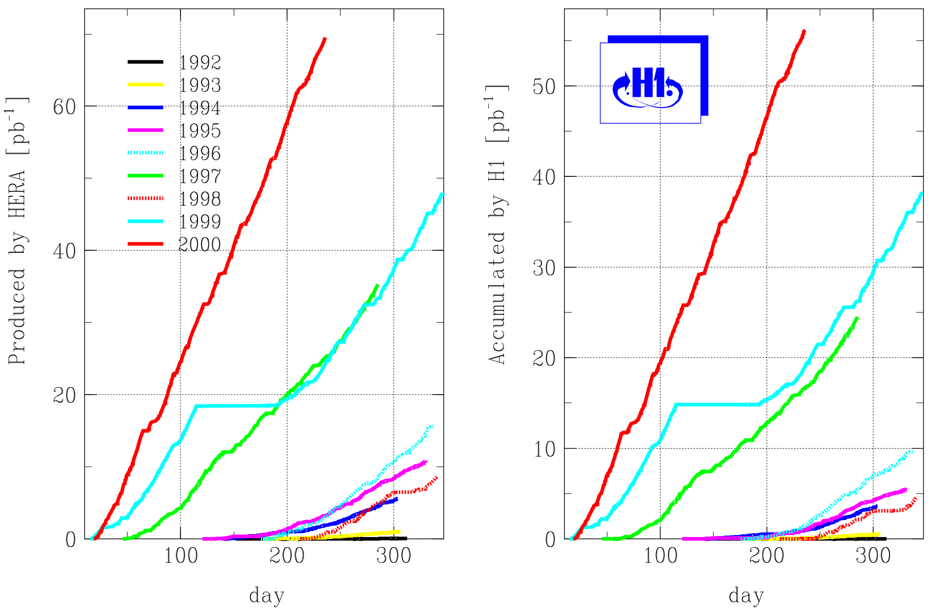

Figure 3.2: *Luminosity delivered by HERA and collected by H1 1992-2000.*

magnitude greater than the energies achieved at previous fixed target e-p experiments. Two further detectors each make use of one of the beams. The HERMES detector makes use of a longitudinally polarised electron beam which collides with a polarised gaseous target. The HERA-B detector studies the interaction of protons with a fixed wire target.

The electron and proton beams are stored in up to 220 bunches, which are arranged such that a bunch from each beam crosses the interaction points every 96 ns. Each filled bunch contains $\sim 10^{11}$ particles. Several bunches are left empty so that the corresponding bunch from the other beam does not undergo collisions. These 'pilot bunches' are used to study beam induced backgrounds, such as beam-gas interactions. As a result, there are typically $\sim$ 175 pairs of interacting bunches per fill of the accelerator.

Figure 3.2 shows the luminosity delivered by HERA and recorded by H1 for each year since HERA started running in 1992. The figure illustrates the improving performance, over time, of the HERA machine as an increased amount of luminosity is delivered each year.

3.3 Overview of the H1 Detector

3.3.1 Requirements

The unique HERA environment imposes certain demands which the detector must fulfil in order to extract the maximum physics information. All previous collider facilities have collided either particle-antiparticle pairs, or two identical particles, of equal energy in the lab frame[3]. This has led to the use of detectors which are symmetric about the interaction point. HERA collides different particles which are at different energies, so that the centre of mass frame is boosted with respect to the lab frame. This requires a detector design which is correspondingly asymmetric.

The kinematic quantities x, y, and Q^2 of the event (see section 2.2.1) can be reconstructed from the scattered electron alone, so high efficiency for the detection of electrons, and high precision and resolution for the measurement of its energy and scattering angle, is essential. This should extend over as full an angular range as possible so that measurements can be made over the full kinematic region accessible at HERA.

---

[3] Historically, fixed target experiments have also had asymmetric designs and, more recently, experiments such as BaBar have used beams of different energies.

Tracking detectors with a high resolution and hermicity are essential. The design should enable track multiplicities in jets with high particle densities to be measured, allow particle identification through energy loss, and allow charged particle momentum measurements to be made. The later measurement requires that the trackers are located within a magnetic field, so that the momentum can be deduced from the track curvature.

The calorimeters must have a high granularity so that the angular energy distribution of the final state can be reconstructed. It must also have a good hermicity so that imbalances in transverse momentum can be detected, as this is a signature for charged current events (see section 2.2.3) and for possible new physics.

Muon detectors covering the full angular range are also essential. Muons are often produced via the decay of heavy flavour particles. They could also be a signature for new or exotic particles.

The asymmetric beam energies at HERA mean that the centre of mass of the *e*-*p* events has a large boost in the forward (or proton) direction. As a result, extra detectors, with enhanced granularity and depth, are needed in this region.

An efficient fast trigger system is needed to distinguish real *e*-*p* events from a very high background, and to select the physics events of most interest. The sources of background include interactions between the beam and residual gas within the accelerator (beam-gas interactions), interactions between the beam and the accelerator walls (beam-wall interactions), and cosmic rays. The particles in the beams are in bunches which cross every 96 ns. The response times of the individual detectors, however, can be much longer. Therefore, the trigger system must be able to identify interesting events every 96 ns, and store the event information until enough is available for a trigger decision.

3.3.2 The H1 Detector

The layout of the H1 detector is shown in figure 3.3. The nominal interaction point is at the centre of the H1 detector. Located around the interaction point are the tracking detectors, the central $\boxed{2}$ and forward $\boxed{3}$ trackers. Within the central tracker, but not shown, are the central and backward silicon trackers. Surrounding the trackers are the calorimeters. The Liquid Argon (LAr) calorimeter is segmented into electromagnetic $\boxed{4}$ and hadronic $\boxed{5}$ sections. The Plug calorimeter $\boxed{13}$ is located close to the beam pipe, in the forward direction, in order to detect hadronic energy at low scattering angles. In the backward direction is the SPACAL calorimeter $\boxed{12}$. The calorimeters and trackers are surrounded by a superconducting solenoid magnet $\boxed{6}$, which produces a field of 1.2 Tesla. The iron return yoke of the magnet $\boxed{10}$ is instrumented and used to detect muons. This is complemented by the forward muon detector $\boxed{11}$, which detects muons in the forward direction. Several detectors are located close to the beam pipe but away from the interaction region and are not shown. Electron and photon taggers are located close to the beam pipe in the backward (or electron) direction. These are used for luminosity measurements and detecting electrons scattered through very small angles. In the forward direction are the proton remnant tagger, forward neutron

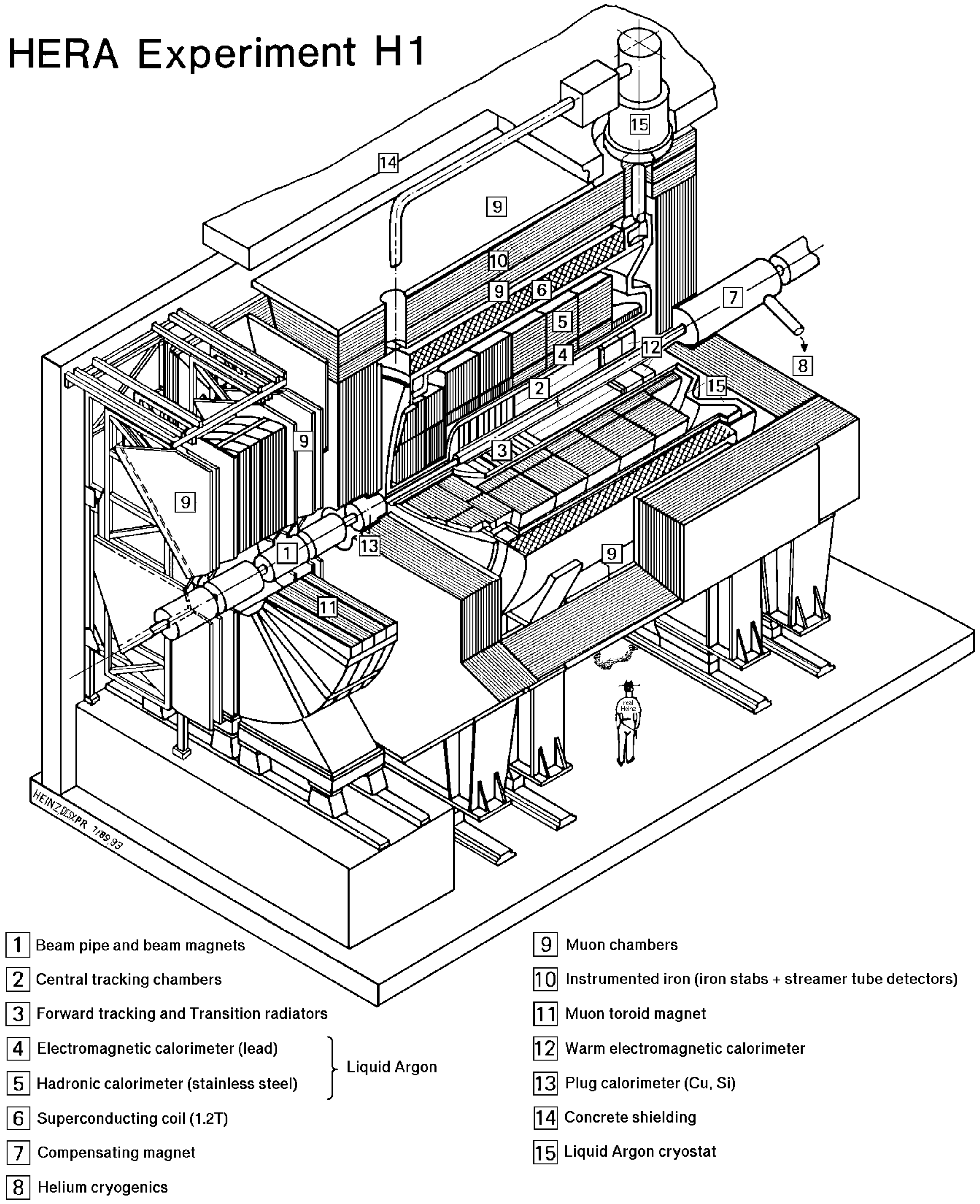

Figure 3.3: *The H1 Detector.*

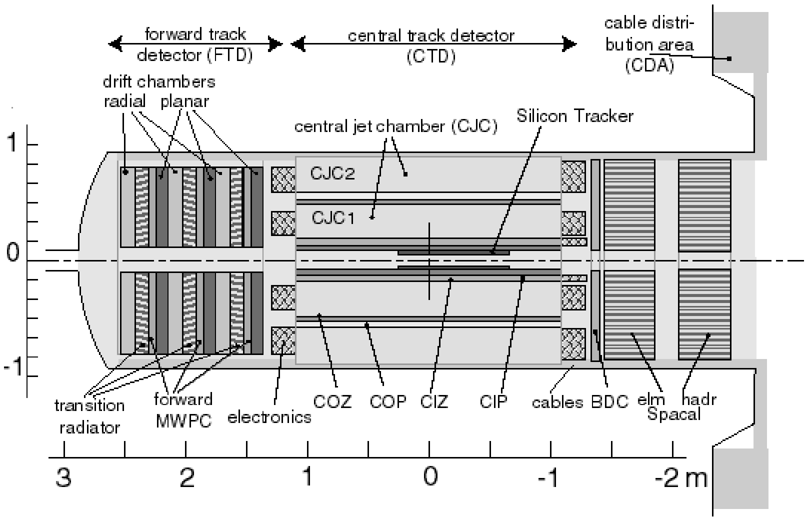

Figure 3.4: *Side view of the H1 tracking system.*

calorimeter and the forward proton spectrometer. These are used for identifying intact protons and neutrons scattered through low angles, and dissociated protons.

H1 uses a right handed coordinate system with the positive z-direction being defined as the forward or proton beam direction. The origin is at the nominal interaction point, with the y-axis vertically upwards. In spherical coordinates, the polar angle θ is defined as the angle relative to the positive z-axis. The azimuthal angle, ϕ, is the angle around the z-axis, with $\phi = 0^\circ$ along the y-axis.

3.4 Tracking

The layout of the H1 tracking system is shown in figure 3.4. The tracking system can be divided into four main components; the Central Tracking Detector (CTD), the

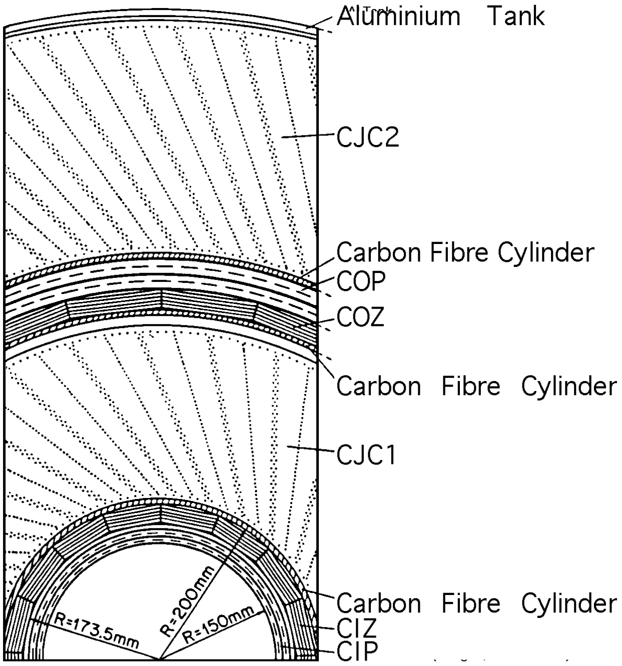

Figure 3.5: *Cross-section of the Central Tracker in the $r - \phi$ plane.*

Forward Tracking Detector (FTD), the Backward Drift Chambers (BDC), and the Silicon Trackers. These are described below.

3.4.1 The Central Tracking Detector (CTD)

The CTD consists of two large concentric drift chambers called the Central Jet Chambers (CJC1 and CJC2), two multiwire proportional chambers (CIP and COP), and two thin drift chambers (CIZ and COZ). The CTD covers the angular range $15° \lesssim \theta \lesssim 165°$. Figure 3.5 shows a cross-sectional view of the CTD in the $r - \phi$ plane.

The Central Jet Chambers (CJC1 and CJC2) are drift chambers with sense wires strung parallel to the beam direction and drift cells which are inclined at 30° to the radial direction, as shown in figure 3.5. CJC1 consists of 30 drift cells containing 24 sense wires in each. CJC2 has 60 drift cells, each containing 32 sense wires. This provides a good measurement of the $r - \phi$ coordinate, with a resolution of 170 μm. The z coordinate can be measured using charge division as the sense wires are read out at both ends. However, this method gives only a moderate resolution of 22 mm. The transverse momentum resolution is $\sigma_{p_t}/p_t^2 = 0.01/\text{GeV}$.

Sandwiching CJC1 are two thin 'z-chambers' (CIZ and COZ). These are drift chambers consisting of 4 layers of sense wire strung perpendicular to the beam direction. These two detectors provide a measurement of the z coordinate with a resolution of 260 μm.

Two multiwire proportional chambers, the CIP and COP, are mounted inside the CIZ and outside the COZ respectively. They both consist of pad cathodes which are segmented in z and ϕ. The CIP is segmented 60-fold in z and 16-fold in ϕ, whilst the COP is segmented 18-fold in z and 16-fold in ϕ. Their main purpose is to provide fast trigger information concerning the origin of any tracks within the event. Hits in the CIP and COP are linked and extrapolated back to possible z vertex positions. The requirement that the z coordinate of the event vertex lies in the nominal interaction region is a powerful way to reject background. The timing of these detectors is much better than the HERA bunch crossing time of 96 ns.

3.4.2 The Forward Tracking Detector (FTD)

Due to the higher track multiplicity in the forward direction, and the fact that high momentum charged particles produced at low angles ($\theta \lesssim 30^\circ$) are only weakly bent by the magnetic field, extra tracking detectors are needed in this region. The FTD is used to provide tracking information in the angular range $5^\circ \lesssim \theta \lesssim 30^\circ$. It consists of three supermodules, each containing three planar drift chambers, a multiwire proportional chamber, a passive transition radiator and a radial drift chamber. Each supermodule is aligned parallel to the $x - y$ plane. The planar chambers consist of 32 cells with 4 sense wires strung in parallel. The wires in each layer are rotated by 60° with respect to the previous layer. They are used to give an x, y space point measurement with a resolution of order 170 μm. The radial chambers are segmented into 48 sectors in ϕ, with each sector containing 12 sense wires. They are used for measurements in the $r - \phi$ plane and have a resolution of order 200 μm. The multiwire proportional chambers are used, in conjunction with the CIP and COP (see section 3.4.1), for triggering.

3.4.3 Backward Drift Chambers (BDC)

The Backward Drift Chambers (BDC) [93] are used for the accurate measurement of the scattering angle of electrons. The BDC consists of four double layers of drift chambers of octagonal shape. The four planes are rotated by 11.5° in ϕ with respect to the adjacent planes. Hits in the BDC are extrapolated to the electromagnetic part of the SPACAL (see section 3.5.2) in order to see if they can be associated with an energy cluster. The resolution of this impact point is 1 mm, yielding a θ resolution for the scattering angle of the electrons of 1 mrad.

3.4.4 Silicon Trackers

Two silicon trackers have recently been added to the H1 detector; these are the Central Silicon Tracker (CST) [94] and the Backward Silicon Tracker (BST) [95]. They were installed in 1996 in order to enhance the resolution of track parameters in the central and backward directions, to make separation of the primary and secondary vertices possible, and to improve the measurement of the track of electrons in low Q^2 DIS events. Secondary vertices arise when a relatively long lived particle produced at the primary vertex subsequently decays into two or more particles.

The CST consists of two layers of silicon strip detectors mounted cylindrically around the beampipe. It is centred at the nominal interaction point and covers the polar angular range $30^\circ < \theta < 150^\circ$. The BST consists of 8 planes of silicon detector discs, each disc containing 16 wedge shaped wafers. The BST covers the polar angular range $162^\circ < \theta < 176^\circ$.

3.5 Calorimetry

The calorimeters are used to measure the energy of both charged and neutral particles. The layout of the H1 calorimetry system is shown in figure 3.6. There are three main

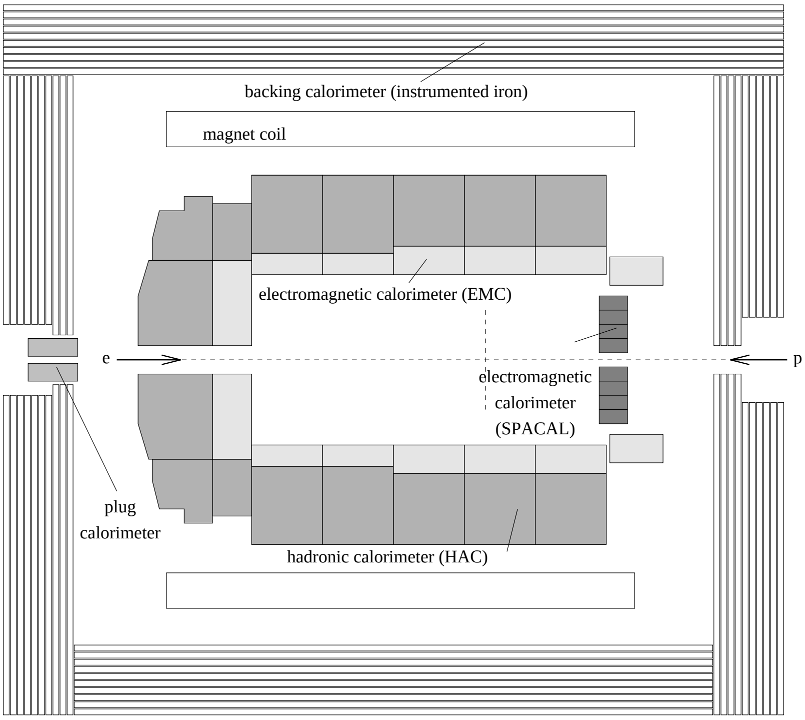

Figure 3.6: *Layout of the H1 calorimetry system.*

components: the Liquid Argon (LAr), SPACAL and Plug. The iron return yoke of the magnet is also instrumented to provide a measurement of any particles which manage to 'punch through' the main calorimeters.

3.5.1 Liquid Argon Calorimeter (LAr)

The LAr calorimeter [96] comprises two parts: an electromagnetic (EMC) and a hadronic (HAC) part. It covers the polar angular range $4^\circ \lesssim \theta \lesssim 153^\circ$. Both sections use liquid argon as the sampling material. The calorimeter is divided into 8 wheels in z (see figure 3.7), each wheel is then subdivided azimuthally into 8 ϕ octants. All but two wheels contain both electromagnetic and hadronic sections.

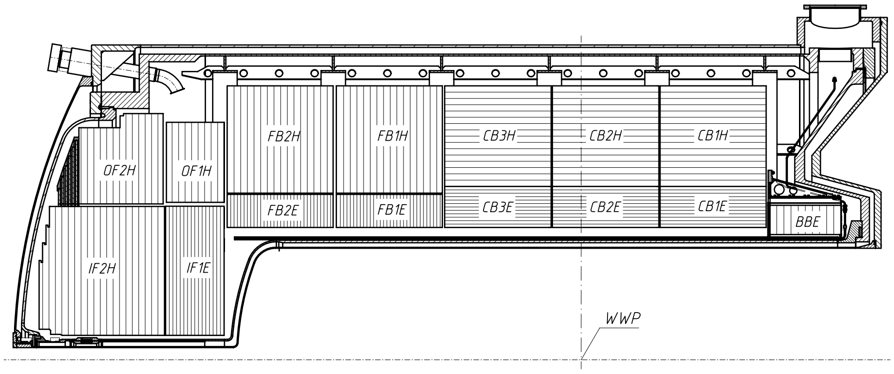

Figure 3.7: *Layout of the LAr Calorimeter.*

Closest to the interaction point is the EMC, which contains alternate layers of a 2.4 mm thick lead absorption plate and a 2.35 mm layer of LAr. The depth of the EMC varies between 20 and 30 radiation lengths, $\chi_\circ$, with θ. All wheels contain an electromagnetic section except the outer forward (OF) wheel due to its position (see figure 3.7).

The EMC is almost completely surrounded by the HAC. The exception is the backward region (the BBE wheel, see figure 3.7), where the hadronic section is absent due to the need to accommodate feed lines for the liquid argon cryostat. As a result, the EMC has a slightly larger angular acceptance than the HAC. The HAC has layers of 16mm thick stainless steel absorber alternating with 5mm sampling layers of LAr. It has a depth of 5 to 8 radiation lengths, λ, with the greatest depth in the forward direction.

The energy resolution for electrons in the EMC is $\sigma(E)/E \approx 0.12/\sqrt{E} \oplus 0.01$ (where E is in GeV), and for hadrons it is $\sigma(E)/E \approx 0.50/\sqrt{E} \oplus 0.02$ from both the EMC and HAC. The overall energy scale is known to 3% and 4% respectively.

3.5.2 SPACAL

The SPAghetti CALorimeter (SPACAL)[4] was designed to provide calorimetry in the backward region. Its primary task is the efficient identification of electrons and an accurate measurement of the electron's energy. It also provides a measurement of hadronic energy deposited in the backward region. The angular coverage of the SPACAL is $153^\circ \lesssim \theta \lesssim 177.5^\circ$. This means that electrons from DIS events with Q^2 as low as 1 GeV^2 are accessible in the SPACAL.

As with the LAr, the SPACAL is split into an electromagnetic and hadronic section. It has a more compact design than the LAr due to a more restricted space. The design incorporates a higher granularity than the LAr in order to make accurate measurements of the electrons scattering angle in the low Q^2 region. Both sections consist of scintillating fibres embedded in lead with the readout via photomultiplier tubes. The resolution has been studied using test beams at CERN. The electromagnetic section has a resolution of $\sigma(E)/E \approx 7.1\%/\sqrt{E} \oplus 1\%$ [97], whilst the hadronic section has a resolution of $\sigma(E)/E \approx 56\%/\sqrt{E} \oplus 3\%$ for pions and $\sigma(E)/E \approx 12.5\%/\sqrt{E} \oplus 3.8\%$ for electrons [98].

---

[4] The SPACAL was installed in 1995 to replace the Backward Electromagnetic Calorimeter (BEMC). As no data taken before 1995 is used here, only the SPACAL will be described. For a description of the BEMC see [92], for example.

3.5.3 The Plug Calorimeter

The Plug calorimeter closes a gap in acceptance between the beam pipe ($\theta \approx 0.3^\circ$) and the LAr calorimeter ($\theta \approx 3^\circ$). It is relatively crude and consists of 9 layers of copper absorber and 8 layers of silicon sampler. The energy resolution of the Plug is $\sigma(E)/E \approx 150\%/\sqrt{E}$.

3.6 Muon Detection

Two detectors are used by H1 primarily for the detection of muons. Firstly the iron return yoke of the magnet is instrumented and used to detect muons over almost the full angular range. Secondly, the forward muon detector is used as an independent measurement of muons in the forward direction. In addition, the LAr calorimeter can be used for the identification of muons through their ionization loss.

3.6.1 Instrumented Iron

Surrounding the superconducting solenoid and the major detector components of H1 is the iron return yoke of the magnet. This is instrumented with limited streamer tubes (LSTs). The primary purpose of this is muon detection. However, it has added value as a 'tail-catcher' calorimeter to detect any remnants of the particle showers that penetrate through the calorimeters.

The instrumented iron, or central muon detector (CMD), provides an angular coverage

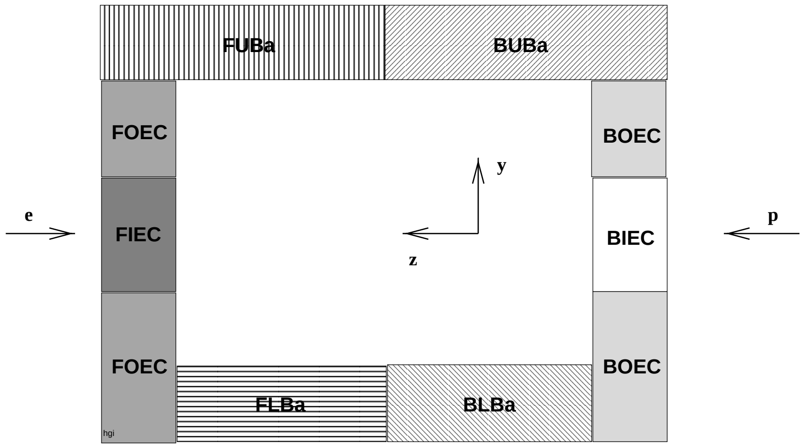

Figure 3.8: *The division of the instrumented iron into sections. The Barrel region is subdivided into four sections, each endcap into two sections.*

of $5^\circ \lesssim \theta \lesssim 175^\circ$, and is split into three sections; the central barrel, the forward endcap ($\theta \lesssim 35^\circ$) and backward endcap ($\theta \gtrsim 130^\circ$). Figure 3.8 shows the division of the instrumented iron. The central barrel consists of four sections; FUBa, FLBa, BUBa, and BLBa. The endcaps are each divided into inner (FIEC, BIEC) and outer (FOEC, BOEC) regions. There are 16 layers of LSTs in each section, placed in slots between layers of iron. Five of the layers of LSTs are equipped with strip electrodes to give a position measurement. The remaining 11 are equipped with pad electrodes which provide coarse energy measurements.

Figure 3.9 shows the internal structure of the LSTs. They have a single sense wire in the middle of each tube, running along the length of the tube. In the endcaps they are oriented in the x-direction, whilst in the barrel they run parallel to the z-axis. The position resolution is determined by the chamber geometry. Using the sense wires, a position resolution of order 4 mm in the direction perpendicular to the wire is achieved. A resolution of order 10 mm in the co-ordinate parallel to the wire is achieved using

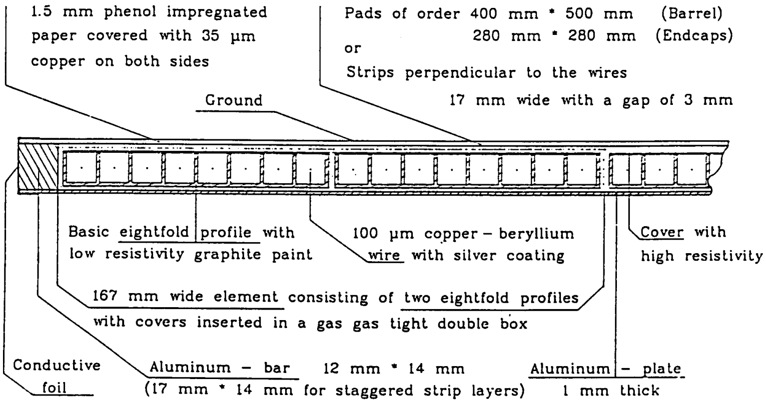

Figure 3.9: *Internal Structure of the Limited Streamer Tubes.*

the strips.

3.6.2 Forward Muon Detector (FMD)

The forward muon detector (FMD) [99] is located outside the iron return yoke of the magnet (see figure 3.3), and is used to detect and measure the momentum of muons produced with high momentum in the highly active forward region. The angular coverage of the FMD is $3^\circ \lesssim \theta \lesssim 17^\circ$.

The detector consists of 6 double layers of drift chambers and a toroidal magnet. Three of the double layers of drift chambers are located before and three after the toroid. In each set of three double layers, two have wires strung around the beam pipe, to measure θ, and one double layer has wires strung radially, to measure ϕ. Figure 3.10 shows the layout of the FMD.

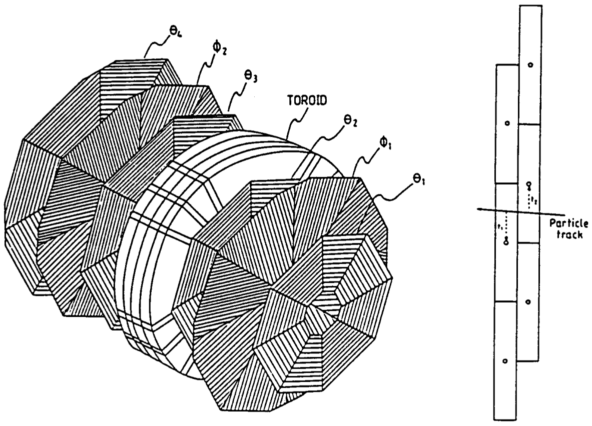

Figure 3.10: *Layout of the Forward Muon Detector. The left figure shows the overall layout. The right figure shows the relative positioning of drift chambers in each double layer.*

The toroidal magnet has an inner radius of 0.65m and an outer radius of 2.90 m. It has a length of 1.2 m, and a field which varies with radius from 1.75 T at the inner radius, to 1.5 T at the outer radius. From the curvature of the muon track due to the toroid, a momentum measurement is possible. This places an upper limit of 100 GeV on the muon momentum measurement due to the accuracy with which the curvature of the muon track can be measured. Muons with momentum below 5 GeV will be detected, but their momentum cannot be measured, as they will lose an average of 3 GeV of energy in the main body of the detector (FTD, LAr calorimeter and Instrumented Iron), and 1.5 GeV in the toroid. Muons with momentum below 3 GeV will not be detected by the FMD.

3.7 Forward Detectors

In order to identify diffractive events (see section 2.2.3), several detector components in the forward direction are used. These are; the forward part of the LAr calorimeter (see section 3.5), the Forward Muon Detector (see section 3.6.2) and the Proton Remnant Tagger (PRT). The PRT is situated around the beam pipe, 24m from the interaction region, in the forward direction. It consists of 7 layers of scintillator pairs, each shielded with lead. The angular acceptance of the PRT is $0.06^\circ \lesssim \theta \lesssim 0.17^\circ$.

3.8 Luminosity System

The H1 Luminosity System [100] has several important uses. It provides a fast online luminosity measurement, information which is used by the HERA accelerator operators who steer the beam so that the luminosity can be maximised. It provides an accurate absolute luminosity measurement after offline corrections have been made. The components can also be used for tagging specific physics events by detecting particles close to the beam pipe, e.g. electrons from photoproduction events, or photons from events with initial state radiation (ISR).

The luminosity system is located close to the beam pipe in the electron, or backward direction. It consists of an Electron Tagger (ET), located 33 m from the interaction point, and a Photon Detector (PD), at 103 m from the interaction point. The luminosity is determined by measuring the rate of the Bethe-Heitler process $ep \rightarrow ep\gamma$ [101]. This has a large, calculable cross-section. The online measurement is made by requiring an $e - \gamma$ coincidence in the ET and PD. The main source of background is from electrons interacting with residual gas in the beam pipe in the bremsstrahlung process $eA \rightarrow eA\gamma$. However, this contribution can be subtracted by using the electron pilot bunches to measure the rate of these events in the absence of Bethe-Heitler events.

3.9 Triggering

Within the HERA machine, an electron and/or a proton bunch crosses the H1 interaction point every 96 ns. This fact, combined with a very high background rate, makes a fast efficient trigger essential. The problem is compounded by the large number of channels to be read out ($\sim$ 270 000) and the long response times of some of the detector components compared to the bunch crossing time. For example, the drift time in the FMD can be up to $\sim 1.2\ \mu$s. If the trigger had to wait for all the information to become available before making a decision, the detector would be unused, or 'dead', for a very large fraction of the running time. In order to solve this problem, H1 uses a pipelined multi-level trigger system, as described below.

There are five levels to the H1 trigger system. Each must be passed in turn for an event to be recorded. The first four levels[5] are performed on-line, whilst the fifth level (L5) is performed off-line during the event reconstruction. The decision time and rates of the trigger levels used on-line are summarised in table 3.1.

Most detector components provide one or more trigger elements. These provide logical

---

[5] Level 3 has not yet been implemented, but will be used after the forthcoming upgrade.

Trigger Level	Time after Event	Typical Output Rate
L1	$2.3\mu s$	1 kHz
L2	$20\mu s$	100-200 Hz
L4	$\sim 100ms$	5 Hz

Table 3.1: *Decision time and typical output rate of the three trigger levels used on-line by H1.*

statements as to whether particular detector conditions have occurred (e.g. trigger element 36 indicates when there is a pair of hits in the first layer of the FMD). There are currently 192 trigger elements in total. The main trigger elements used in this analysis are described in more detail in section 3.9.1.

The output from each trigger element is sent to the central trigger [102] for each bunch crossing, where they are then combined into 128 logical combinations, known as sub-triggers, which form the first level of the trigger (L1). Each sub-trigger contains a mixture of criteria. Some criteria are designed to reject backgrounds, whilst others are designed to select particular physics channels. If any sub-trigger condition is fulfilled, then the detector read-out is stopped and the event information is sent to the second level (L2).

Due to the relatively long response time of some detector components, an L1 decision is made $\sim$ 2.3 μs, or 24 bunch crossings, after the event has taken place. In order to avoid the problem of the detector being dead for the following 24 bunch crossings, the detector information is stored in memory, or pipelined, until an L1 decision is made.

Some of the sub-triggers are used purely for monitoring the backgrounds. These sub-triggers often have a much higher rate than the physics sub-triggers, and so it is necessary to only read out a fraction of these events. In order to reduce the trigger rate to an acceptable level, a process known as pre-scaling is applied in H1. This process applies a programmable factor to each sub-trigger that determines what fraction of the events from that sub-trigger are recorded. For example, giving a sub-trigger a pre-scale factor of 100 means that only every 100^{th} event that satisfies the sub-trigger conditions is kept.

The pre-scale factors are chosen such that the physics output is optimised. As the background conditions and rates of individual triggers vary over time, four sets of pre-scale factors, each optimised for different conditions and rates and known as a trigger *phase*, are used. For example, phase 1 is optimised for use soon after data taking begins, when trigger rates and backgrounds are high, whereas phase 4 is used when both rates and backgrounds are low[6].

Once a decision to keep the event has been made at L1, the detectors dead time begins. This lasts until all the detector information has been readout and passed to level 4 (L4), or the event is rejected by L2. The dead time therefore depends on how long L2 takes to make a decision ($\sim 20\ \mu$s), and how long it takes to transmit the full event information to L4, which in turn depends on the rate at which L4 can process the events.

L2 is divided into two sections: a topological trigger (L2TT) [103] and a neural network trigger (L2NN) [104]. They receive more detailed information than is made available to L1 and are mainly used to process those physics triggers which are susceptible to

---

[6] In 1998 this procedure was upgraded so that pre-scale factors could be automatically adjusted online to take account of the current conditions and optimise the physics output. This new procedure is know as Autoprescale.

high backgrounds. This is necessary if large pre-scales are to be avoided for interesting channels. If L2 decides to reject the event, the L1 readout is immediately re-started. If L2 decides to keep the event, the full event information is sent to the L4 trigger. Once L4 has all the information, the L1 readout is re-started.

The L4 trigger consists of a farm of microprocessors which perform a limited reconstruction of the event. Firstly, L4 uses the reconstructed event to verify the L1 decision was correct. For example, if an L1 trigger looks for three central tracks, L4 checks that three central tracks were reconstructed. At least one L1 sub-trigger must fire, with that decision verified by L4, for the event to be accepted. The reconstructed event is then analysed to see if there was a *Hard Scale* process involved, e.g. a high momentum particle, a high-Q^2 event or a high energy jet. If a hard scale is found, the event is kept. If no hard scale is found in the event, a set of finders are applied to the event until one accepts the event. The finders are designed to select physics events of particular interest. Additionally, background finders are applied in order to reject obvious background events. If the event fails all the finders a Q^2 dependent downscaling factor is applied to the event. This procedure is very similar to the L1 pre-scaling scheme and a weight is given to any event selected at this stage (the weight is 1 if the event is accepted by any of the L4 finders or due to a hard scale being found in the event). L4 can process up to 30 events at the same time, at an input rate of $\sim$ 40 Hz. After passing L4, the events are written to tape, at a maximum rate of $\sim$ 10 Hz.

The fifth level of the trigger system (L5) is performed off-line. It involves a full reconstruction of the event and the classification of the event according to which type of physics event it is. Any event not falling into any of the predefined physics classes is rejected.

3.9.1 L1 Trigger Elements

Almost every detector component in H1 contributes to at least one of the trigger elements which are used by the L1 trigger. A brief description of the principle of operation of the main triggers relevant to this analysis is given below.

z-vertex trigger

The z-vertex trigger [105] uses information from the central proportional chambers (CIP and COP) and the first proportional chamber in the FTD (the FPC) to provide a fast, rough estimate of the z-coordinate of the event vertex. It does this by connecting all possible combinations of 4 or more hits in the chambers to form rays. The rays are then extrapolated back to the origin along the z-axis. A 16-bin histogram of where these rays are projected to intercept the z-axis is produced and a set of trigger elements uses this histogram to send information to the L1 trigger.

DCRϕ trigger

Information from the central drift chambers (CJC1 and CJC2) is used by the DCRϕ trigger to give track based trigger information. Hits from 16 out of the 56 wire layers of CJC1 and CJC2 are used. The hit patterns are compared to about 10,000 pre-defined masks, which are designed to mimic the hit patterns left by tracks originating at the interaction point. Possible tracks are classified into 'low' ($450 \lesssim p_t \lesssim 800$ MeV) or 'high' ($p_t \gtrsim 800$ MeV) momentum candidates separately for both negative and positive tracks. Trigger elements based on this information are then used by the L1 trigger.

Muon trigger

The muon trigger [92] uses information from 5 out of the 16 layers of the instrumented iron (a separate trigger uses information from the FMD, see [106]). The detector is divided into 64 modules. In the endcaps, a coincidence of hits on 3 out of 5 layers in a module is required to form an acceptable trigger. In the barrel region, 2 out of the 4 inner layers are required.

3.10 HERA Upgrade program

The HERA machine is currently undergoing a major upgrade program. The aim of this is to increase the luminosity by a factor of five and to provide a longitudinally polarised electron beam [107]. In order to make the best use of the new data taking conditions, H1 will is also being upgraded.

The tracking detectors in the forward region will be significantly enhanced. A new Forward Silicon Tracker (FST), covering the angular region $8° \lesssim \theta \lesssim 16°$, will be installed [108]. The FTD will be upgraded by installing three additional planer chambers [109]. This will enhance the efficiency and precision of track measurements in the forward region.

The z resolution of the CTD will be improved by replacing the CIZ and two planes of the CIP with five layers of cylindrical multiwire proportional chamber [110]. Several components will be serviced in order to repair performance degradation which has occurred over time. For example, the Plug calorimeter will be improved by using copper absorber plates sandwiched between plastic scintillators [111].

Due to the increased luminosity, the input rate to the trigger system will be higher. Therefore, there are several projects to improve the trigger system. There will be a new L1 jet trigger attached to the calorimeters [112]. The DCRϕ trigger will be replaced by a new Fast Track Trigger (FTT). The FTT will operate on all levels of the trigger system and will lower the p_t threshold for triggering on tracks from 300 MeV to 100 MeV [113]. Finally, levels 4 and 5 of the trigger will be merged into a single system [114].

Chapter 4

Selection of Inelastic J/ψ Mesons

This chapter will discuss the data selection used for the analysis. The analysis is split into two different kinematic regions: low-z and medium-z (the choice of regions will be discussed in chapter 5). The selection for each region is broadly the same, but there are differences related to the different signal-to-background ratios, kinematic region and event characteristics, which will be indicated where appropriate. The J/ψ's are identified via their decay into a pair of muons, hence much of this chapter will focus on how the muons are used for triggering and how they are identified.

4.1 Triggering

The selection of a suitable set of triggers is crucial. In an ideal situation, a set of independent triggers would be used: firstly to select the data, and secondly to provide independent checks on the efficiency of the triggers used to record the data. This is not possible in this analysis, however, due to several complicating factors. The events occur at a low rate relative to the background. Therefore, high thresholds are needed in order to keep the trigger rate at an acceptable level. Unfortunately, this reduces the efficiency of the trigger. The analysis also suffers from relatively low statistics (for example, the diffractive J/ψ analysis has over a factor of two more events [33]). Therefore, in order to obtain as many events as possible, a combination of triggers is used. The situation is further complicated because the triggers are not independent: they all identify possible J/ψ events via the event topology and the decay to muons, making the efficiency determination in data more tricky.

4.1.1 L1 Trigger

In the medium-z analysis, the choice of suitable sub-triggers differs between two run[1] periods. The first period consists of the 1996 data taking period, and the first part of the 1997 data taking period (up to run 193432). The second period is all the data taken after that during 1997. This change was made because a new sub-trigger suitable for this analysis became available during the 1997 data taking period.

Two sub-triggers, s19 and s22, are used throughout, whilst one, s15, is used in the second period only. The definition of the sub-triggers, in terms of the trigger elements, is given in table 4.1, with the trigger elements defined in table 4.2. Events which satisfy any of the chosen sub-triggers are selected for further analysis.

---

[1] A run is a term used to describe a unit of data taking in which the conditions are stable. A run lasts typically 30 minutes.

Sub-trigger	L1 Definition
s15	`(Mu_Bar||Mu_ECQ)&&DCRPh_Thig&&zVtx_sig`
s19	`Mu_Bar&&DCRPh_CNH&&zVtx_sig_1`
s22	`Mu_ECQ&&DCRPh_CNH&&zVtx_sig_1`
s56	`(SPCLe_IET>1||SPCLe_IET_Cen_2)&&DCRPh_Ta&&Mu_Any`

Table 4.1: *Definition of the L1 sub-triggers in terms of the trigger elements.*

Trigger Element	Definition
`Mu_Any`	at least one muon in the CMD
`Mu_Bar`	at least one muon in the barrel of the CMD
`Mu_ECQ`	at least one muon in the outer endcaps of the CMD
`DCRPh_CNH`	`DCRPh_Tc&&DCRPh_TNeg&&DCRPh_THig`
`DCRPh_Ta`	at least one track candidate
`DCRPh_Tc`	at least three track candidates
`DCRPh_TNeg`	at least one negative track candidate
`DCRPh_THig`	at least one $p_t > 800$ MeV track candidate
`zVtx_sig`	significant vertex candidate
`zVtx_sig_1`	significant vertex candidate (more restrictive)
`SPCLe_IET>1`	$\geq$ 2GeV of em energy in the outer region of the SPACAL
`SPCLe_IET_Cen_2`	$\geq$ 2GeV of em energy in the inner region of the SPACAL

Table 4.2: *Definition of the trigger elements.*

For the low-z analysis, a slightly different trigger mix is used. Again, the data is split into two periods due to an extra sub-trigger becoming available during 1997 (from run 179855). s19 and s22 are used throughout, with s56 used in addition during the second period. The sub-triggers are defined in detail in table 4.1. Events accepted by any of the chosen sub-triggers are selected for further analysis.

The L1 sub-triggers are designed to select events with the following characteristics:

s15 An inclusive muon trigger which will fire for the combination of a muon in the barrel or outer endcaps of the CMD, a high momentum track and a reconstructed vertex.

s19 An inclusive muon trigger which will fire for the combination of a muon in the barrel region of the CMD, at least 3 tracks (including at least one with high momentum and at least one negative track) and a reconstructed vertex.

s22 An inclusive muon trigger which will fire for the combination of a muon in the endcaps of the CMD, at least 3 tracks (including at least one with high momentum and at least one negative track) and a reconstructed vertex.

s56 An inclusive muon trigger which will fire for the combination of a muon in the CMD, at least one track and at least 2 GeV of electromagnetic activity in the SPACAL.

4.1.2 L2 Neural Network Trigger

In order to increase the efficiency of the trigger for J/ψ events, a new sub-trigger (s15) with less stringent track and vertex criteria was commissioned during the 1997 data taking period. In order to keep the rate of this trigger to an acceptable level and to avoid large pre-scales, a fast neural network was designed to provide a trigger decision for s15 at L2. The neural network uses more detailed information from the trackers, calorimeters and CMD than is available at L1. It was trained using J/ψ events selected by s19 and s22 during the 1995 and 1996 data taking periods, and background events from a special run during 1996. Its main advantage is an improved ability to reject background, thus enabling the L1 conditions to be relaxed and the efficiency improved.

For a more detailed description see [115].

4.1.3 L4 Trigger

There are several stages which the event must pass if it is to be accepted by the fourth level of the trigger system. A fast reconstruction of the event is performed and this information is used to analyse the event in more detail. The L1 decision is verified for each sub-trigger to ensure it was correct, otherwise the sub-trigger is reset. Furthermore, at least one of the selected L1 sub-triggers must fire, with that decision verified by L4, for the event to be accepted.

If the event passes the trigger verification, it is analysed to see if there is a *Hard Scale* process involved (see section 3.9). If a Hard Scale is found, the event is kept. If not, and the event is not rejected by the background finders, the physics finders are applied to the event. The finder relevant to this analysis is the High Mass finder. This loops over all tracks in the event and reconstructs the invariant mass of all pair combinations of tracks. If a pair with an invariant mass greater than 2 GeV is found, the event is kept. If the event has failed the finders, the L4 downscaling scheme is applied. For photoproduction events the weight is often large, typically about 40.

	1996	1997	Total
$\int \mathcal{L}dt$ delivered by HERA (pb^{-1})	14.5	33.4	47.8
$\int \mathcal{L}dt$ collected by H1 (pb^{-1})	9.9	28.2	38.1
$\int \mathcal{L}dt$ after run + HV selection (pb^{-1})	6.8	15.5	22.3
Satellite Correction	7.3%	6.5%	
$\int \mathcal{L}dt$ for analysis (pb^{-1})	6.3 ± 0.1	14.5 ± 0.2	20.81 ± 0.33

Table 4.3: *Summary of the integrated luminosity available from the 1996 and 1997 data taking periods.*

4.2 Run Selection and Luminosity Determination

Data recorded during 1996 and 1997 have been selected for this analysis. In order to obtain a reliable measurement of all the event quantities, it is required that the major detector components used in this analysis all have their high voltage switched on, and are included in the readout, in order for an event to be considered. The components are the LAr calorimeter, SPACAL, CTD, FTD, and the CMD. Furthermore, only runs where the trigger was in phase 2-4 are used. The phase 1 setup is excluded as it has high pre-scales for photoproduction triggers. This is because it is used at the beginning of data taking when detector components are being switched on (in particular the trackers are ramping up) and the data taking conditions are therefore unstable.

The integrated luminosity available for analysis from the selected run period corresponds to 20.81 ± 0.33 pb^{-1}. This is obtained from the total luminosity collected by H1 in the selected run period after correcting for several losses. The cut on the position of the z coordinate of the event vertex, z_{vtx}, of $|z_{vtx} - z_{nom}| < 40$ cm (see section 4.4), where z_{nom} is the z coordinate of the nominal interaction point, means that corrections for satellite bunches (i.e. early or late bunches), and any remaining events occurring outside of the selected vertex region, must be applied as these are included in the on-line luminosity measurement. The measurement must also be corrected for losses due to the high voltage of detector components not being on. The luminosity determination is summarised in table 4.3 for each year, and in total.

4.3 Muon Identification

The identification of a pair of unlike sign muons is a crucial part of this analysis and is the first stage of the off-line selection. The detectors which are used for the identification of muons in this analysis are the CMD and the LAr Calorimeter, both in conjunction with the CTD. The CTD is also used to obtain measurements of the muon properties from the muon tracks. The FMD is not used in this analysis due the limited number of extra events gained compared to the difficulties in making measurements in the highly active forward region. Additionally, the FMD must be used in conjunction with the FTD, from which measurements are not as reliable as those from the CTD.

4.3.1 Track Selection

In order to be considered as a muon candidate, a track is required. The track allows a good measurement of the muon momentum and angle, and is extrapolated into other detectors which are used for the identification. The muons produced in the decay of J/ψ's typically have a momentum of $\sim$ 2 GeV. This is a momentum for which the performance of the trackers is best, allowing fairly loose track selection cuts.

Only tracks in the CTD are considered here due to the poor performance and simulation of the FTD. Tracks are required to be constrained to the primary event vertex and leave at least 10 hits in the jet chambers (CJC1 and CJC2). Additionally, the tracks are required to start in the inner chamber (CJC1) and be at least 10 cm in length for $\theta < 150^{\circ}$. The latter requirement is relaxed to 5 cm for $\theta > 150^{\circ}$ due to the detector geometry.

4.3.2 Muon Identification in the CMD

Track segments in the CMD are linked to tracks in the CTD. In the barrel region of the CMD, at least two hits are required to form a track. In the endcaps, at least three (six) are required in the backward (forward) region. The differences are due to different background conditions and the different amounts and composition of material the muon must traverse in the various regions. A probability that the track segment in the CMD and the track in the CTD originate from the same muon is then calculated. The calculation is performed by extrapolating tracks from the CTD into the CMD and vice versa. The extrapolated tracks are then compared to the real tracks and a probability that the two tracks should be linked calculated. For a detailed description of this calculation, see [116]. Candidate combinations with a probability greater than 0.01% are accepted as muon candidates. Where the CMD track segment can be linked to more than one CTD track, the track with the highest link probability is used.

4.3.3 Muon Identification in the LAr Calorimeter

Muons with a momentum $p \gtrsim 1.5$ GeV penetrate through the calorimeters and reach the CMD. In order to identify lower momentum muons, and increase the overall identification efficiency, the LAr calorimeter is used.

Muons traversing the LAr calorimeter are minimum ionising particles. This is in contrast to other particles, such as electrons and pions, which cause showers of particles. The energy deposits left by muons, therefore, have different characteristics which can be exploited to identify muons. The procedure is as follows:

Tracks from the CTD are extrapolated to the LAr and two concentric cylinders are formed around these extrapolated tracks. The inner cylinder has a radius of 15cm, chosen such that the muons deposit almost all of their energy within it, whilst the outer cylinder has a radius of 30cm, so that hadronic showers are contained within it. Four estimators are then calculated based on the energy deposits and their location within these cylinders. They are:

1. The summed energy in the electromagnetic part of the calorimeter, within the inner cylinder, E_{EMC}.
2. The total energy within the outer cylinder, E_{HAD}.
3. The maximum distance of any energy deposit above the noise threshold, within the inner cylinder, from the entrance point of the track, L_{MAX}.
4. The sum of the distances from the entrance point of all the energy deposits above

the noise threshold within the inner cylinder, L_{HAD}.

The exact cut values for these estimators are given a strong angular dependence, to allow for the detector geometry, and an additional weak momentum dependence is imposed. They are chosen such that E_{EMC} and E_{HAD} are small (to reject backgrounds from electrons and pions), and L_{MAX} and L_{HAD} are large (so that the particle has penetrated deeply into the calorimeter). A weighted sum of the deviations of the estimators from the cut values is calculated and, from this sum, a quality is assigned to the muon candidate:

- *not a muon* (Quality=0),
- *poor* (Quality=1),
- *medium* (Quality=2),
- *good* (Quality=3).

For a more detailed discussion of the procedure for the identification of muons in the LAr calorimeter, see [116].

4.3.4 Muon Selection

The event selection in the analysis requires two unlike sign muons:

- A muon identified in the CMD
- A second muon identified in the CMD or in the LAr with quality ≥ 2.

The criteria for the first muon is stricter so that trigger efficiencies can be extracted reliably. All the L1 sub-triggers used in this analysis contain a muon trigger element which require at least one muon in the CMD. Hence for one of the sub-triggers to fire because of the presence of a J/ψ in the event, a muon must have been detected in the CMD. The cut on the LAr quality is chosen so that the probability for a pion to be misidentified as a muon is less than 5% [116].

The angular coverage of the CTD restricts the polar angle of each muon, θ_μ, to the range $20^\circ < \theta_\mu < 160^\circ$. The backward region ($\theta_\mu > 160^\circ$) is excluded due to the lack of adequate tracking information, whilst the forward region ($\theta_\mu < 20^\circ$) is excluded due to the higher backgrounds and complications arising from the need to use a different set of detector components in order to identify and measure the properties of any muons produced in this region. The polar angle requirement is further tightened to $20^\circ < \theta_\mu < 140^\circ$ in the low-z analysis. This is in order to increase the signal-to-background ratio by removing a region which suffers from excessive 'punch-through' background. This region corresponds to the BBE wheel of the LAr calorimeter (see figure 3.7) which does not contain a hadronic section. Hence there is less material

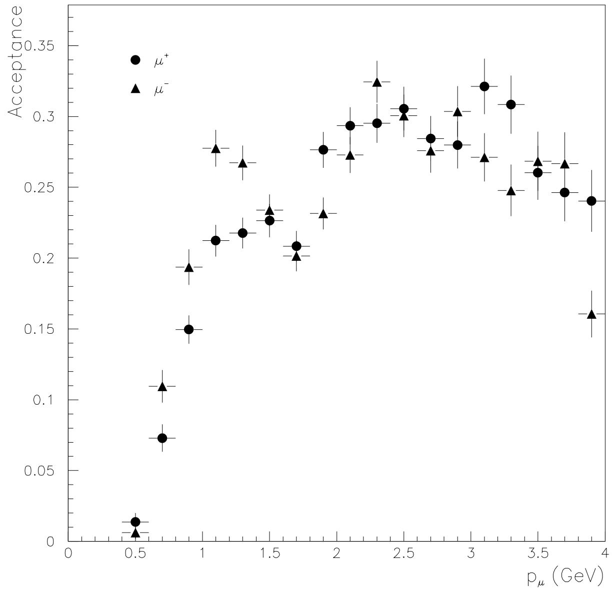

Figure 4.1: *The acceptance of the data selection, excluding triggers, as a function of the muon momentum. The acceptance is measured using a corrected Monte Carlo simulation.*

between the interaction point and the CMD in this region and so other particles, such as pions, could 'punch-through' more easily and be detected by the CMD. It can, however, be safely included in the medium-z analysis as there is a much greater signal-to-background ratio.

The momentum of each muon, p_μ, must be greater than 800 MeV. This is to ensure a reasonable efficiency for the identification of the muons. This is illustrated by figure 4.1, where the acceptance of the total selection chain (excluding the triggers) of the medium-z analysis is plotted as a function of the muon momentum, measured using the positive and negative muons separately. The acceptance is determined using Monte Carlo simulation with all the correction factors used in this analysis applied (see chapter 6), and is the fraction of the events generated that are selected after applying every criteria used in this analysis except the triggers. This can clearly be seen to rise sharply from zero at $p_\mu \sim 400$ MeV. The momentum cut is chosen such that the acceptance is above 10%. The acceptance dips slightly at $p_\mu \sim 1.5$ GeV. This corresponds to a region where the LAr muon identification efficiency is falling and the CMD efficiency is rising sharply (see section 6.2). The asymmetry between positive and negatively charged muons is due to the detector geometry. The CJC wires are inclined at 30° to the radial direction (see section 3.4.1). As the magnetic field curves positive and negative charged particles in opposite directions, this inclination results in a higher efficiency for the identification of tracks from negatively charged particles.

4.4 Final Event Selection

Events which pass the full trigger scheme, are from the selected run range, and contain a pair of unlike sign muons (selected according to the criteria given in section 4.3.4) are considered further. A cut on the invariant mass of the muon pair, $m_{\mu\mu}$, is made of $2.9 < m_{\mu\mu} < 3.3$. The selected events are considered to contain a J/ψ candidate. Further selection criteria are used to select J/ψ's produced in the desired way.

To select photoproduction events, a cut is made on any electromagnetic energy cluster (i.e. a region in the electromagnetic section of the calorimeters with energy deposited in) found in the event (excluding the electron taggers) in order to ensure the electron has not been detected in the main body of the detector. An event is considered to be a photoproduction event if no cluster is found with an energy greater than 5(8) GeV in the medium(low)-z analysis. The requirement is looser in the low-z analysis due to the possibility that the resolved photon remnant leaves energy deposits in the SPACAL. An inelastic J/ψ event will produce a final state which contains other particles along with the J/ψ. Therefore, it is required that the event contains at least three tracks. A cut of $|z_{vtx} - z_{nom}| < 40$ cm is applied in order to reduce the background from events which are not e-p collisions. Finally, events are selected only if they are in the kinematic region of interest. The choice of kinematic region will be described in section 5.3. Checks to ensure the selected data and simulation are correct are performed in chapter 6.

Chapter 5

Event Reconstruction

This chapter will describe the methods used in order to reconstruct the event properties, in particular the properties of the J/ψ and the kinematic variables used to describe the event. Finally a discussion on the choice of kinematic region for the measurement is presented.

5.1 Reconstruction of the properties of the J/ψ

The properties of the J/ψ are reconstructed solely from its decay muons. From these, the mass of the J/ψ candidate, and the momentum vector it is produced with are reconstructed. The CTD is used to measure the momentum vector of each muon, and from this information the invariant mass of the muon pair, $m_{\mu\mu}$, is calculated. The transverse momentum of the J/ψ, $p_{t,J/\psi}$, will be used extensively in this analysis. It is simply the vector sum of the p_t's of the muon pair.

5.2 Reconstruction of the Event Kinematics

There are several methods available for the reconstruction of the event kinematics at HERA. They include: the electron, double angle, Σ, $e\Sigma$, and the Jacquet-Blondel methods [117, 118]. The choice of method used depends on the type of event and the information available. In photoproduction events the electron is scattered through a very small angle and so will be undetected within the main body of the detector. All of the reconstruction methods require a detected electron with the exception of the Jacquet-Blondel method [118], which makes use of information from the hadronic final state only. For a description of the other methods, see [117] for example.

5.2.1 The Jacquet-Blondel Reconstruction Method

Using the Jacquet-Blondel method [118], y is reconstructed using the expression

$$y_{JB} = \frac{\sum_{had.fin.state}(E_i - p_{z,i})}{2E_e}, \tag{5.1}$$

where E_i and $p_{z,i}$ are the energy and z-component of the momentum of the i-th particle in the event, and E_e is the initial energy of the electron. The sum is over all particles produced in the event with the exception of the scattered electron, i.e. the hadronic final state. E_i and $p_{z,i}$ are determined by combining CTD tracks and calorimeter clusters. Any clusters not assigned to a track are assumed to be due to neutral particles (e.g. π° or γ's) and are treated accordingly. $W_{\gamma p}$ can then be obtained from y using

$$\begin{aligned} W_{\gamma p}^2 &= (P+q)^2 = Q^2(\frac{1}{x}-1)+m_p^2 \\ &= ys - Q^2 + m_p^2 \\ &\simeq ys, \end{aligned} \qquad (5.2)$$

because Q^2 is small and the proton mass, m_p, can be neglected.

In J/ψ analyses, the inelasticity variable z is a useful discriminatory variable (see section 2.3.2). This can be reconstructed using

$$\begin{aligned} z &= \frac{(E-p_z)_{J/\psi}}{2E_e y} \\ &= \frac{\sum_{i=\mu_1,\mu_2}(E_i - p_{z,i})}{\sum_{had.fin.state}(E_i - p_{z,i})}, \end{aligned} \qquad (5.3)$$

where the numerator is a sum over the J/ψ decay products only, and the denominator is a sum over all the hadronic final state (including the J/ψ).

5.2.2 Comparison between Generated and Reconstructed Kinematics

The accuracy and resolution of the technique used to reconstruct the kinematic variables can be tested using Monte Carlo simulations. Events are generated with known kinematics (y_{gen}, Q^2_{gen}, z_{gen} etc), passed through a full detector simulation, and finally a full event reconstruction is performed. The reconstructed quantities (y_{rec}, Q^2_{rec}, z_{rec}

etc) are then compared with the generated quantities in order to examine the accuracy and resolution of the reconstruction method.

The important kinematical variables for this analysis are $W_{\gamma p}$, z, and $p^2_{t.J/\psi}$. The reconstruction of $W_{\gamma p}$ is obtained directly from the reconstruction of y using equation 5.2, and the reconstruction of z depends on the y reconstruction via equation 5.3. Hence it is critical to have an accurate and reliable reconstruction method for three variables: y, z, and $p^2_{t.J/\psi}$. The Jacquet-Blondel reconstruction method has been studied using Monte Carlo simulations. Two different types of events have been used. Both are events with inelastic J/ψ photoproduction, one with the photon interacting directly, the other with a resolved photon interaction (see section 2.4.5). The results of this study are presented and discussed below.

y reconstruction

Figure 5.1 shows the results of the study into the accuracy and resolution of the y reconstruction. The figure shows histograms of $(y_{rec} - y_{gen})/y_{gen}$ for (a) direct Monte Carlo events and (b) resolved Monte Carlo events. Gaussian functions have been fitted to each histogram in the region $\mu \pm 2 \times RMS$, where μ is the mean and RMS is the root mean square of the histogram. A constant has been added to the fitted functions to account for the few events where the a J/ψ decay muon has been incorrectly identified. The Gaussians give a good description of the distributions for the region fitted. The mean of the Gaussians is $(2.37 \pm 0.25) \times 10^{-2}$ for direct events, and $(-0.96 \pm 0.40) \times 10^{-2}$ for resolved events, showing that there is no significant systematic shift in the

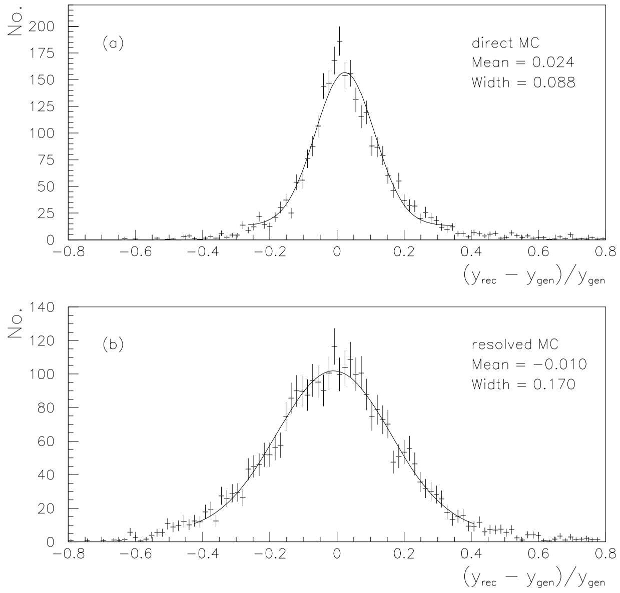

Figure 5.1: *The accuracy and resolution of the y reconstruction, using the Jacquet-Blondel method, as measured using (a) direct and (b) resolved Monte Carlo events. The mean and width of the fitted Gaussian is also shown.*

reconstruction. The width of the Gaussians is $(8.81 \pm 0.30) \times 10^{-2}$ for direct events, and 0.170 ± 0.008 for resolved events, giving an estimate for the resolution of the reconstruction method. The resolution is not as good for the resolved events due to the presence of the photon remnant in the backward region. Particles in this region will have larger values of $E - p_z$, and hence will have a large influence on the reconstruction of the kinematics. Additionally, some of the particles will be lost down the beampipe and this will upset the calculation using the Jacquet-Blondel method.

The results presented here are for events generated over the full kinematic range studied in the analysis. The study was repeated in each $W_{\gamma p}$ bin used in the analysis and the $W_{\gamma p}$ resolution was always smaller than the bin width. No significant systematic shift was observed in any bin.

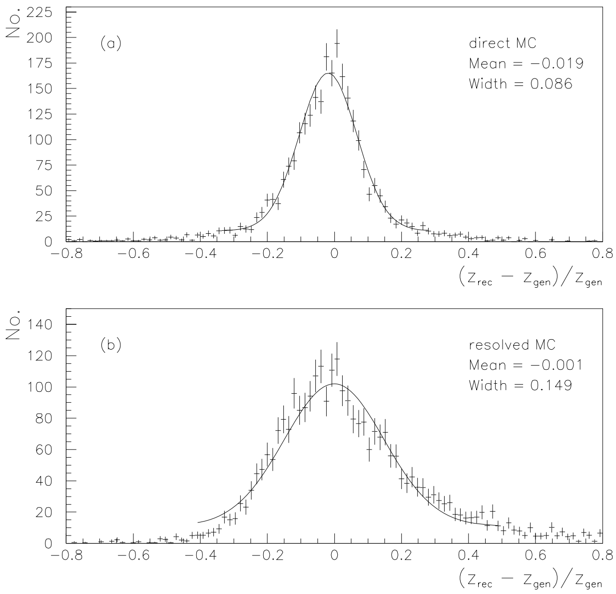

Figure 5.2: *The accuracy and resolution of the* z *reconstruction as measured using (a) direct and (b) resolved Monte Carlo events. The mean and width of the fitted Gaussian is also shown.*

z reconstruction

The z reconstruction depends on the y reconstruction through equation 5.3, and the measurement of the J/ψ decay products. Hence the study into the y reconstruction presented in the previous section already gives confidence in the accuracy of the z reconstruction. However it is still important to study it independently.

The results of the z reconstruction study is summarised by figure 5.2. The figure shows histograms of $(z_{rec} - z_{gen})/z_{gen}$ for (a) direct Monte Carlo events and (b) resolved Monte Carlo events. The analysis of the results is identical to that described in the previous section. The mean of the fitted Gaussians is $(-1.89 \pm 0.22) \times 10^{-2}$ for direct events, and $(-0.06 \pm 0.44) \times 10^{-2}$ for resolved events, showing that there is no significant systematic shift in the reconstruction of z. The widths are $(8.60 \pm 0.25) \times 10^{-2}$ and 0.149 ± 0.005 for direct and resolved events respectively. The resolution for resolved events is not as good as that for direct events due to the poorer resolution for the reconstruction of y. A bias can be observed in the histogram for resolved events, with more events where z_{rec} is overestimated than underestimated. This is due to the fact that the number of events increases as $z \rightarrow 0$. As $z \rightarrow 0$, less of the photons energy is transferred to the J/ψ and more is carried by the photon remnant. There will be more particles undetected in the beampipe in the backward direction, causing y to be underestimated and hence z to be overestimated. The corresponding asymmetry for the y reconstruction can be seen in figure 5.1, although it is not as noticeable.

The study was repeated in each individual bin in z used in the analysis. The resolution was always smaller than the bin width. No significant systematic shift was observed in any bin.

$p_{t.J/\psi}^2$ reconstruction

The reconstruction of $p_{t.J/\psi}^2$ depends solely on the measurement of the properties of the J/ψ decay products. Hence it is unaffected by undetected particles in the rest of the final state, unlike the y and z reconstruction. The results of the study into the $p_{t.J/\psi}^2$ reconstruction are presented in figure 5.3, with the upper plot being a histogram of $(p_{t,rec}^2 - p_{t,gen}^2)/p_{t,gen}^2$ for direct events and the lower plot is for resolved events. The histograms are analysed using the method described above. The means of the fitted Gaussians are $(9.50 \pm 1.00) \times 10^{-3}$ and $(4.98 \pm 0.94) \times 10^{-3}$, and the widths are

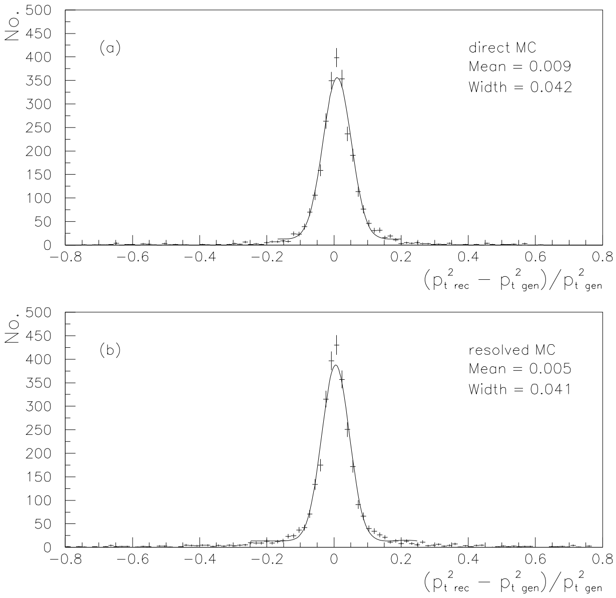

Figure 5.3: *The accuracy and resolution of the* $p^2_{t.J/\psi}$ *reconstruction as measured using (a) direct and (b) resolved Monte Carlo events. The mean and width of the fitted Gaussian is also shown.*

$(4.22 \pm 0.10) \times 10^{-2}$ and $(4.09 \pm 0.09) \times 10^{-2}$ for direct and resolved events respectively. No significant systematic shift in the reconstruction is observed. The resolutions for direct and resolved events are similar because the measurement depends solely on the J/ψ decay products and so should be independent of the production method of the J/ψ. The small differences that are observed are due to the different kinematics with which the J/ψ is produced.

The study was repeated in each $p^2_{t.J/\psi}$ bin used in the analysis, and the resolution was always smaller than the bin width. No significant systematic shift was observed in any bin.

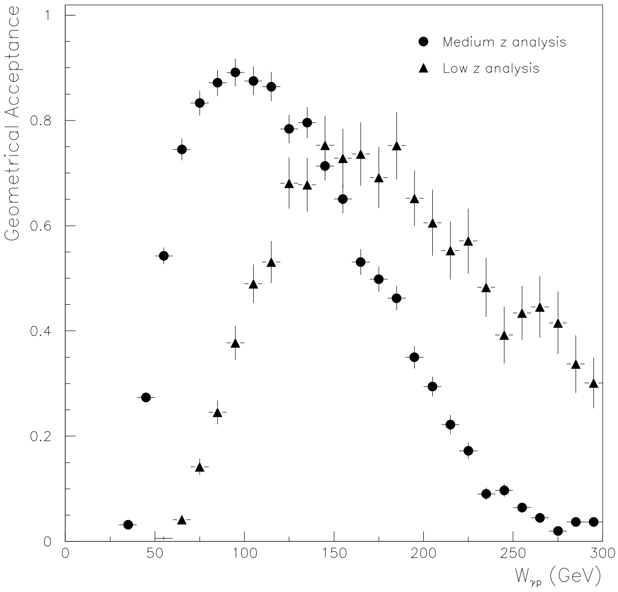

Figure 5.4: *Geometrical acceptance as a function of* $W_{\gamma p}$ *for the medium and low-z analyses. The low-z acceptance is only for the region* $0.07 < z < 0.3$. *The acceptance is determined using Monte Carlo simulation and contains all relevant correction factors.*

5.3 Selection of Kinematic Region

The choice of kinematic region in which the measurement is to be made is an important stage of the analysis. For this analysis, it is defined in terms of four kinematic variables: the photon virtuality Q^2, the photon-proton centre-of-mass energy $W_{\gamma p}$, the J/ψ's transverse momentum squared $p^2_{t,J/\psi}$, and the inelasticity variable z.

The simplest choice is the Q^2 range. Photoproduction events are events where the exchanged photon is real, i.e. $Q^2 = 0$ GeV^2. However, due to the angular acceptance of the SPACAL, in practice the best that can be achieved is to restrict events to the range $Q^2 < 1$ GeV^2, which is approximately the threshold above which the electron reaches the SPACAL.

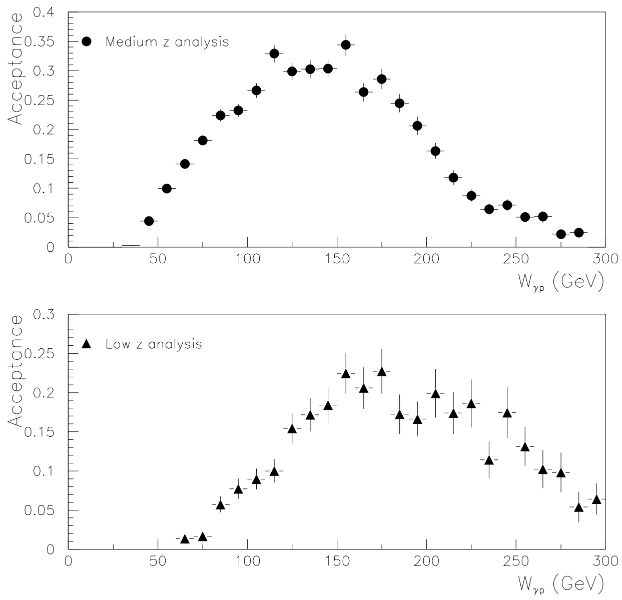

Figure 5.5: *Acceptance of the selection (excluding triggers) as a function of* $W_{\gamma p}$ *for the medium and low-z analyses. The low-z acceptance is only for the region* $0.07 < z < 0.3$. *The acceptance is determined using Monte Carlo simulation and contains all relevant correction factors.*

The analysis is split into two kinematic regions in z. This is because the $W_{\gamma p}$ acceptance function varies as a function of z. This is illustrated by figures 5.4 and 5.5. Figure 5.4 shows the geometrical acceptance (the fraction of events where the J/ψ decay muons are within the selected angular region), as a function of $W_{\gamma p}$, for the two analyses, whilst figure 5.5 shows the acceptance excluding triggers for the two analyses. The analysis is split into the medium ($0.3 < z < 0.9$) and low ($0.07 < z < 0.45$) z regions. The two regions overlap so that consistency checks between the two analyses are possible. The choice of kinematic region in $W_{\gamma p}$ and $p^2_{t,J/\psi}$ is discussed separately below for each analysis.

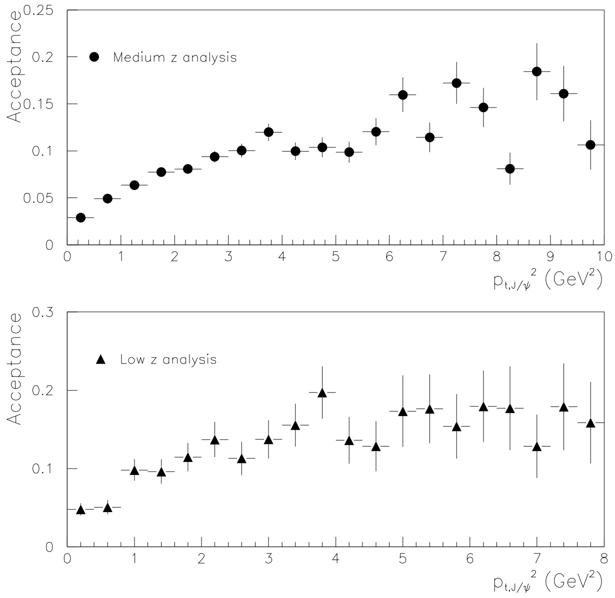

Figure 5.6: *Acceptance as a function of* $p_{t,J/\psi}^2$ *for the medium and low-z analyses. The low-z acceptance is only for the region* $0.07 < z < 0.3$. *The acceptance is determined using Monte Carlo simulation and contains all relevant correction factors.*

Medium-z Analysis

The $p_{t,J/\psi}^2$ region is chosen to be $p_{t,J/\psi}^2 > 1$ GeV^2. This is partly based on theoretical grounds in order to suppress the background from diffractive events [78]. Additionally, the acceptance falls as $p_{t,J/\psi}^2 \to 0$ GeV^2, as can be seen in figure 5.6. Restricting the $p_{t,J/\psi}^2$ range to $p_{t,J/\psi}^2 > 1$ GeV^2 excludes a region where the acceptance is below $\sim 5\%$.

The major limitation on the accessible $W_{\gamma p}$ region is the polar angle restriction on the decay muons. This is illustrated by figure 5.4, which shows the geometrical acceptance as a function of $W_{\gamma p}$. Requiring that the geometrical acceptance is above $\approx 20\%$ gives a $W_{\gamma p}$ range of $40 < W_{\gamma p} < 220$ GeV. This restriction is slightly modified when the total acceptance excluding triggers, shown in figure 5.5, is studied. Requiring that the

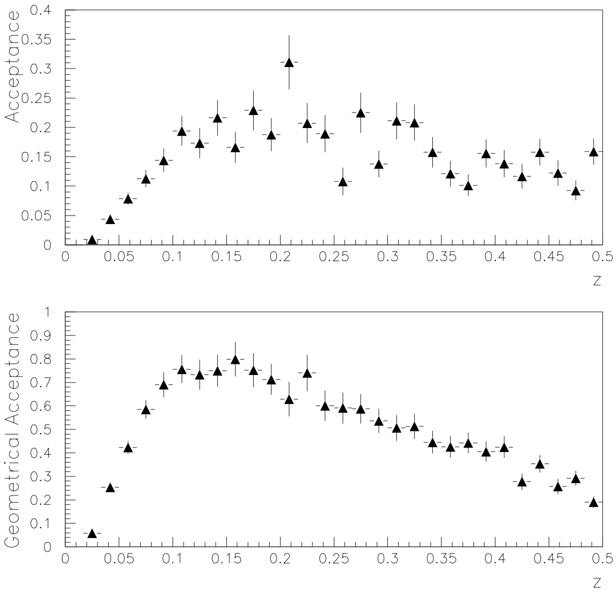

Figure 5.7: *Acceptance and Geometrical Acceptance of the low-z analysis, as a function of z. The acceptance is determined using Monte Carlo simulation and contains all relevant correction factors.*

acceptance (excluding triggers) is above ≈ 10% gives a range of $50 < W_{\gamma p} < 220$ GeV.

Low-z Analysis

The primary purpose of the low-z analysis is to measure the cross-section in the region $z < 0.3$. The region $0.3 < z < 0.45$ is included to provide consistency checks with the medium-z analysis. The choice of kinematic region is therefore optimised for the region $z < 0.3$. All figures referred to in this section only consider this region in z.

Unfortunately, there is still a restriction on how low in z the analysis can reach. This is illustrated by figure 5.7, which shows the geometrical acceptance and the acceptance excluding triggers of the low-z analysis, as a function of z. Both can be observed to fall to 0% at $z \sim 0.02$. Requiring that the acceptance is above $\sim 10\%$ restricts the analysis to the range $0.07 < z < 0.45$.

The background from diffractive events is expected to be predominantly at medium to high-z [78]. Therefore, the theoretical arguments used for the $p^2_{t,J/\psi}$ cut in the medium-z region are not relevant for the low-z region. However, the acceptance is very low below $p^2_{t,J/\psi} \sim 1$ GeV^2 (see figure 5.6). For this reason, and for consistency with the medium-z analysis, the cross-section measurements will be performed in the same $p^2_{t,J/\psi}$ region as in the medium-z analysis.

The geometrical acceptance (see figure 5.4) illustrates the restriction to a different $W_{\gamma p}$ region in the low-z analysis. The total acceptance (excluding triggers) is shown in figure 5.5. Requiring that this is above $\approx 15\%$ gives a $W_{\gamma p}$ range of $120 < W_{\gamma p} < 250$ GeV.

Chapter 6

Correction of the Data

In order to extract a cross-section measurement from the data, corrections for effects such as detector acceptances, muon identification efficiencies and trigger efficiencies must first be made. This is done using Monte Carlo simulations of the events and the full detector response. This chapter describes the various checks made on the Monte Carlo simulation in order to ensure that it correctly describes the data. Differences between the data and Monte Carlo have been found and the correction factors applied in order to correct the discrepancies are described where appropriate. Finally, the possible systematic errors remaining are described and summarised.

6.1 Trigger Efficiencies

6.1.1 L1 Trigger Elements

The L1 sub-triggers used in this analysis are not fully independent of each other. Additionally, measuring the efficiency of the sub-triggers used in this analysis using data recorded by sub-triggers which are completely independent of those used here (i.e. they contain no trigger elements from any of the detectors which provide trigger elements for this analysis) is not possible due to limited statistics. To avoid this problem, the efficiencies of the individual trigger elements, that are combined to form the sub-triggers used in this analysis, are measured using both data and Monte Carlo events separately. This can be done as enough data events can be obtained using sub-triggers independent of any given trigger element to measure the efficiency of the trigger element in a fully independent way. This section will discuss the trigger element efficiencies as measured for the medium-z analysis (similar results were obtained for the low-z analysis), with the exception of the SPACAL trigger elements as they are only used in the low-z analysis.

The muon trigger element efficiencies are measured in data using a sample of diffractive J/ψ events. This is because there are sub-triggers designed to select these events based on their topology (i.e. they fire for events with just two tracks) and which do not contain a muon trigger element. Hence a relatively high statistics data set can be obtained to measure the efficiency. Additionally, the J/ψ decay muons will be produced such that their distribution as a function of momentum, p_μ, and polar angle, θ_μ, is very similar to those from the decay of inelastic J/ψ's.

The selection of the diffractive J/ψ's is broadly the same as for the main analysis, described in chapter 4. The differences are in the number of tracks, which is required to be two, and triggering. The sub-trigger selection is that the event must fire at least one sub-trigger, at all levels, that is completely independent of the CMD. This ensures that the data sample is independent, as the event has been recorded irrespective of whether the trigger element under investigation has fired.

The efficiencies of the other trigger elements are all measured using a sample of inelastic J/ψ events. This is because these trigger elements are sensitive to the event topology. The only change from the selection described in chapter 4 is in the trigger selection. The events must fire at least one sub-trigger, at all levels, that is completely independent of the trigger system which contributes the trigger element under study. For example, for the measurement of the `DCRPh_Tc` efficiency, the event must fire at least one sub-trigger which does not contain any trigger element from the DCRϕ trigger. This ensures that independent data samples are used, although it does limit statistics.

Monte Carlo events are also used to measure the efficiencies. Monte Carlo events are selected using the selection criteria described in chapter 4, excluding the trigger selection, for all trigger element efficiency measurements. Full corrections (described later in this chapter) are applied to the Monte Carlo events. For the medium-z analysis, direct Monte Carlo events are used. For the low-z analysis a mixture of direct and resolved Monte Carlo events are used. By comparing the efficiencies obtained from the data and Monte Carlo events, a check can be performed as to whether the Monte Carlo simulation is accurately representing the behaviour of the trigger system.

Figure 6.1 compares the efficiencies of the individual muon trigger elements, as measured using data and Monte Carlo events separately. The results are shown as a function of the momentum (p_μ) and the polar angle (θ_μ) of the muon with the highest transverse momentum. For the `Mu_Bar` and `Mu_ECQ` efficiency measurements an additional requirement was made on the events that they have a muon within the angular coverage of the trigger element. This is reflected in the `Mu_ECQ` efficiency measurement as a function of θ_μ where there is a gap in the central region not covered by this trigger element. The agreement between data and Monte Carlo is good, with the remaining small differences propagated into the final results as a systematic error in each case.

Figure 6.2 shows the efficiencies of the main DCRϕ and zVtx trigger elements used in this analysis. The results are shown as a function of p_μ of the muon with the highest p_t and the event multiplicity (N_{tracks}). The agreement between data and Monte Carlo is again good. The efficiency of the DCRϕ trigger elements is higher in the Monte Carlo than in the data for low multiplicity events. Correcting for this inefficiency changed the results by much less than the systematic error quoted later, and so it will therefore remain uncorrected and be incorporated into the systematic error.

The SPACAL trigger element efficiency was measured using a sample of events from the low-z analysis. The event selection was as described in chapter 4, with the exception of the trigger selection where it was required that at least one sub-trigger that does not contain any SPACAL trigger element fired at all levels. Additionally, the trigger elements fire when there is more than 2 GeV of energy deposited in a region of the

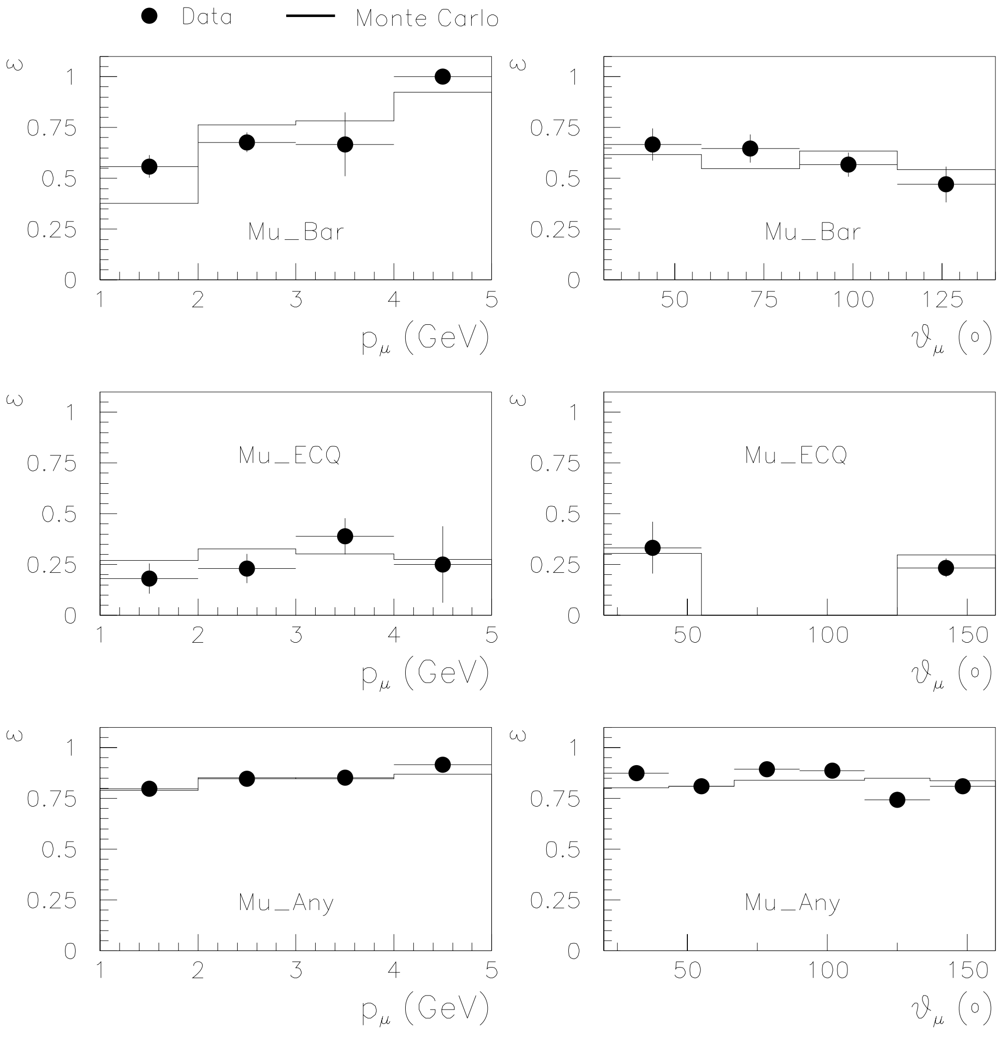

Figure 6.1: *Efficiencies of the muon trigger elements as a function of the muon momentum* (p_μ) *and polar angle* (θ_μ).

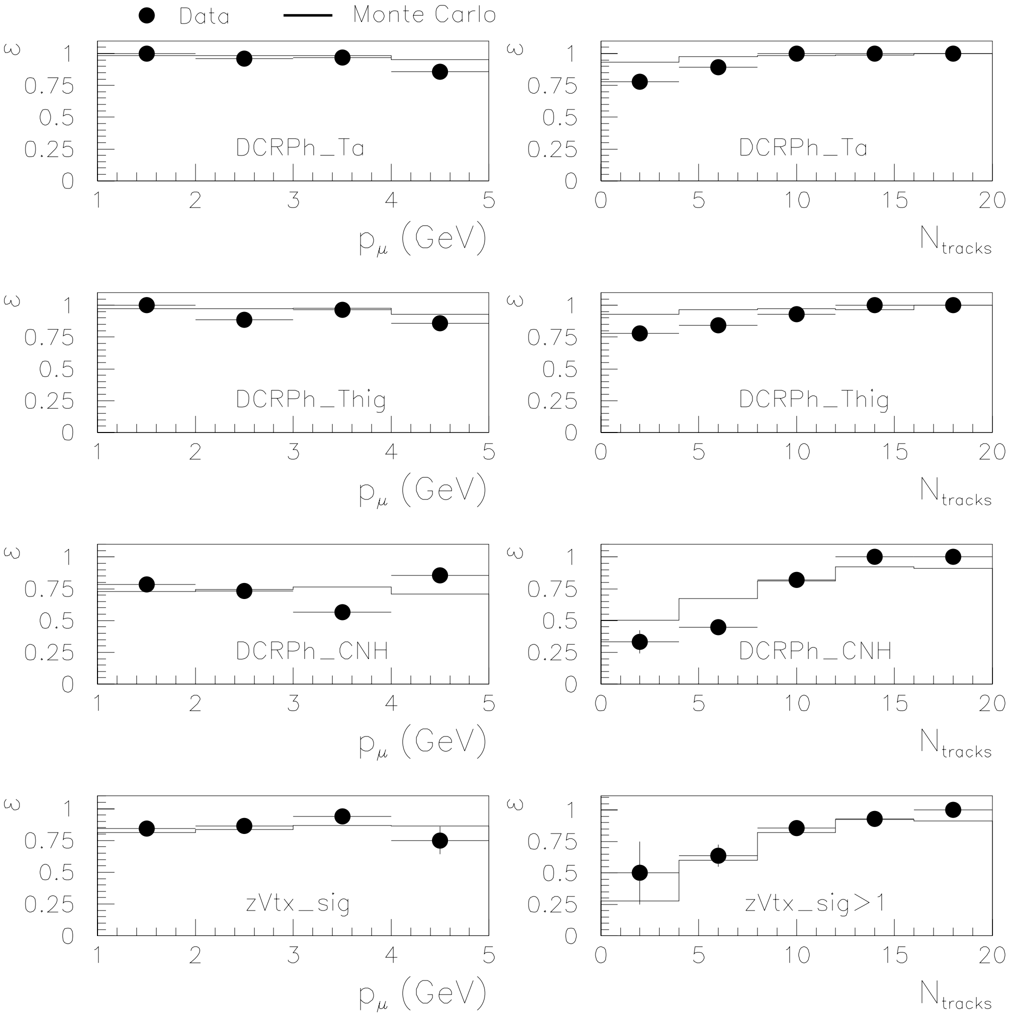

Figure 6.2: *Efficiencies of the track based trigger elements as a function of the muon momentum (p_μ) and event multiplicity (N_{tracks}).*

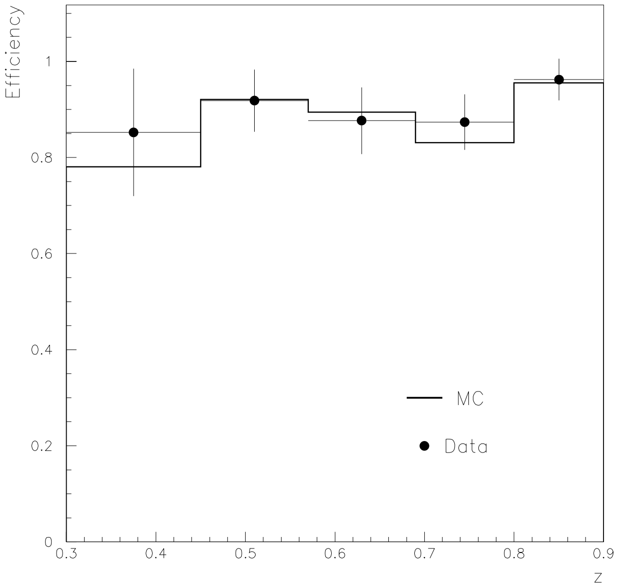

Figure 6.3: *L2NN Efficiency as a function of z as measured using data and Monte Carlo.*

SPACAL, therefore, it was required that there was at least 2 GeV of energy deposits reconstructed in the SPACAL. Unfortunately, the measurement of the efficiency is limited due to a lack of statistics. The overall efficiency in data is $27.3 \pm 6.7\%$, and in Monte Carlo it is $33.1 \pm 2.3\%$.

6.1.2 L2NN Trigger Element

The efficiency of the L2NN trigger element is measured using data selected by subtriggers s19, s22 and s87 (s87 fires for the combination of a muon in the CMD, a track and an electron in one of the electron taggers), which also pass the event selection chain. The efficiency is then the fraction of those events which fire s15 at L1 that also fire the L2NN trigger element. The efficiency is determined using both data and Monte

Carlo events, and is found to be $87.6 \pm 4.0\%$ and $87.2 \pm 0.6\%$ respectively. The variation with the kinematic variables, shown in figure 6.3 as a function of z for example, is flat, with good agreement between data and Monte Carlo simulation. The Monte Carlo efficiency will be used to correct the data, with the error on the data efficiency used to estimate the systematic error.

6.1.3 L4 Trigger

The L4 trigger does not need to be simulated in the Monte Carlo because the efficiency can be measured in data, and then the Monte Carlo can be corrected for any inefficiency. The efficiency with which L4 verifies the L1 sub-trigger decision can be measured directly using real events which have passed another sub-trigger at all levels (e.g. the s19 verification efficiency could be measured using events which have passed s15 at L1, L2 and been verified as passing s15 at L4). The efficiency is then the fraction of those events accepted by an L1 sub-trigger, for which the decision is verified at L4. The L4 verification for all the sub-triggers used in this analysis is more than 95% efficient with the exception of s19, for which the verification efficiency is only $83.7 \pm 2.9\%$. The Monte Carlo is corrected for this inefficiency by applying a weight of 0.837 to all Monte Carlo events which pass s19 and no other sub-trigger in use in the analysis. A weight of 1 is applied to all other events. The L4 verification efficiencies are summarised in table 6.1

The efficiency of the High Mass finder should be $\sim 100\%$ because all the cuts applied by the High Mass finder are repeated and, in many cases, tightened in the analysis.

L1 sub-trigger	L4 Verification Efficiency
s15	$\approx 100\%$
s19	$83.7 \pm 2.9\%$
s22	$95.7 \pm 2.3\%$
s56	$\approx 100\%$

Table 6.1: *Summary of the efficiencies with which the L1 sub-trigger decisions are verified by L4.*

This can be checked using the L4 weights. The presence of any event with a weight greater than 1 would be a sign of inefficiency, because it would indicate that the event had failed the High Mass finder. As expected, no events with a weight greater than 1 were found in either the medium or low-z analyses. Hence it can be concluded that the High Mass finder is $\approx 100\%$ efficient.

6.2 Muon Identification Efficiency

The efficiency of the muon identification is measured in the data using a sample of diffractive J/ψ events as this provides a pure sample of muons which is independent of the muon triggers and the data under study, and has higher statistics. This efficiency is then compared to the efficiency measured using direct Monte Carlo events (the same results were obtained using resolved Monte Carlo events) and any differences are either corrected for or incorporated into the systematic error. The events are selected by requiring that the event contains only two tracks which are from unlike-sign particles, one of which is identified as a muon, and that the invariant mass of the pair falls within the J/ψ mass peak ($2.9 < M_{\mu\mu} < 3.3$ GeV). For the LAr efficiency measurement, the

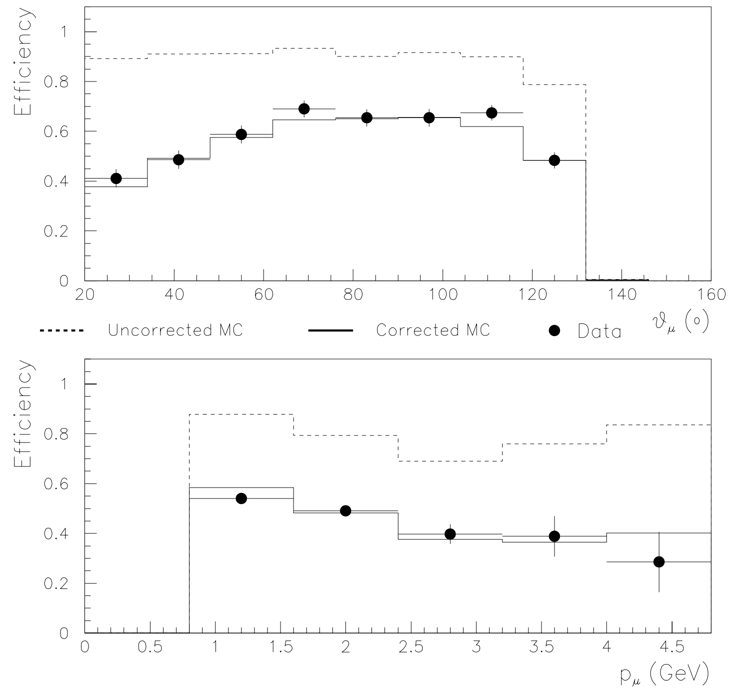

Figure 6.4: *Muon identification efficiency in the LAr calorimeter for data and Monte Carlo as a function of the polar angle, θ_μ, and momentum, p_μ, of the muon. The Monte Carlo is shown before and after a correction factor, discussed in the text, is applied.*

first muon is required to be identified in the CMD, whilst for the CMD efficiency measurement the first muon can be identified in either the CMD or the LAr with a quality ≥ 2. The efficiency is then the fraction of events where the second track is identified as a muon by the relevant detector.

The LAr muon identification efficiency, determined using this method, is shown in figure 6.4 as a function of the momentum, p_μ, and polar angle, θ_μ, of the muon. The efficiency measured using the Monte Carlo simulation (dashed line) fails to agree with the efficiency measured in data (points), an effect which has also been seen in other analyses (see [80] or [119], for example). In order to correct this, the Monte Carlo is re-weighted as a function of the polar angle of the muon, θ_μ, for those events where a

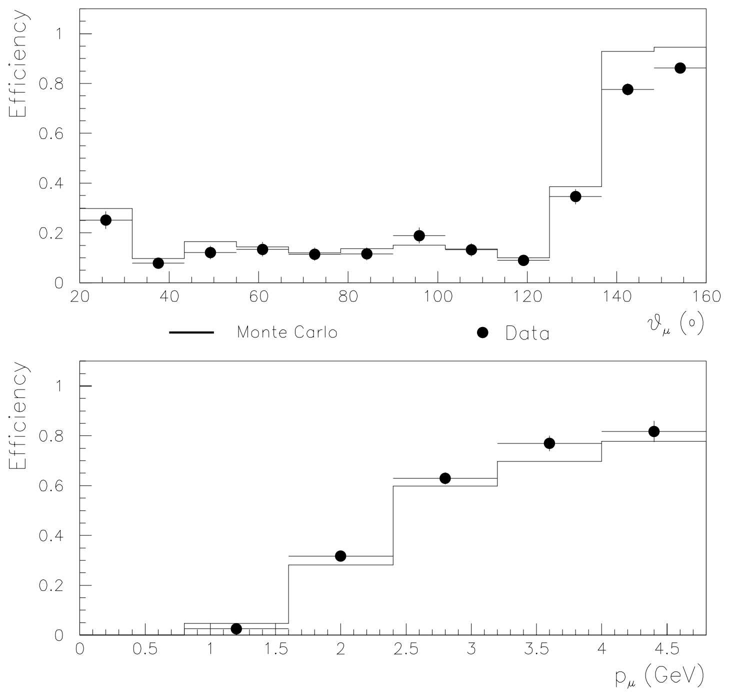

Figure 6.5: *Muon identification efficiency in the central muon detector for data and Monte Carlo as a function of the polar angle, θ_μ, and momentum, p_μ, of the muon.*

muon is identified by the LAr only. The function is determined by fitting a second-order polynomial to the ratio of the efficiencies in data and Monte Carlo. The re-weighting function is:

$$f(\theta_\mu) = 0.119 + (1.41 \times 10^{-2}) \cdot \theta_\mu - (7.91 \times 10^{-5}) \cdot \theta_\mu^2. \tag{6.1}$$

The corrected Monte Carlo efficiencies (solid lines) agree with the efficiency measured using data, as can be seen in figure 6.4, as a function of both the polar angle and momentum of the muon. The efficiency falls slightly with momentum because the identification algorithm is optimised for low momentum muons.

The muon identification efficiency in the CMD, as a function of θ_μ and p_μ, is shown in figure 6.5. The agreement between data and Monte Carlo is more than reasonable in this case. Small differences are present but these are taken account of as a systematic error. The efficiency rises with momentum because the probability that a muon reaches the CMD rises with momentum. The muon requires $p_\mu \sim 1.5$ GeV to penetrate the calorimeters and reach the CMD. This, however, varies with polar angle, a fact reflected by the θ_μ efficiency distribution. The peak in efficiency at $\theta_\mu \gtrsim 140°$ is due to the absence of the BBE wheel of the LAr calorimeter. Hence a muon will deposit less energy before reaching the CMD and a greater proportion will reach the CMD in this region. The main differences between the data and Monte Carlo are the higher efficiency in the data at high momentum ($p_\mu \gtrsim 2$ GeV) than in Monte Carlo and the lower data efficiency at large polar angle ($\theta_\mu \gtrsim 140°$) than in Monte Carlo. Correcting for these effects did not affect the final results in any significant way and so this too is included in the systematic error.

Figure 6.6 shows the total muon identification efficiency, i.e. the efficiency for the identification of a muon by either the LAr or the CMD. The plots reflect the features of the efficiency plots for the individual detectors. Both the raw Monte Carlo efficiency and that after correcting the LAr efficiency are shown. The average identification efficiency for a single muon is $70.3 \pm 1.0\%$ in data and $70.4 \pm 0.1\%$ in Monte Carlo. The analysis requires that one of the muons is identified in the CMD. The average identification efficiency for a single muon in the CMD is $34.0 \pm 1.0\%$ in data and $31.4 \pm 0.1\%$ in Monte Carlo. The average total efficiency for the identification of a pair of muons in this analysis is therefore $23.9 \pm 1.3\%$ in data and $22.1 \pm 0.1\%$ in Monte Carlo.

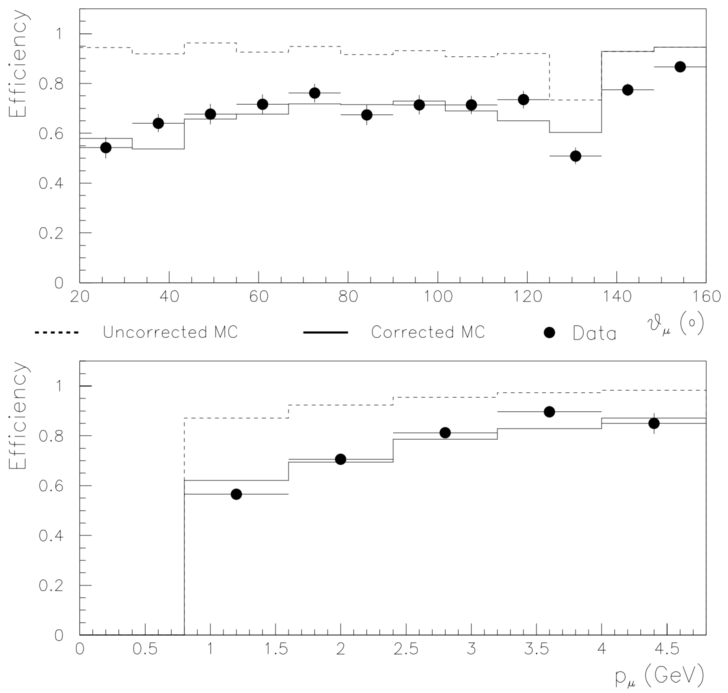

Figure 6.6: *Total muon identification efficiency for data and Monte Carlo as a function of the polar angle, θ_μ, and momentum, p_μ, of the muon.*

6.3 *z* vertex distribution

The observed z_{vtx} distribution does not exactly match the simulated distribution, as can be seen in figure 6.7 where the z_{vtx} distribution for the 1997 data (points) is compared with that from the resolved Monte Carlo events simulated for the 1997 data taking conditions (dashed line). Therefore, the cut of $|z_{vtx} - z_{nom}| < 40cm$ (see section 4.4) would introduce a bias in the cross-section measurement. In order to compensate for this, Gaussian functions are fitted to the z_{vtx} distributions in both data and Monte Carlo. The Monte Carlo is then re-weighted, as a function of z_{vtx}, using the ratio between these two Gaussian distributions, so that the corrected Monte Carlo z_{vtx} distribution (solid line) matches the data distribution closely. However, some small

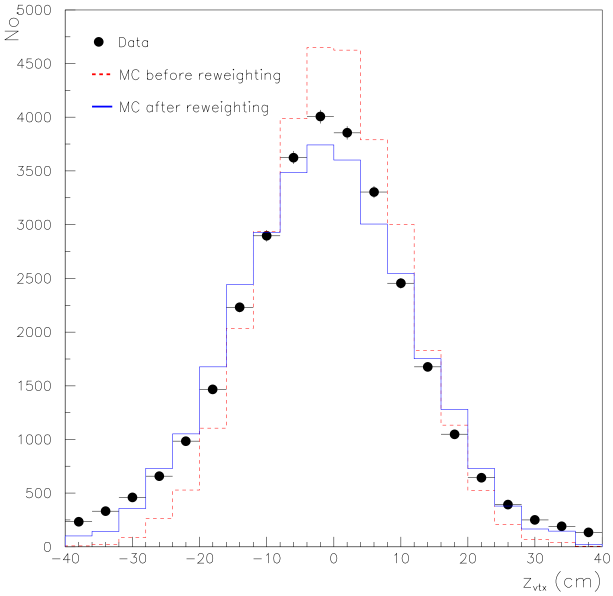

Figure 6.7: *The z-vertex distribution for the 1997 data taking period as observed in data and the resolved Monte Carlo. The Monte Carlo is shown before and after re-weighting.*

differences between the data and Monte Carlo distributions remain (see figure 6.7). These will be accounted for through a systematic error. This procedure is repeated for each set of simulated Monte Carlo events separately.

6.4 $p^2_{t,J/\psi}$ Re-weighting

The Monte Carlo generator EPJPSI (see section 2.6) generates events using a leading order calculation. As a consequence the $p^2_{t,J/\psi}$ distribution of the events generated for direct photoproduction does not correctly describe the distribution of the data events selected for the medium-z analysis. This is illustrated by figure 6.8, where the distribution of events in the medium-z analysis, in data (points) and Monte Carlo (dashed line), is plotted as a function of $p^2_{t,J/\psi}$. The Monte Carlo $p^2_{t,J/\psi}$ distribution

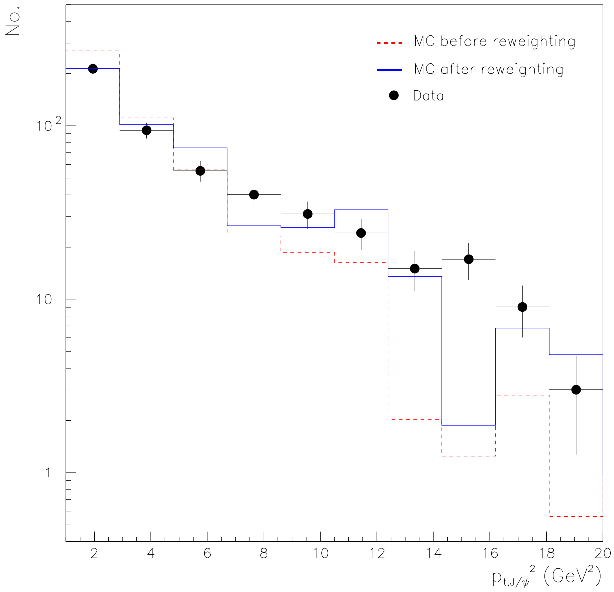

Figure 6.8: *Number of events selected for the medium-z analysis as a function of* $p_{t,J/\psi}^2$ *in data and Monte Carlo. The Monte Carlo is shown before and after a* $p_{t,J/\psi}^2$ *dependent re-weighting function, discussed in the text, is applied.*

falls too steeply. The direct Monte Carlo events are re-weighted as a function of $p_{t,J/\psi}^2$ in order to match the distribution of the data. The re-weighting function is determined by fitting an exponential function, $f(p_{t,J/\psi}^2)$, given by

$$f(p_{t,J/\psi}^2) = \exp\,(a + b \cdot p_{t,J/\psi}^2), \tag{6.2}$$

to the ratio of the number of events in data and Monte Carlo as a function of $p_{t,J/\psi}^2$, with a and b allowed to vary freely. The results of the fit are $a = -0.35 \pm 0.08$ and $b = (7.16 \pm 1.32) \times 10^{-2}$. The effect of the re-weighting is illustrated by figure 6.8, where the re-weighted Monte Carlo distribution (solid line) now has the correct $p_{t,J/\psi}^2$ dependence.

6.5 Comparison Between Data and Monte Carlo

The most important comparisons between data and Monte Carlo have already been discussed, along with all the correction factors that are applied. In addition to those already discussed, the Monte Carlo simulation has been compared with the data in as many ways as possible in order to detect any possible discrepancies between the simulation and the data. This section will present and discuss some of the most relevant comparisons.

Figures 6.9 and 6.10 show control plots for the medium-z and low-z analyses respectively. They are comparisons between some important distributions from data and Monte Carlo events. The distributions compare the properties of the decay muons ((a) the angular distribution, θ_μ, and (b) momentum, p_μ), the event kinematics ((c) $W_{\gamma p}$ and (d) z), detector effects ((e) the radial track length of the muons and (f) the number of hits in the CMD from each muon), and finally a check that the remainder of the hadronic final state is correctly simulated is performed by examining (g) the $(E - p_z)$ sum excluding the J/ψ and (h) the net p_t of the hadronic final state excluding the J/ψ. No subtraction for the non-resonant background under the J/ψ mass peak has been performed for the data due to limited statistics, and the Monte Carlo has been normalised to the data.

In both analyses, most of the plots show good agreement between the data and Monte Carlo. The exceptions are the θ_μ distribution in both analyses, and the $W_{\gamma p}$ distribution in the medium-z analysis. The differences in the medium-z analysis are understand-

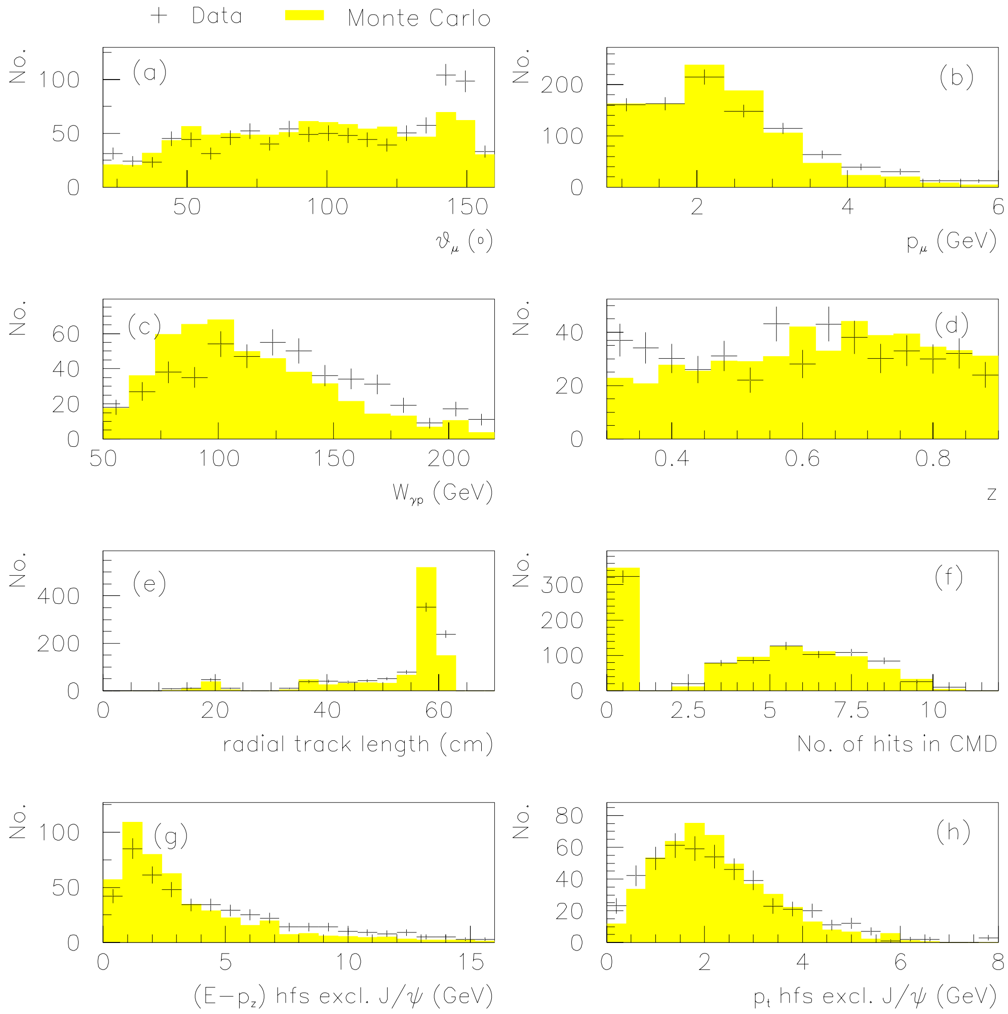

Figure 6.9: *Comparison between data and the Monte Carlo simulation for the medium-z analysis. The plots compare (a) the polar angle of the muons, θ_μ, (b) the muon momentum, p_μ, (c) $W_{\gamma p}$, (d) z, (e) the radial track length of the muons, (f) the number of hits in the CMD from each muon, (g) the $(E - p_z)$ sum for the hadronic final state excluding the J/ψ, and (h) the p_t of the hadronic final state excluding the J/ψ.*

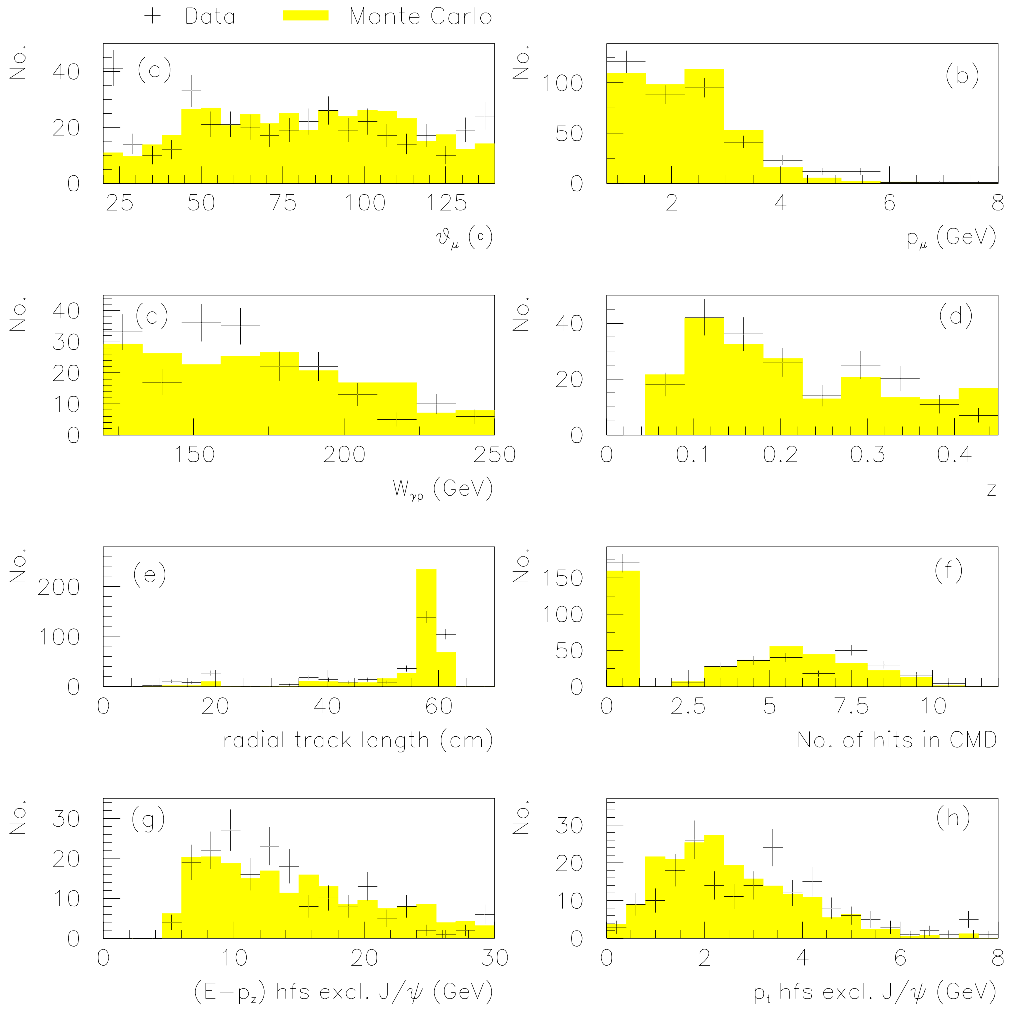

Figure 6.10: *Comparison between data and the Monte Carlo simulation for the low-z analysis. The plots compare (a) the polar angle of the muons,* θ_μ*, (b) the muon momentum,* p_μ*, (c)* $W_{\gamma p}$*, (d) z, (e) the radial track length of the muons, (f) the number of hits in the CMD from each muon, (g) the* $(E - p_z)$ *sum for the hadronic final state excluding the* J/ψ*, and (h) the* p_t *of the hadronic final state excluding the* J/ψ*.*

able and appear to be due to background. The background increases with $W_{\gamma p}$ (see section 7.3), hence the slight difference in shape. The medium-z θ_μ distribution shows an excess of events in data for $130^\circ \lesssim \theta_\mu \lesssim 150^\circ$. This region corresponds to the BBE wheel of the LAr calorimeter, a region which suffers from excessive 'punch-through' background and is therefore excluded in the low-z analysis. The subtraction of these background contributions has not been performed here, but is performed in chapters 7 and 8, where the cross-section is measured. The θ_μ distribution in the low-z analysis shows good agreement with the exception of one bin, $\theta_\mu \lesssim 25^\circ$, where there is a significant excess of data. Excluding this region reduced the number of events but changed the final results by less than the statistical error, and so it was retained

6.6 Systematic Errors

Muon Identification

The muon identification efficiency in data and Monte Carlo agree, apart from a few small deviations, once the LAr efficiency in Monte Carlo has been corrected. The correction function (equation 6.1) is determined from a fit to the ratio of the efficiencies in data and Monte Carlo. The resulting parameters have an error associated with them. Varying the parameters in the correction function by the amount allowed by their errors gives an estimate for one source of systematic error.

An additional source comes from the small differences in the efficiencies. Correcting the data using the efficiencies as measured using data, and varying these efficiencies by the statistical error on them, allows an estimate for this source of systematic error to be obtained. The two sources are added in quadrature and result in a systematic error of 7.9% (17%) in the medium (low)-z analysis.

Trigger Efficiency

The L1 trigger efficiencies measured in data and Monte Carlo broadly agree. However, there are some differences, The Monte Carlo efficiencies are used to correct the data, if the data efficiencies were used, slightly different results would be obtained. Additionally, there is a statistical error on the data efficiency. By correcting the data using the trigger efficiencies measured in data, and varying these efficiencies by the statistical error, an estimate of the systematic error due to the L1 trigger efficiencies can be obtained. This is 17% in the medium-z analysis, and 12% in the low-z analysis.

There is very good agreement between the L2NN efficiency measured in data and Monte Carlo. The statistical error on the data efficiency is used to estimate the systematic error, yielding 1.7%.

The L4 efficiency is measured using data. The Monte Carlo is corrected for the inefficiency on the verification of s19. Varying the correction factor by the statistical error on the efficiency gives an estimate for one source of the systematic error. The verification of s22 has a small inefficiency which is uncorrected. Correcting for this inefficiency, and varying the correction factor by the statistical error, gives an estimate for another source of systematic error. For the final source, a conservative uncertainty of 2% on the verification efficiency for s15 and s56 is assumed. Adding the contributions in quadrature gives a systematic error of 2.3(4.0)% in the medium(low)-z analysis.

Branching Ratio

The values quoted by the Particle Data Group are used for the J/ψ branching ratio [26]: $BR(J/\psi \rightarrow \mu^+\mu^-) = 5.88 \pm 0.10\%$. This leads to a systematic uncertainty of 1.7%.

Luminosity

The luminosity determination is described in section 4.2. The error on the luminosity found for the 1996 data taking period is 1.77% and in 1997 this was 1.5% [120], contributing a total error for the whole period of 1.6%.

Energy Scale of Calorimeters

The LAr and SPACAL calorimeters provide information that is used to reconstruct the kinematic variables of the event. The energy scale of these detectors is known to 4% and 7% respectively [15]. In addition, the energy scale of the trackers is known to 3%. These effects all contribute to an uncertainty in the energy and momentum measurements of all objects that are detected in the final state. By varying the measurements by the uncertainty on the energy scale, possible systematic effects can be studied and a systematic error of 2.9(3.5)% in the medium (low)-z analysis is estimated.

z-vertex distribution

As an estimate of the possible systematic error from residual differences between the z_{vtx} distributions in data and Monte Carlo, the results were calculated with and without the vertex re-weighting. The results differed by $\approx 1.5(1.0)\%$ in the medium(low)-z analysis, and this is used as an estimate of the possible systematic error.

Track and Vertex Finding

The efficiency for track reconstruction and vertex finding has been studied in several independent ways (see [80], [119] and [121], for example). The total efficiency is about 97% [121]. A conservative systematic error of 2% on the single track reconstruction efficiency is assumed [119], a 4% error in total.

$p^2_{t,J/\psi}$ re-weighting

The re-weighting of the $p^2_{t,J/\psi}$ distribution of the direct Monte Carlo leads to an improved agreement with the $p^2_{t,J/\psi}$ distribution in data (see figure 6.8). The parameters of the re-weighting function are determined from a fit and hence have errors associated with them. By varying the parameters by the errors, an estimate of any possible systematic error can be obtained. The results varied by $0 - 5.2\%$, depending on the bin, in the medium-z analysis, and $0.2 - 4.0\%$ in the low-z analysis. This is included as a systematic error.

Diffractive J/ψ and $\psi(2S)$ Background

The background due to J/ψ's produced in diffractive interactions and in the decay of diffractively produced $\psi(2S)$'s has been studied using Monte Carlo simulations of the events. The Monte Carlo program DIFFVM [89] (see section 2.6) was used to simulate the events and a small contamination is observed, in both the generated and reconstructed events, in the medium-z analysis for $z \gtrsim 0.65$. No contamination is observed in the low-z analysis. Including these events in the acceptance calculation, and varying the Monte Carlo normalisation by the experimental uncertainty on the diffractive cross-sections, gives an estimate for the systematic error from the diffractive background. In the low-z analysis, no systematic error is observed. In the medium-z analysis, a bin-dependent error of $3.7 - 5.8\%$ is observed on the cross-section as a function of $W_{\gamma p}$. For $d\sigma/dz$, a bin-dependent error of $0 - 14\%$ is observed. For $d\sigma/dp_{t,J/\psi}^2$, the lowest $p_{t,J/\psi}^2$ bin ($0 < p_{t,J/\psi}^2 < 1$ GeV^2) has a systematic error of 30%. This region is excluded from all other measurements in order to suppress the diffractive background. The other bins have a systematic error of $1 - 10\%$.

CJC Event Mixing

It was recently discovered that some of the information from the CJC tracking detectors was being mixed between events during part of the 1997 data taking [122]. The severity of the problem fluctuated and affected up to 8% of the CJC information. The affected data corresponds to an integrated luminosity of 6.50 pb^{-1}. Results were calculated excluding this data and some deviations of a few percent were found. This could be a statistical fluctuation, but as an estimate of any possible systematic error an overall cross-section for each analysis was calculated with and without the affected data. In the medium-z analysis, the differential cross section $d\sigma/dz$ was determined for the kinematic range $0.3 < z < 0.9$, $50 < W_{\gamma p} < 220$ GeV, and $p^2_{t,J/\psi} > 1$ GeV^2. The result was 44.7 ± 2.8 nb using the full data sample, and 42.3 ± 3.3 nb excluding the affected data. In the low-z analysis, the differential cross-section was determined for the kinematic range $0.07 < z < 0.45$, $120 < W_{\gamma p} < 250$ GeV, and $p^2_{t,J/\psi} > 1$ GeV^2. The result was 55.0 ± 8.0 nb using the full data sample, and 56.3 ± 9.6 nb excluding the affected data. In all cases, the errors are statistical only. The results differ by 5.4% (2.4%) in the medium(low)-z analysis. This is included as a systematic error.

Monte Carlo Mixing

In the low-z analysis, the Monte Carlo simulation of two different types of event need to be mixed in order to ensure the data is correctly simulated. The normalisation of each Monte Carlo is not correct. Therefore the normalisation of each of the Monte Carlo's is determined from the data. The data, however, has limited statistics which introduces a possible systematic error in obtaining the correct normalisation factors. By varying the normalisation factors by the amount allowed due to the statistical error on the data, the effect on the final acceptance can be studied. A bin dependent variation of $0 - 8\%$ is observed and assigned as a systematic error.

Source	Medium-z Analysis	Low-z Analysis
Muon Identification	7.9%	17%
L1 Trigger Efficiency	17%	12%
L2 Trigger Efficiency	1.7%	-
L4 Trigger Efficiency	2.3%	4.0%
Branching Ratio	1.7%	1.7%
Luminosity	1.6%	1.6%
Energy Scale	2.9%	3.5%
z-Vertex distribution	1.5%	1.0%
Track and Vertex Finding	4%	4%
Diffractive J/ψ and $\psi(2S)$ Background	0 – 14%	-
$p^2_{t,J/\psi}$ re-weighting	0 – 5.2%	0.2 – 4.0%
CJC event mixing	5.4%	2.4%
Monte Carlo mixing	-	0 – 8%
Sum	20 – 25%	22 – 24%

Table 6.2: *Summary of the systematic errors.*

Chapter 7

Results of the Medium-z analysis

This chapter presents the results of the analysis in the medium-z kinematic region ($0.3 < z < 0.9$). The measurement of the cross-section as a function of $W_{\gamma p}$, and the differential cross-sections $d\sigma/dz$ and $d\sigma/dp^2_{t,J/\psi}$ are presented and discussed. The method used for making the cross-section measurement is similar in each case. It will be described in detail for the measurement of the differential cross-section $d\sigma/dz$, and in outline for each subsequent measurement with any differences indicated. Finally, the results are compared with theoretical predictions. The results presented here are summarised in Appendix A.

7.1 Selected Data Sample

The data selection is described in chapter 4. The invariant mass spectrum of the muon pairs for all the events selected is shown, in the range $2.0 < m_{\mu\mu} < 4.0$ GeV, in

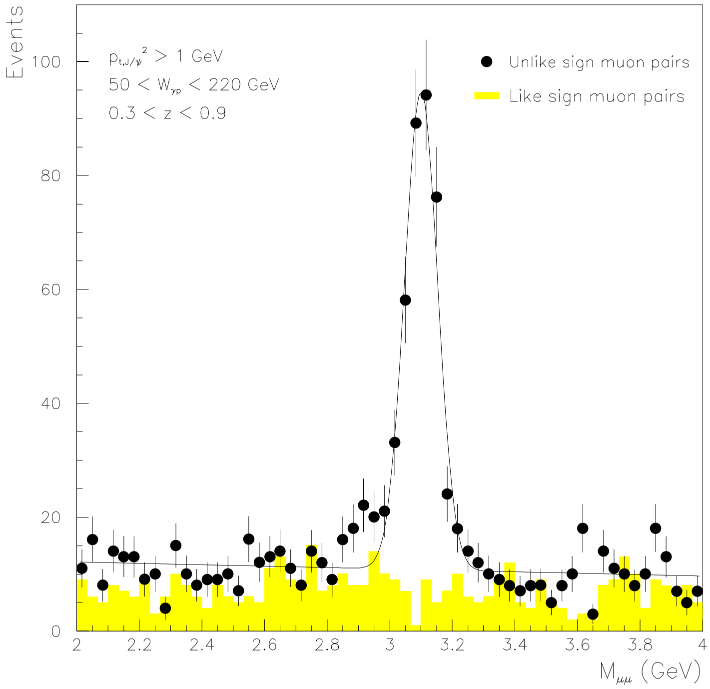

Figure 7.1: *Mass spectrum of the events selected for the medium-z analysis.*

figure 7.1. The figure also shows the spectrum for like-sign muons pairs selected using the same selection chain and subjected to the same analysis procedure. This is used as a consistency check for the background. The like-sign spectrum shows no peak at the J/ψ mass, thus showing that the J/ψ peak is not a an artefact of the analysis procedure. The shoulder on the mass peak at $m_{\mu\mu} \sim 2.9$ GeV has been investigated and is not due to detector effects. It is a statistical fluctuation upwards in this region.

The mass and width of the J/ψ can be extracted from the data by fitting a function which is the sum of a Gaussian and a first order polynomial to the data[1]. The function

---

[1] The first order polynomial is used to model the non-resonant background distribution. Other functions were also used (e.g. an exponential function) but this did not change the final results in any significant way.

is given by

$$f(x) = a + bx + \frac{c}{\sqrt{2\pi e}} \exp \frac{-(x-d)^2}{2e^2}, \tag{7.1}$$

and the resultant fit is also shown in figure 7.1. The measured mass and width of the J/ψ are then given by parameters d and e in equation 7.1. They are

$$\begin{aligned} m_{J/\psi} &= 3.100 \pm 0.004 \text{ GeV}, \\ \Gamma_{J/\psi} &= 52.7 \pm 4.0 \text{ MeV}. \end{aligned}$$

The mass is in agreement with the accepted value of 3.097 GeV [26], whilst the width is much greater than the accepted value of 87 ± 5 keV. The measured width, however, is dominated by the detector resolution. Using the same procedure, it is possible to extract the Monte Carlo expectation for the width. The value is $\Gamma_{J/\psi} = 55.0 \pm 0.7$ MeV. Hence the measured width in data is in agreement with the expectation from Monte Carlo simulations.

From the fit, the number of selected events can also be extracted (parameter c). There are 332.3 ± 21.8 events selected for the medium-z analysis.

7.2 Differential Cross-Section $d\sigma/dz$

The cross-section determination is performed in two stages. Firstly the electron-proton cross-section, $d\sigma_{ep \to J/\psi X}/dz$, is measured. Then this is converted into a photon-proton cross-section, $d\sigma_{\gamma p \to J/\psi X}/dz$. The differential e-p cross-section is calculated using

$$\frac{d\sigma_{ep}}{dz} = \frac{N_{events}(z)}{\varepsilon(z).\mathcal{L}.BR.\Delta z}, \tag{7.2}$$

where N_{events} is the number of events detected, ε is the acceptance, $\mathcal{L}$ is the integrated luminosity of the data recorded (see section 4.2), BR is the branching ratio for the decay channel used (in this analysis $BR = BR(J/\psi \to \mu^+\mu^-) = 5.88 \pm 0.10\%$ [26]) and Δz is the bin width. The acceptance is the total correction factor necessary to correct for the trigger efficiency, muon identification efficiency, reconstruction efficiency, detector acceptance and bin migrations. The following sections will describe the extraction of the number of events, the acceptance determination, the conversion of $d\sigma_{ep}/dz$ to $d\sigma_{\gamma p}/dz$, before presenting the results and discussing them with a comparison to theoretical predictions.

7.2.1 Extraction of the number of J/ψ events

The number of events in each bin is extracted using the following procedure. The first stage is to plot the invariant mass spectrum, $m_{\mu\mu}$, of the muon pairs from all J/ψ candidates, in the range $2 < m_{\mu\mu} < 4$ GeV, as shown in figure 7.1. The function $f(x)$, given by equation 7.1 is fitted to the distribution with all five parameters (a, b, c, d, and e) allowed to vary freely. The measured mass and width of the J/ψ are extracted (parameters d and e in equation 7.1), and these are then fixed for subsequent fits.

The invariant mass spectrum of the J/ψ candidates is then plotted separately for each bin, as shown in figure 7.2, which also indicates the bin limits. A clear signal can be observed in each bin, with the background increasing as z decreases. The function $f(x)$ is then fitted to each distribution with only three parameters allowed to vary freely (a, b, and c). The Gaussian normalisation (parameter c) gives the number of J/ψ events in that bin. The number of events as a function of z, extracted using this method, is shown in figure 7.3(a). The bin limits were partly chosen to achieve approximately the same number of events in each bin, as can be seen to be the case.

7.2.2 Correction of the Data

The acceptance is determined using the corrected Monte Carlo simulation. Chapter 6 described the various checks performed and correction factors applied in order to ensure that the simulation is correct. The acceptance is defined as

$$\varepsilon = \frac{n_{rec}(z_1 < z_{rec} < z_2, 50 < W_{rec} < 220, p_{t,rec}^2 > 1)}{n_{gen}(z_1 < z_{gen} < z_2, 50 < W_{gen} < 220, p_{t,gen}^2 > 1)}, \tag{7.3}$$

where z_1 and z_2 are the bin limits, and n_{rec} and n_{gen} are the corrected number of reconstructed and generated Monte Carlo events respectively. The acceptance can be factorised into four main stages: Geometrical acceptance (the effect of the cut on the polar angle, θ_μ, of the muon), Trigger Efficiency, Muon Identification and Final Selection Efficiency. This is illustrated by figure 7.4, where this factorisation is plotted as a function of $W_{\gamma p}$ and z. The largest efficiency loss is due to the trigger efficiency, with a significant $W_{\gamma p}$ dependence arising from the polar angle cut on the muons. There

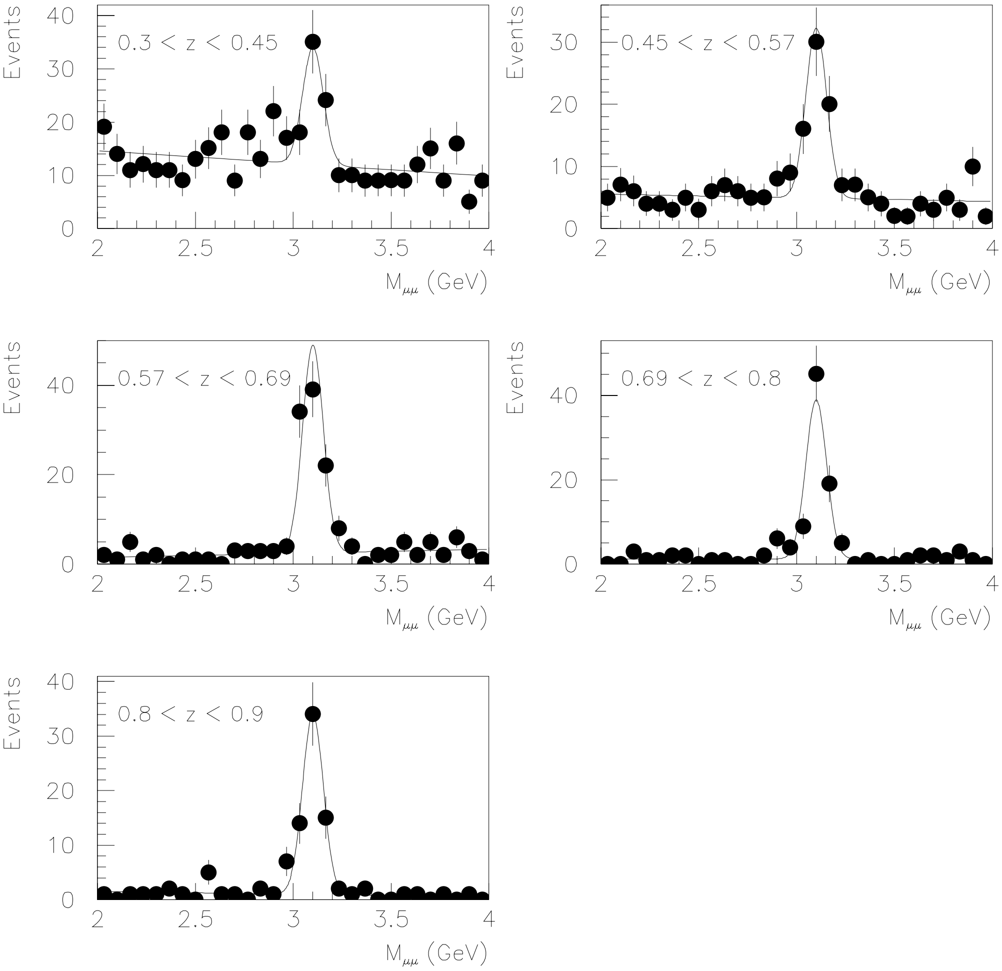

Figure 7.2: *Invariant mass spectrum of the selected events in bins of z.*

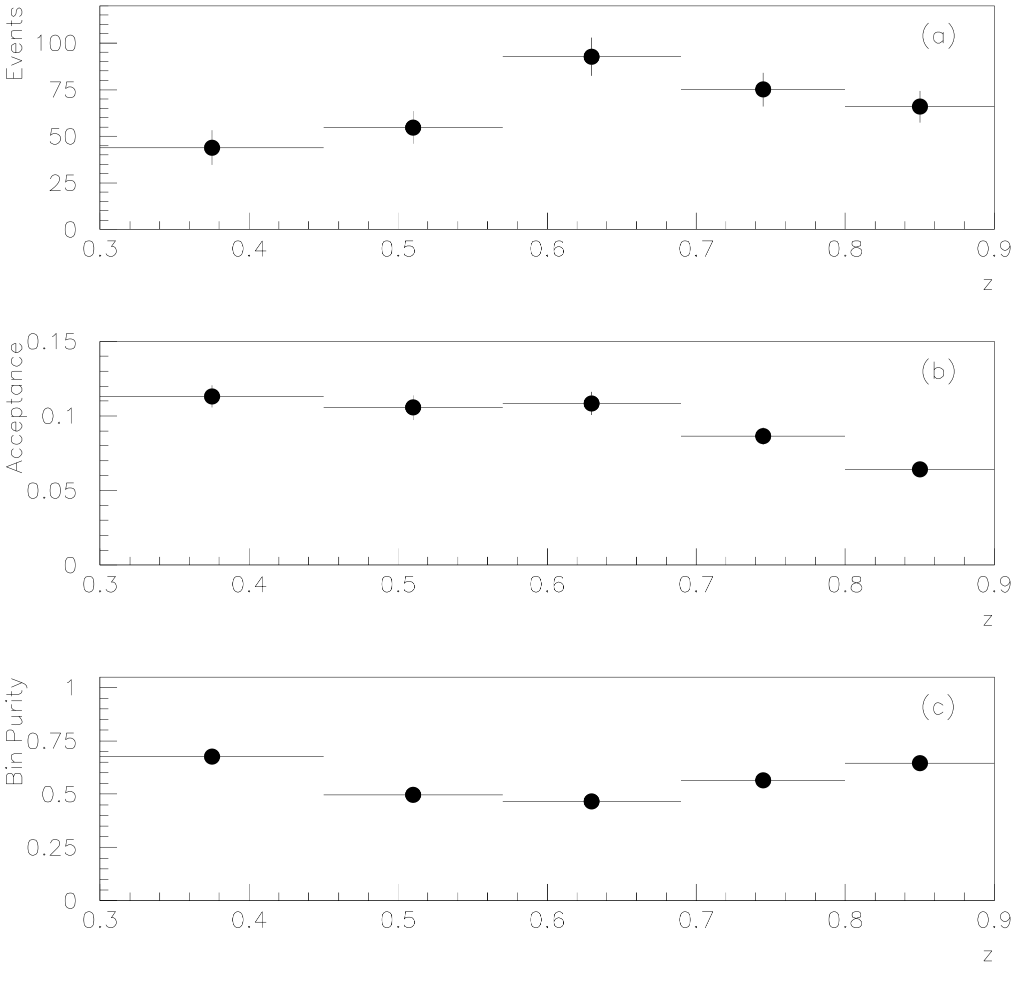

Figure 7.3: *The (a) number of events selected, (b) acceptance and (c) bin purity for each bin in z.*

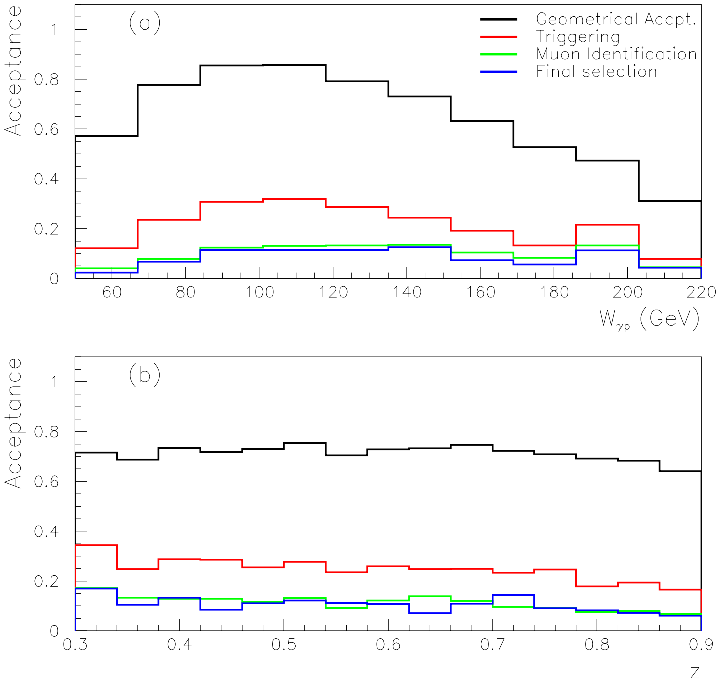

Figure 7.4: *Factorisation of the acceptance as a function of (a) $W_{\gamma p}$ and (b) z. The plot shows the cumulative acceptance after adding each indicated selection criteria in turn.*

is also a significant inefficiency due to muon identification.

The total acceptance is shown in figure 7.3(b) for each z bin. The acceptance is approximately constant but starts to fall as z increases. This is because as z increases the energy available for the production of particles in addition to the J/ψ decreases. Therefore fewer will be produced and they will have a lower momentum. Several stages of the selection require the presence of additional particles. For example, the L1 sub-triggers s19 and s22 require at least three track candidates. The efficiency for a track to be reconstructed increases with momentum and this contributes to the fall in acceptance as z increases.

In order to check for any significant bin migrations, the bin purity is shown in figure 7.3(c). The bin purity is measured using the Monte Carlo simulation, and is defined as

$$\text{Bin Purity} = \frac{N_{stay}}{N_{rec}}, \tag{7.4}$$

where N_{rec} is the number of events reconstructed in a bin and N_{stay} is the number of events that were both generated and reconstructed in the bin. The bin purity is $\gtrsim 50\%$ for each bin.

The final correction factor is the bin centre correction. This is applied in order to correct for the affect of the bin centre not being the average in the bin. In this case, the average z (or $W_{\gamma p}$, $p^2_{t,j/\psi}$) of the data events in each bin is used as the plotting value for the measurements.

7.2.3 Conversion to γ-p Cross-Section

The conversion from electron-proton to photon-proton cross-section is a relatively trivial step. The flux of quasi-real photons from an electron is well understood and is therefore not of much interest. By converting, a well understood part of the measurement is removed, leaving the measurement of the more interesting photon-proton interaction. Additionally, it allows comparison with results from fixed target γ-p experiments, for example.

The γ-p cross-section can be calculated from the e-p cross-section using [123]

$$\sigma_{ep} = \int_{y_{min}}^{y_{max}} dy \int_{Q^2_{min}}^{Q^2_{max}} dQ^2 \mathcal{F}_{\gamma/e}(y, Q^2)\sigma_{\gamma p}, \tag{7.5}$$

where $\mathcal{F}_{\gamma/e}$ is the flux of photons emitted by the electron, and, in this analysis, the Q^2 range is:

$$\begin{aligned} Q^2_{max} &= 1 \text{ GeV}^2 \\ Q^2_{min} &= \frac{m_e^2 y^2}{1-y} \end{aligned}$$

where m_e is the mass of the electron. Q^2_{max} is given by the minimum acceptance of the SPACAL, and Q^2_{min} is the minimum kinematically allowed.

In photoproduction, the photons are almost real and so are predominantly transversely polarised. In this case, the Weizsäcker-Williams approximation [124] can be used. The photon flux is given by

$$\mathcal{F}_{\gamma/e}(y, Q^2) = \frac{\alpha}{2\pi}\frac{1}{yQ^2}(1 + (1-y)^2 - \frac{2m_e^2 y^2}{Q^2}), \tag{7.6}$$

where α is the electromagnetic coupling constant [125].

The photoproduction cross-section only has a weak dependence on Q^2 and y (for $Q^2 < 1$ GeV^2). Hence the γ-p cross-section is, to a good approximation, given by

$$\sigma_{\gamma p} = \frac{\sigma_{ep}}{\Phi_{\gamma/e}}, \tag{7.7}$$

where $\Phi_{\gamma/e}$ is the photon flux factor, given by

$$\Phi_{\gamma/e} = \int_{y_{min}}^{y_{max}} dy \int_{Q^2_{min}}^{Q^2_{max}} dQ^2 \mathcal{F}_{\gamma/e}(y, Q^2). \tag{7.8}$$

The photon flux can then be calculated by a numerical integration.

7.2.4 Results and Model Comparison

Figure 7.5 shows the results for the differential cross-section $d\sigma/dz$. The inner error bars are statistical errors only and the outer error bars are statistical and systematic errors added in quadrature. Also shown on the plot are the results of fitting two different functions to the results. They are an exponential function ($d\sigma/dz \propto e^{b.z}$) and power law function ($d\sigma/dz \propto z^{\delta}$). Both parameterisations give a good description of the data. As the largest systematic errors are all correlated, only the statistical error was taken into account for the fit. The results of the fits were $b = 2.73 \pm 0.39$ for the exponential function, and $\delta = 1.64 \pm 0.25$ for the power law.

The results are compared with other results and the predictions from two different models in figure 7.6. The results from this analysis are in good agreement with the preliminary results from H1 [126] and ZEUS [127]. The dashed line is the prediction from a leading order Colour Octet (LO CO) model calculation [78]. The CO model matrix elements used in the calculation were determined using constraints obtained from the Tevatron data, fixed target experiments and B decays. The calculation used a charm quark mass of $m_c = 1.5$ GeV, a factorisation scale of $2m_c$, the GRV LO

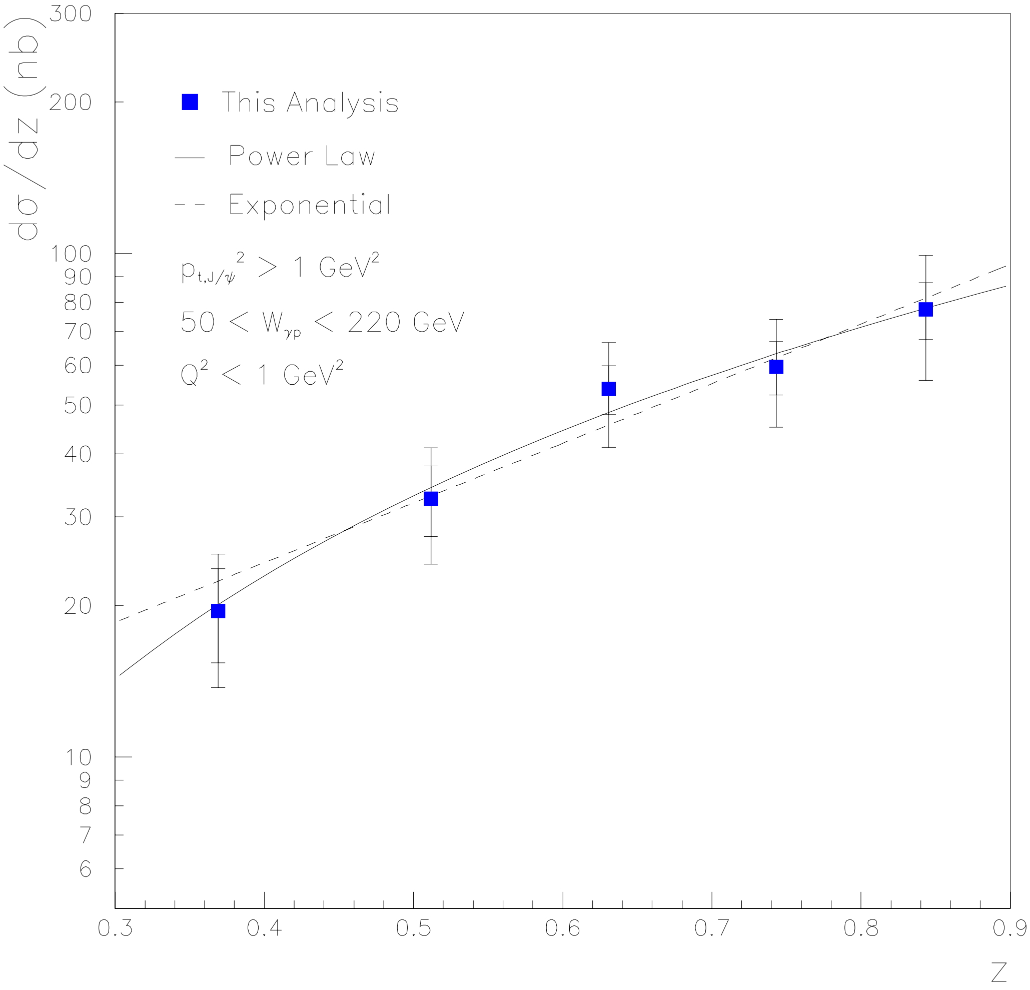

Figure 7.5: *The differential cross-section $d\sigma/dz$, measured in the kinematic range* $p^2_{t,J/\psi} > 1$ GeV^2, $50 < W_{\gamma p} < 220$ GeV *and* $Q^2 < 1$ GeV^2*. The line is a fit of* $d\sigma/dz \propto z^{\delta}$*, yielding* $\delta = 1.64 \pm 0.25$*. The dashed line is a fit of* $d\sigma/dz \propto e^{b.z}$*, yielding* $b = 2.73 \pm 0.39$*.*

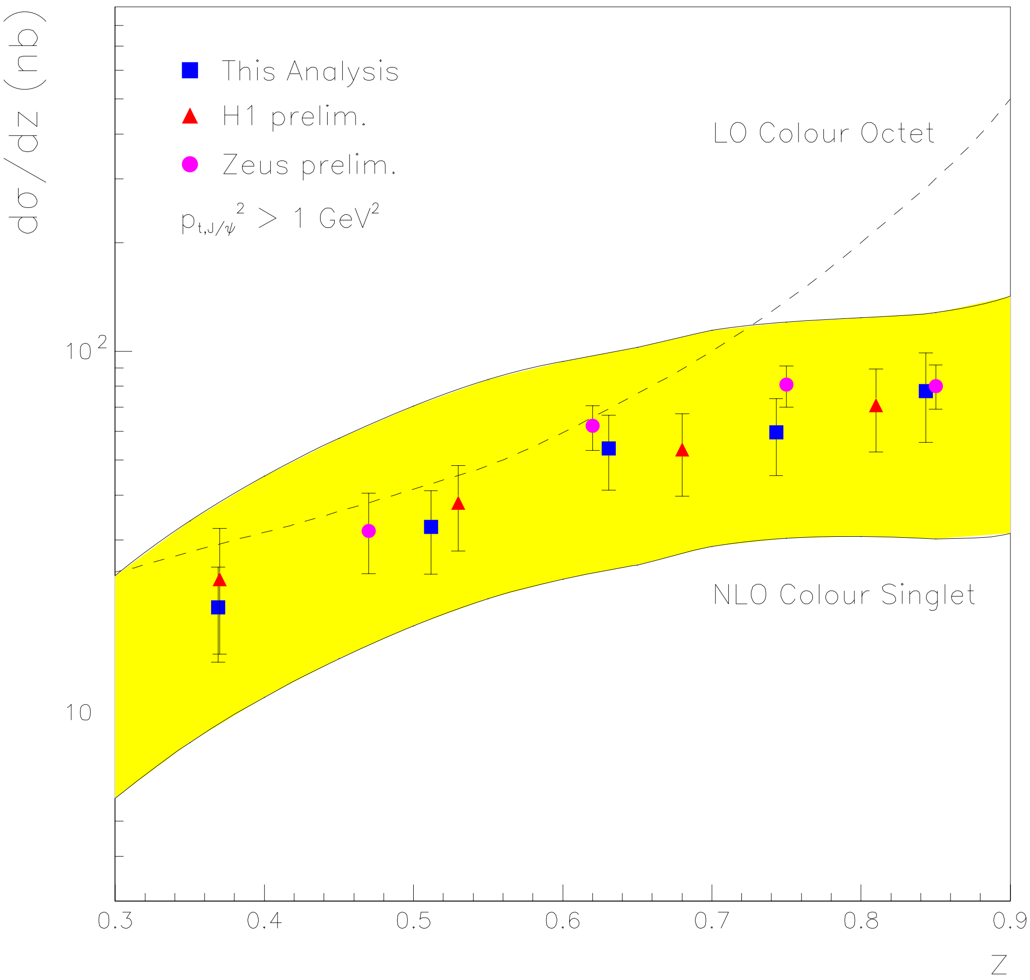

Figure 7.6: *The differential cross-section* $d\sigma/dz$ *from this analysis and preliminary results from H1 [126] and ZEUS [127]. The dashed line shows the prediction from a LO Colour Octet model calculation [78], whilst the shaded area represents the prediction and uncertainty from a NLO Colour Singlet model calculation [41, 128, 129].*

parton density functions [67, 81] and is for $W_{\gamma p} = 100$ GeV (in data the average $W_{\gamma p}$ is ≈ 126 GeV). The shaded band shows the uncertainty on the prediction from a next-to-leading order Colour Singlet (NLO CS) model calculation [41, 128], which has recently been updated [129]. The calculation is for the direct photon interaction only, used a factorisation scale of $\sqrt{2}m_c$ and is for $W_{\gamma p} = 100$ GeV, with the upper and lower bounds obtained by varying the input parameters. The upper bound was the result of using $m_c = 1.3$ GeV, $\alpha_s(M_Z) = 0.1225$ and the MRST99 (set 5) PDF's [74] as input parameters. The lower bound was obtained by using $m_c = 1.5$ GeV, $\alpha_s(M_Z) = 0.1175$ and the MRST99 (set 1) PDF's [74] as input parameters. The choices of α_s and PDF are correlated as the PDF's are extracted for specific values of α_s, whilst the range $1.3 < m_c < 1.5$ GeV represents the typical range of uncertainty in m_c.

The results clearly favour the NLO CS model calculation over the LO CO model calculation. The LO CO model does not describe the shape of the $d\sigma/dz$ distribution, in contrast to the NLO CS model. However, there is a large uncertainty (a factor of ~ 3) in the normalisation of the CS model at NLO.

7.3 Cross-Section as a function of $W_{\gamma p}$

The measurement method is largely the same as described above, therefore only an outline will be given. Figure 7.7 shows the invariant mass spectrum of the selected events for each bin in $W_{\gamma p}$, with the bin limits also indicated. A clear signal can be observed in each bin, with the background increasing with $W_{\gamma p}$. The number of events

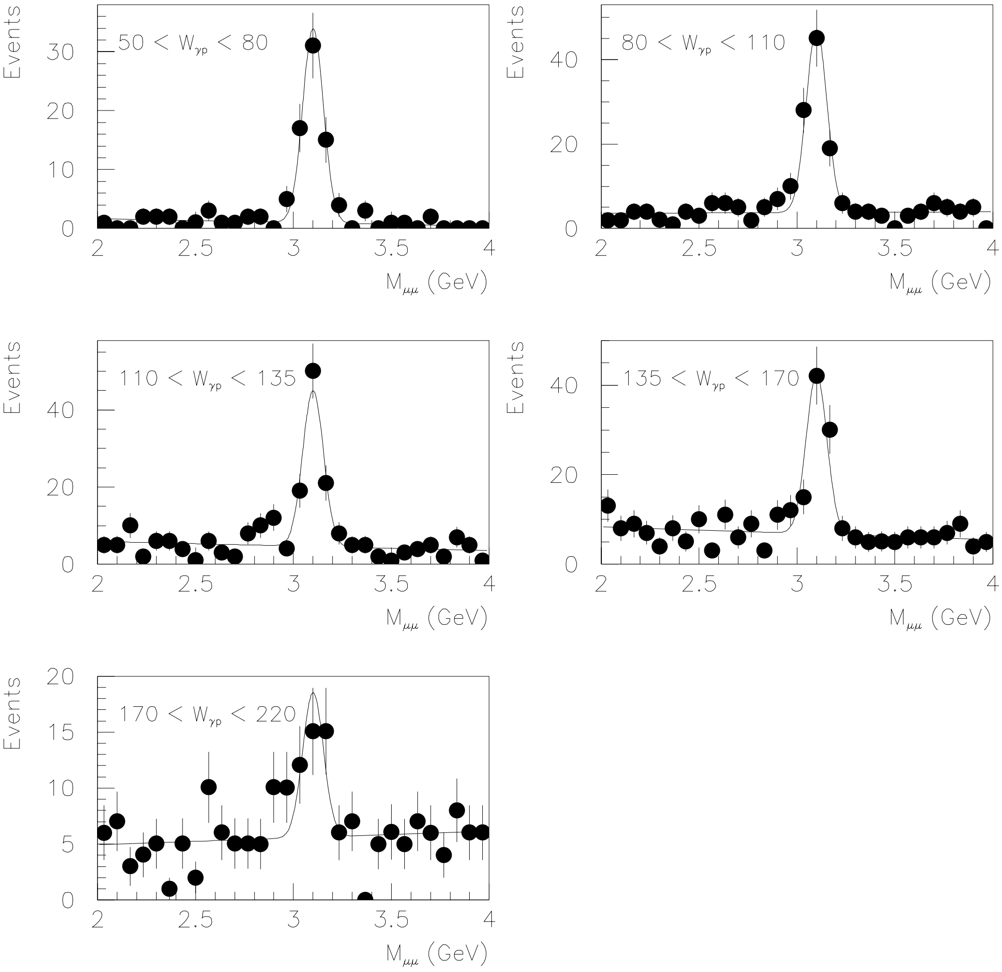

Figure 7.7: *Invariant mass spectrum of the selected events in bins of* $W_{\gamma p}$.

as a function of $W_{\gamma p}$ is shown in figure 7.8(a). The acceptance is defined as:

$$\varepsilon = \frac{n_{rec}(W_1 < W_{rec} < W_2, p^2_{t,rec} > 1, 0.3 < z_{rec} < 0.9)}{n_{gen}(W_1 < W_{gen} < W_2, p^2_{t,gen} > 1, 0.3 < z_{gen} < 0.9)}, \tag{7.9}$$

where W_1 and W_2 are the bin limits. The acceptance is shown in figure 7.8(b) for each $W_{\gamma p}$ bin. The acceptance is $\gtrsim 5\%$ for each bin, with a large variation arising from the geometrical acceptance. The Bin Purity, shown in figure 7.8(c), is $\gtrsim 75\%$ for each bin.

From the above information, the cross-section σ_{ep} can be calculated using

$$\sigma_{ep} = \frac{N_{events}}{\varepsilon.\mathcal{L}.BR}. \tag{7.10}$$

The conversion to $\sigma_{\gamma p}$ is performed using the procedure described in section 7.2.3. The bin centre correction is performed as described in section 7.2.2.

7.3.1 Results and Model Comparison

The results for the measurement of the cross-section as a function of $W_{\gamma p}$ are shown in figure 7.9. The inner error bars are statistical errors only and the outer error bars are statistical and systematic errors added in quadrature. The cross-section is measured in the kinematic range $0.3 < z < 0.9$, $p^2_{t,J/\psi} > 1$ GeV^2, and $Q^2 < 1$ GeV^2. The gluon content of the proton rises rapidly as x decreases [12], and, as can be seen from equations 2.4 and 2.6, this implies that the gluon content increases as $W_{\gamma p}$ increases. The interaction under study here is boson-gluon fusion and so the cross-section is

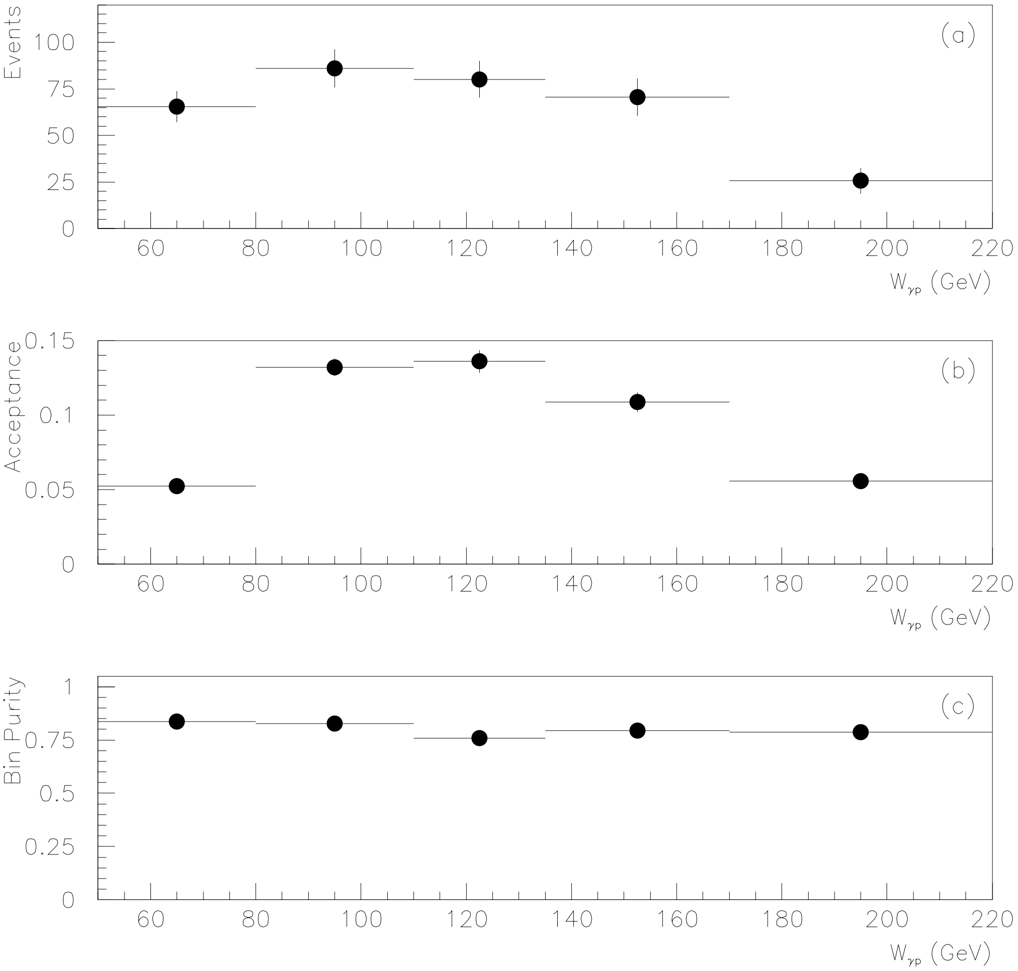

Figure 7.8: *The (a) number of events selected, (b) acceptance and (c) bin purity for each bin in* $W_{\gamma p}$.

expected to rise with $W_{\gamma p}$, as observed. The plot also shows the results of fitting two different functions to the data. As before, they are an exponential function ($\sigma \propto e^{b.W_{\gamma p}}$) and a power law ($\sigma \propto W_{\gamma p}^{\delta}$) and only the statistical errors have been taken into account in the fit. Both functions give a good description of the data. The results are $b = (4.55 \pm 1.72) \times 10^{-3}$ for the exponential function, and $\delta = 0.54 \pm 0.21$ for the power law. Including preliminary results from H1 [126] and ZEUS [127] in the power law fit yields $\delta = 0.55 \pm 0.15$.

The power law result is of particular interest as this function is used to parameterise the diffractive cross-section as a function of $W_{\gamma p}$. The H1 collaboration recently obtained $\delta = 0.83 \pm 0.07$ [33] for diffractive J/ψ photoproduction. The diffractive events are viewed as occurring via Pomeron exchange, and the partonic content of the Pomeron has been shown to be dominated by gluons [16]. The simplest model of the Pomeron is one in which it contains two gluons. Hence diffractive J/ψ production will couple more strongly to the gluon content of the proton. The result here shows that the inelastic cross-section does not rise as rapidly with $W_{\gamma p}$ as the diffractive cross-section, supporting this picture.

Figure 7.10 compares the results with preliminary results from H1 and ZEUS, as well as the predictions from a NLO CS model calculation [41, 128] which has recently been updated [129] and was described in section 7.2.4. The results are in good agreement with previous results, and this analysis has extended the $W_{\gamma p}$ range covered. The shaded band corresponds to the uncertainty on the NLO CS model calculation, with the upper and lower bands obtained by varying the input parameters as described in

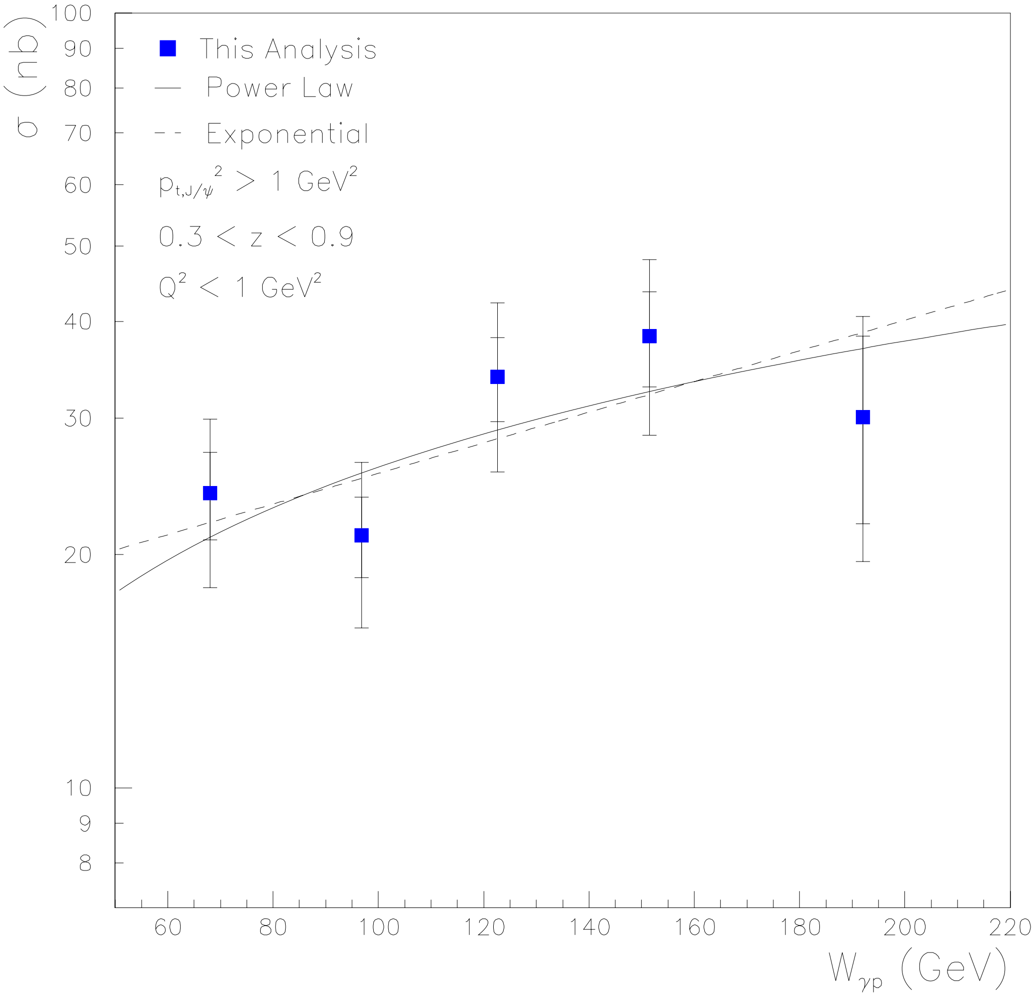

Figure 7.9: *The total photon-proton cross-section* $\sigma(\gamma p \rightarrow J/\psi X)$ *as a function of* $W_{\gamma p}$*, measured in the kinematic range* $p_{t,J/\psi}^2 > 1$ GeV^2, $0.3 < z < 0.9$ *and* $Q^2 < 1$ GeV^2*. Two functions are fitted to the data:* $\sigma \propto W_{\gamma p}^{\delta}$ *and* $\sigma \propto e^{b.W_{\gamma p}}$*. The fits yield* $\delta = 0.54 \pm 0.21$ *and* $b = (4.55 \pm 1.72) \times 10^{-3}$.

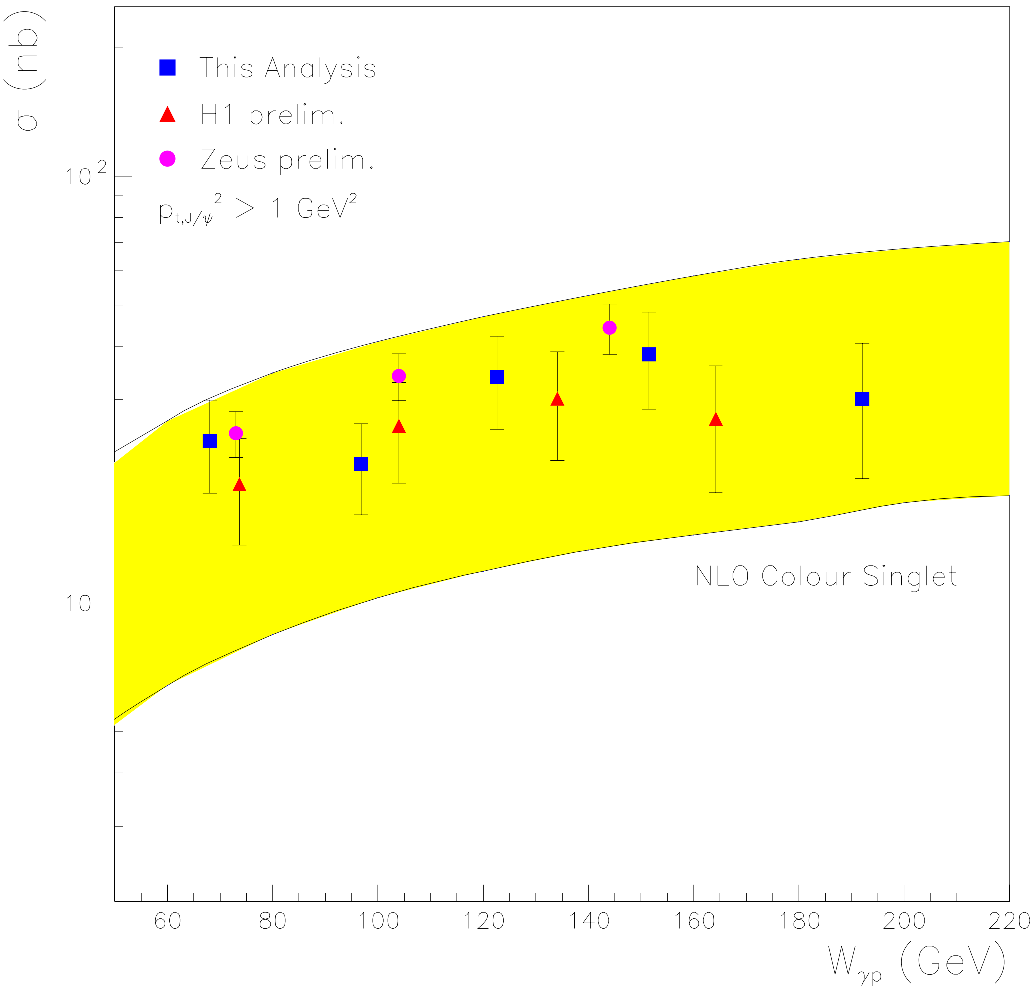

Figure 7.10: *The total photon-proton cross-section* $\sigma(\gamma p \to J/\psi X)$ *versus* $W_{\gamma p}$ *from this analysis and preliminary results from H1 [126] and ZEUS [127]. The shaded area represents the results and uncertainty arising from a NLO Colour Singlet model calculation [129].*

section 7.2.4. The Colour Singlet model describes the shape of the data well, with a large uncertainty over the normalisation.

7.4 Differential Cross-Section $d\sigma/dp^2_{t,J/\psi}$

The procedure for measuring the differential cross-section is as described previously. The invariant mass spectrum of the selected events is shown in figure 7.11 for each bin in $p^2_{t,J/\psi}$. The bin limits are also indicated on each plot. A J/ψ signal can be observed in each bin, with both the number of events and the number of background events decreasing as $p^2_{t,J/\psi}$ increases. This is reflected in the choice of bin limits, with the bin size increasing with $p^2_{t,J/\psi}$ (with the exception of the first bin). The number of events in each bin is shown in figure 7.12(a).

The acceptance is defined as

$$\varepsilon = \frac{n_{rec}(p^2_{t,1} < p^2_{t,rec} < p^2_{t,2}, 50 < W_{rec} < 220, 0.3 < z_{rec} < 0.9)}{n_{gen}(p^2_{t,1} < p^2_{t,gen} < p^2_{t,2}, 50 < W_{gen} < 220, 0.3 < z_{gen} < 0.9)}, \tag{7.11}$$

where $p^2_{t,1}$ and $p^2_{t,2}$ are the bin limits. The acceptance is shown in figure 7.12(b) for each $p^2_{t,J/\psi}$ bin. The acceptance can clearly be seen to rise with $p^2_{t,J/\psi}$. Figure 7.12(c) shows the bin purity, which is greater than 90% in all bins. The differential cross-section $d\sigma_{ep}/dp^2_{t,J/\psi}$ can then be calculated using equation 7.2, replacing z with $p^2_{t,J/\psi}$. The conversion to $d\sigma_{\gamma p}/dp^2_{t,J/\psi}$, and the bin centre corrections were both performed using the methods already described. The bin centre corrections are more significant in this case due to the steeply falling $p^2_{t,J/\psi}$ distribution.

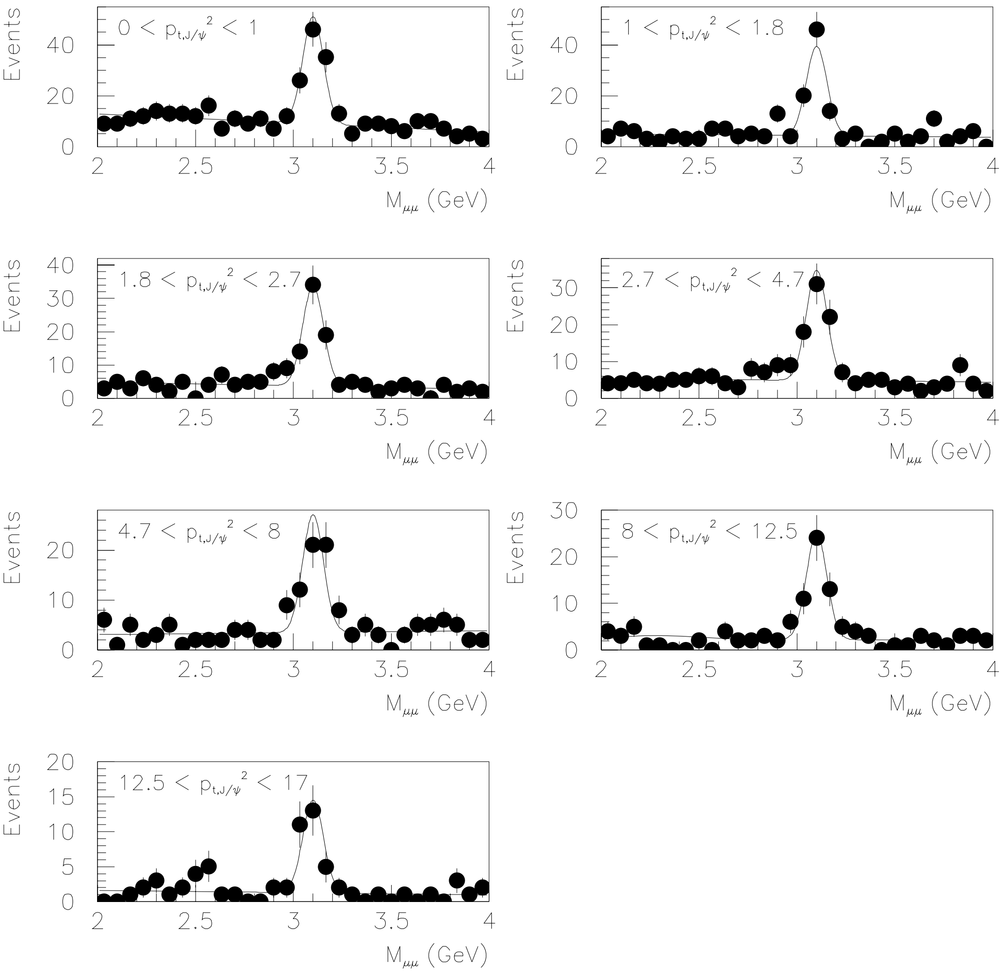

Figure 7.11: *Invariant mass spectrum of the selected events in bins of* $p^2_{t,J\psi}$.

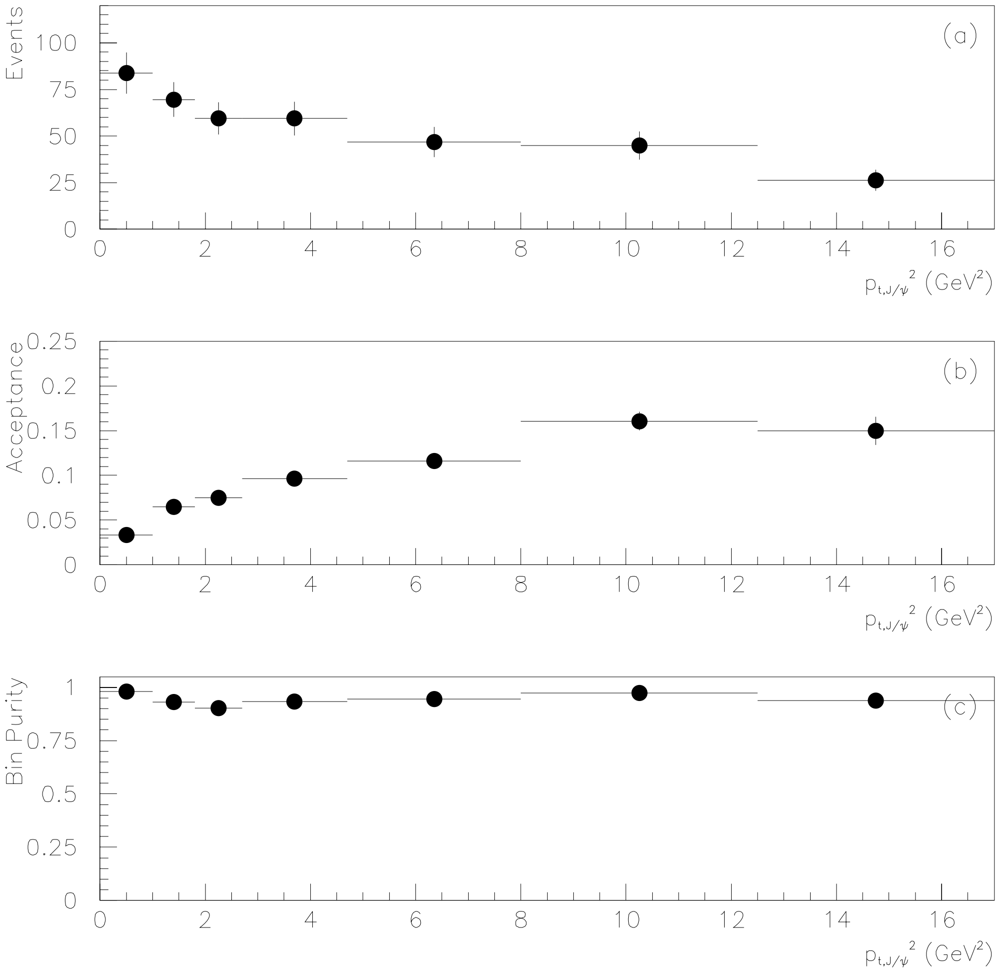

Figure 7.12: *The (a) number of events selected, (b) acceptance and (c) bin purity for each bin in* $p^2_{t,J\psi}$.

7.4.1 Results and Model Comparison

The differential cross-section $d\sigma/dp^2_{t,J/\psi}$, as measured in this analysis, is shown in figure 7.13. The inner error bars are statistical errors only and the outer error bars are statistical and systematic errors added in quadrature. The measurement has been made in the kinematic range $0.3 < z < 0.9$, $50 < W_{\gamma p} < 220$ GeV and $Q^2 < 1$ GeV^2. As with the previous results, two functions have been fitted to the data: a power law ($d\sigma/dp^2_{t,J/\psi} \propto (p^2_{t,J/\psi})^\delta$) and an exponential function ($d\sigma/dp^2_{t,J/\psi} \propto e^{b.p^2_{t,J/\psi}}$). An exponential function is often used to parameterise the diffractive differential cross-section at low $p^2_{t,J/\psi}$ (see [33], for example). As can be seen, the exponential function gives a reasonable description at low $p^2_{t,J/\psi}$, but fails at high $p^2_{t,J/\psi}$ where the distribution begins to flatten. Whilst neither fit is particularly good, the power law gives a better description of the data than the exponential function. This is unsurprising as, in the Colour Singlet model, the cross-section is expected to have a power law dependence, with the leading order contribution expected to have a $1/p^8_{t,J/\psi}$ dependence, and the next-to-leading order contribution a $1/p^6_{t,J/\psi}$ dependence [129]. The results of the fits are $\delta = -1.20 \pm 0.04$ and $b = -0.46 \pm 0.05$.

Figure 7.14 compares the results of this analysis with preliminary results from H1 [126] and ZEUS [127], and the figure illustrates the consistency between all the experimental results. The results are also compared with the predictions of the Colour Singlet model at leading order and next-to-leading order [41, 128], which have recently been updated [129]. The NLO Colour Singlet model calculation was described in section 7.2.4 and the shaded area represents the uncertainty in the predictions, determined using the

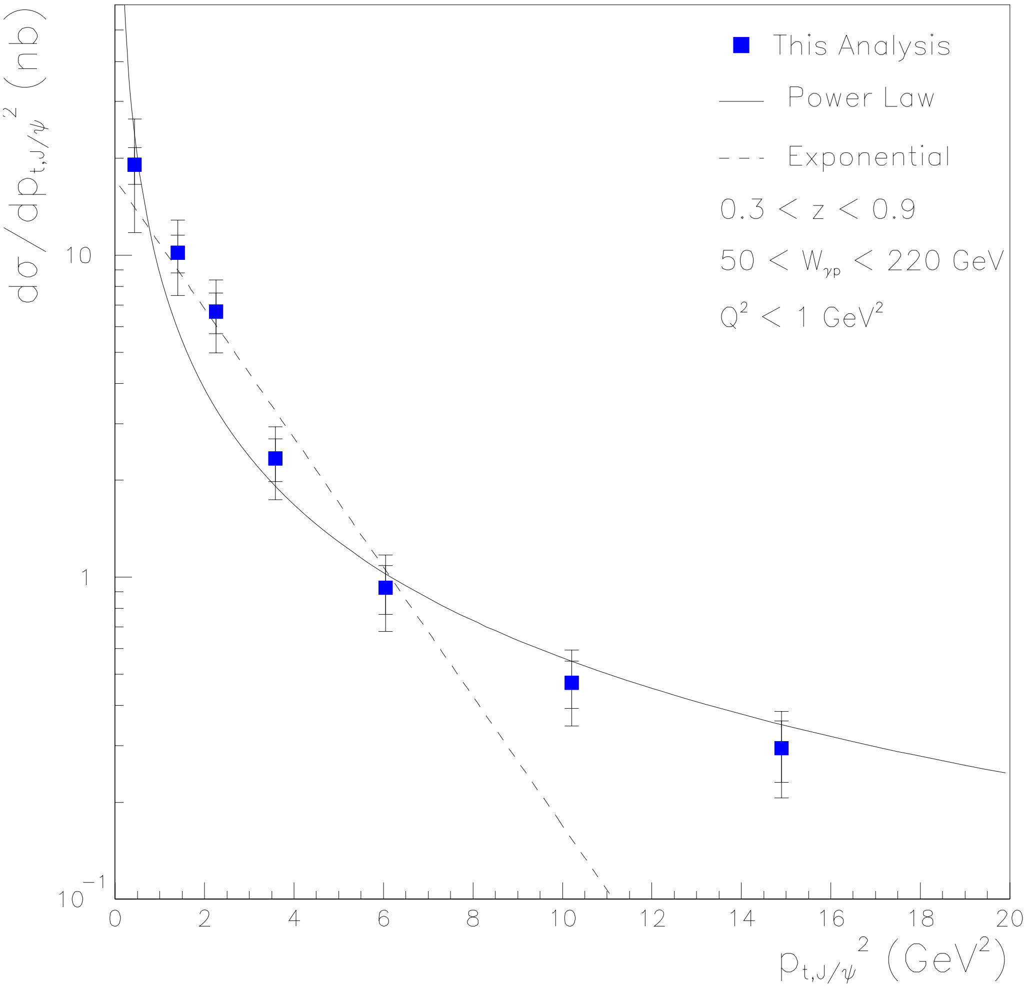

Figure 7.13: *Differential cross-section* $d\sigma/dp^2_{t,J/\psi}$ *measured in the kinematic range* $0.3 < z < 0.9$, $50 < W_{\gamma p} < 220$ GeV *and* $Q^2 < 1$ GeV^2. *The functions* $d\sigma/dp^2_{t,J/\psi} \propto (p^2_{t,J/\psi})^\delta$ *and* $d\sigma/dp^2_{t,J/\psi} \propto e^{b.p^2_{t,J/\psi}}$ *are fitted to the data, yielding* $\delta = -1.20 \pm 0.04$ *and* $b = -0.46 \pm 0.05$.

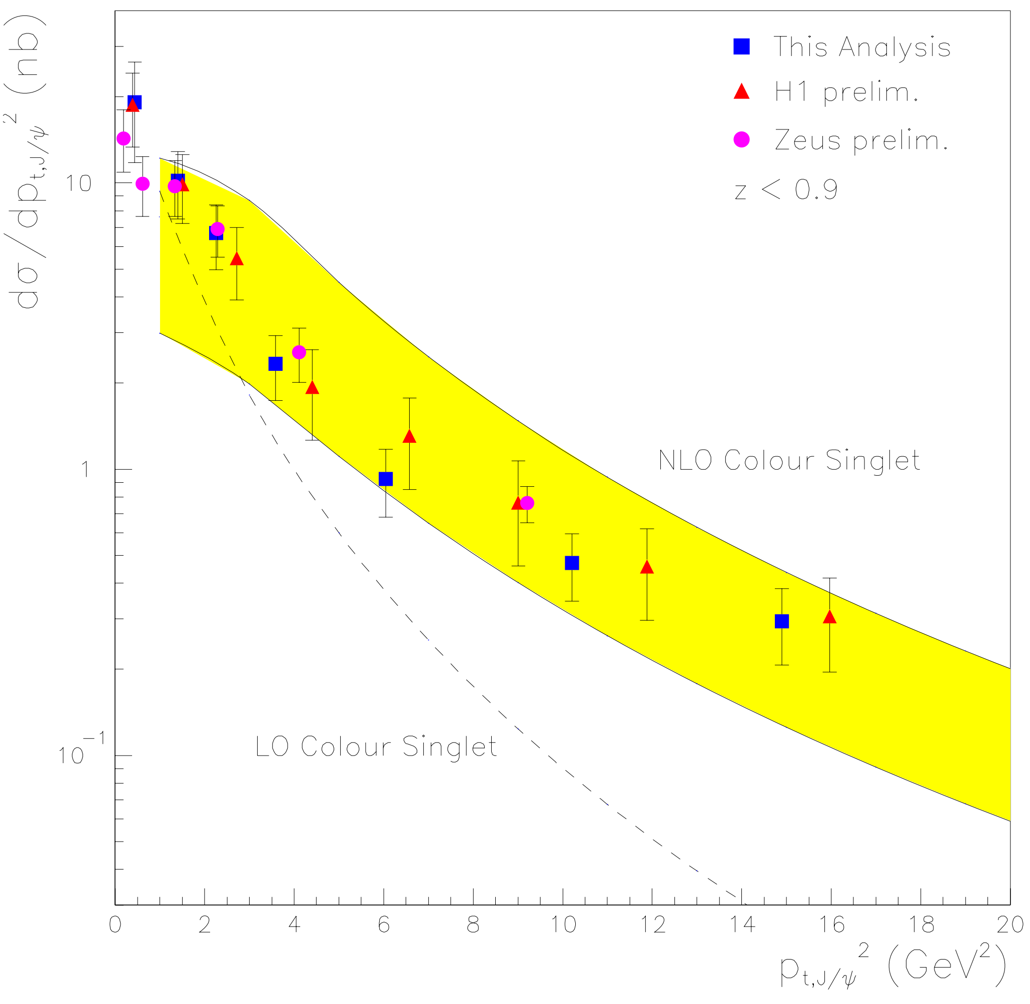

Figure 7.14: *The differential cross-section* $d\sigma/dp^2_{t,J/\psi}$ *from this analysis and preliminary results from H1 [126] and ZEUS [127]. The dashed line is a LO Colour Singlet model calculation, whilst the shaded area shows the results and uncertainty resulting from a NLO Colour Singlet model calculation.*

method previously described. The LO calculation was performed using a factorisation scale of $\sqrt{2}m_c$, a charm quark mass of $m_c = 1.3$ GeV, a leading order $\alpha_s(M_Z)$ of 0.13 and the MRST98LO(set 5) PDF's. The LO CS calculation fails to describe the $p^2_{t,J/\psi}$ distribution correctly, predicting a more steeply falling distribution than is observed. The NLO calculation does describe the shape of the distribution correctly, with the same factor of ~ 3 uncertainty in the normalisation as was observed in the z and $W_{\gamma p}$ distributions.

7.5 Summary

The inelastic photoproduction of J/ψ mesons has been studied in the medium-z kinematic region. The differential cross-sections $d\sigma/dz$ and $d\sigma/dp^2_{t,J/\psi}$, and the cross-section as a function of $W_{\gamma p}$, have all been measured. Good agreement with other preliminary results has been found and the $W_{\gamma p}$ range covered has been extended. The shape of the results are well described by the Colour Singlet model at next-to-leading order, whereas both the Colour Singlet and Colour Octet models fail at leading order to describe the shapes. There is, however, a large uncertainty in the normalisation of the Colour Singlet model at next-to-leading order due to the uncertainty over the choice of input parameters for the calculation. The results here provide no evidence for the Colour Octet contributions which were necessary to explain the Tevatron results. However, there is no next-to-leading order Colour Octet model calculation available. It would be interesting to see if this could describe the data in a similar way to how the Colour Singlet does at next-to-leading order but not at leading order.

Chapter 8

Results of the Low-z Analysis

This chapter presents the results of the analysis in the low-z kinematic region. The primary purpose of this analysis is to extend the kinematic region over which measurements have been made into the low-z region. There are currently no published results in this region, only one set of preliminary results are available [1]. This analysis covers $0.07 < z < 0.45$, over a $W_{\gamma p}$ region of $120 < W_{\gamma p} < 250$ GeV, for $p^2_{t.j/\psi} > 1$ GeV^2 and $Q^2 < 1$ GeV^2 (see section 5.3). Measurements of the cross-section as a function of $W_{\gamma p}$, and the differential cross-sections $d\sigma/dz$ and $d\sigma/dp^2_{t,J/\psi}$ are presented and discussed. The results presented here are summarised in Appendix B.

8.1 Selected Data Sample

The data selection has already been described in chapter 4. Figure 8.1 shows the invariant mass spectrum of the unlike sign muon pairs for all the events selected in the

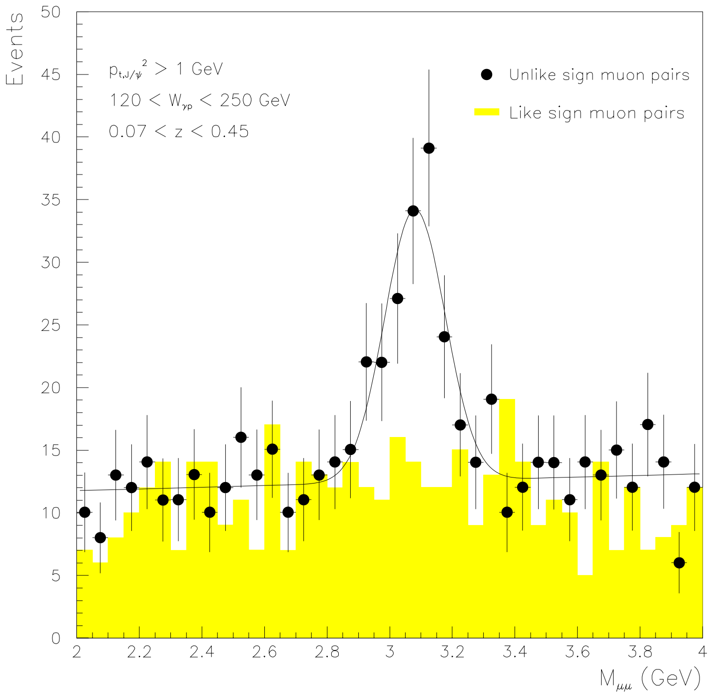

Figure 8.1: *Mass spectrum of the events selected for the low-z analysis.*

range $2.0 < m_{\mu\mu} < 4.0$ GeV. Also shown is the spectrum for the like-sign muon pairs in the same range, from which it can be seen that the signal in the unlike-sign pairs is genuine and not an artefact of the analysis procedure. The measured mass and width of the J/ψ, determined using the method described in section 7.1, is:

$$\begin{aligned} m_{J/\psi} &= 3.081 \pm 0.017 \text{ GeV}, \\ \Gamma_{J/\psi} &= 96.8 \pm 18.8 \text{ MeV}. \end{aligned}$$

The mass is consistent with the accepted value. The width, however, is much greater than both the accepted value, and the value measured in the medium-z analysis. Additionally, the value determined from Monte Carlo simulation is $\Gamma_{J/\psi} = 47.5 \pm 1.3$ MeV.

The measured value is much greater in data due to the much higher background rate than in the medium-z analysis. There 105.3 ± 17.8 events selected for the low-z analysis.

8.2 Correction of the data

As with the medium-z analysis, the data is corrected using Monte Carlo simulation to determine the acceptance, with as many efficiencies as possible checked independently with data (see chapter 6 for these checks). In this analysis, the situation is complicated by the need to mix Monte Carlo simulations of two different types of events: direct and resolved photoproduction. This was not necessary in the medium-z analysis because the direct events dominate (see figure 2.12). The normalisation of each Monte Carlo simulation is not correct as a full next-to-leading order calculation is not included. Therefore, a more practical approach is used in order to obtain the correct mixture of events.

The direct Monte Carlo is normalised to the data in a region where the direct events are expected to be dominant and the resolved events negligible. The region chosen is given by $0.5 < z < 0.9$, $50 < W_{\gamma p} < 220$ GeV, and $p^2_{t.j/\psi} > 1$ GeV^2 (changing the lower z cut to 0.4 or 0.6 makes negligible difference). This normalisation factor is then applied to the direct Monte Carlo in the low-z region. The resolved Monte Carlo's normalisation factor is determined by normalising the Monte Carlo to the difference between the data and the normalised direct Monte Carlo in the region studied in the low-z analysis. The mixture of normalised Monte Carlo's is then used to determine the acceptance needed to correct the data.

8.3 Differential Cross-Section $d\sigma/dz$

The procedure used for measuring the differential cross-section $d\sigma/dz$ is the same as that described in section 7.2. Figure 8.2 shows the invariant mass spectrum of the selected events in three bins of z. The unlike-sign spectrum is also shown for each bin and a signal can be observed in each bin. The bin limits have also been indicated on the figure. They were chosen so that the first two bins were of similar width and contain a similar number of events. The final bin covers an identical z range to the lowest bin in z from the medium-z analysis, allowing cross-checks between the two analyses. Figure 8.3 shows (a) the number of events, (b) the acceptance, and (c) the bin purity for each bin. The bin purity is higher ($> 60\%$) than that for the medium-z analysis. The acceptance of the third bin ($0.3 < z < 0.45$) is lower than was found in the medium-z analysis. This is because of the different $W_{\gamma p}$ range covered, which was optimised in this case for the region $0.07 < z < 0.3$. From this information, the differential cross-section $d\sigma/dz$ can be calculated using equation 7.2.

8.3.1 Results and Model Comparison

Figure 8.4 shows the number of events as a function of z in data and Monte Carlo. The figure also shows the resolved contribution to the number of Monte Carlo events. This illustrates the need to include a resolved component in the simulation and calculations

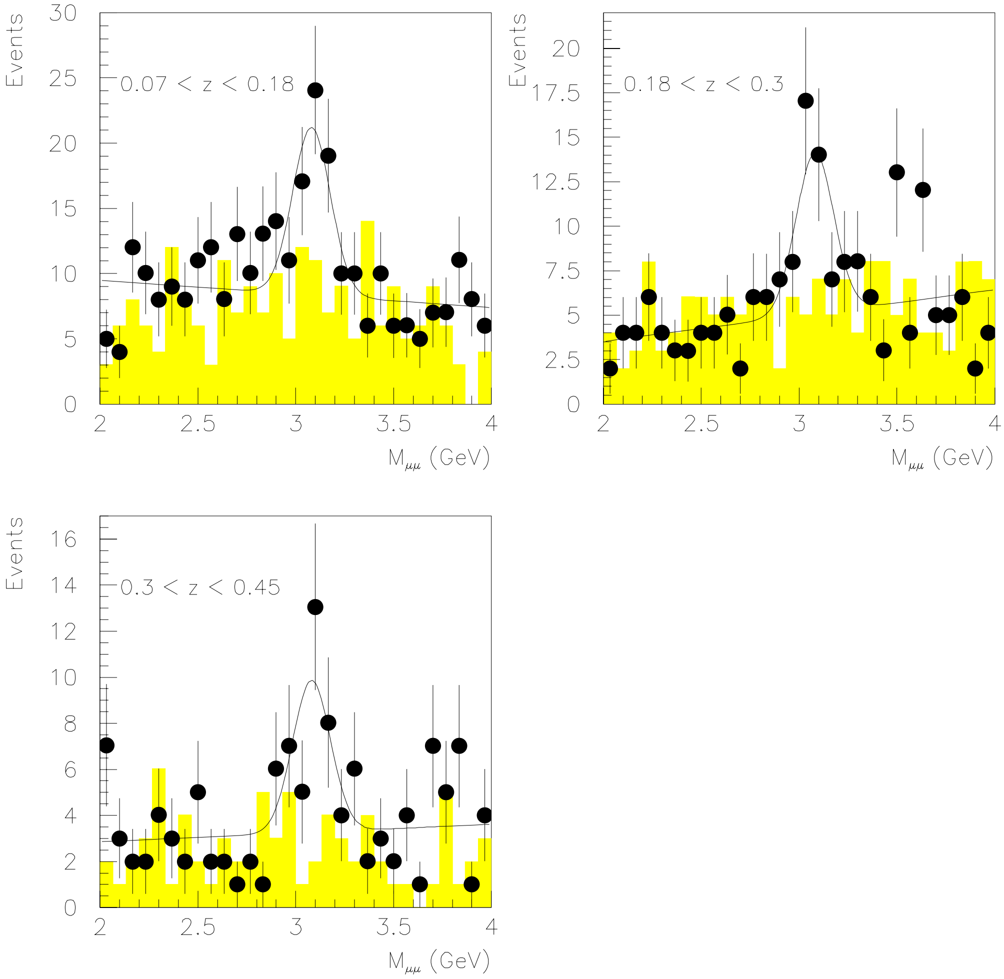

Figure 8.2: *Invariant mass spectrum of the events selected for the low-z analysis in three bins of z.*

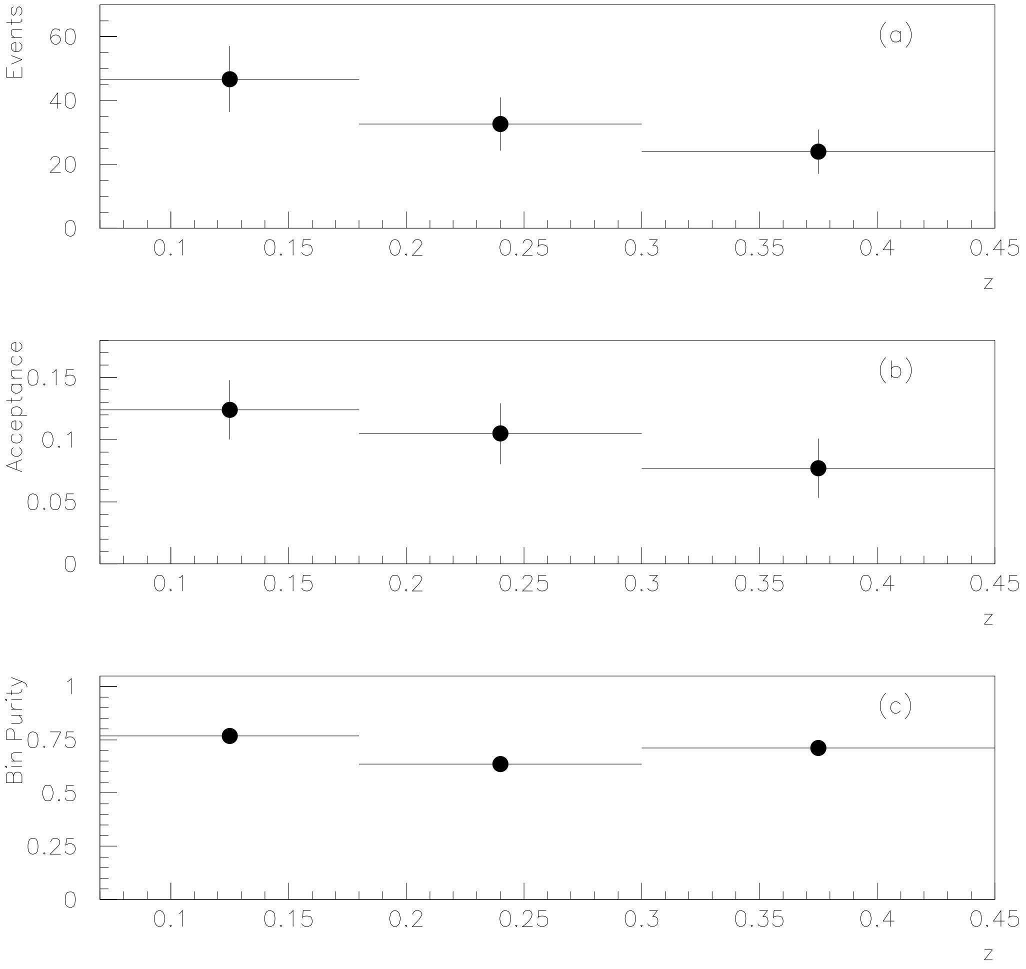

Figure 8.3: *The (a) number of events selected, (b) acceptance and (c) bin purity for each z bin for the low-z analysis.*

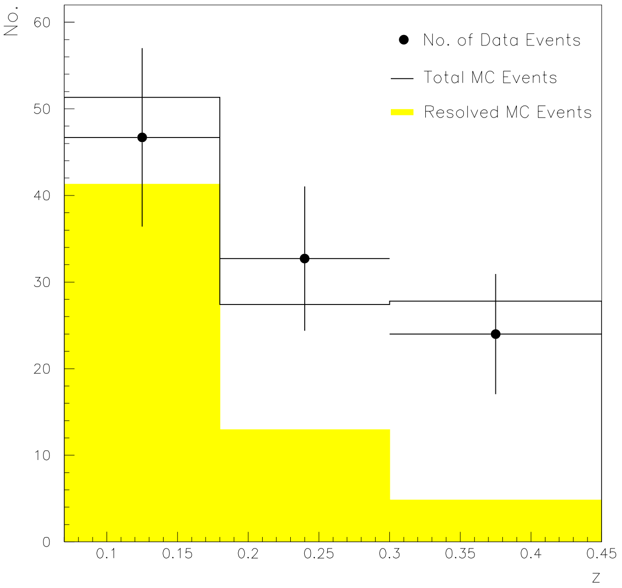

Figure 8.4: *The number of events as a function of z in data and Monte Carlo. The shaded area represents the contribution from resolved photon interactions.*

as it becomes increasingly important as z decreases.

The differential cross-section $d\sigma/dz$, measured in the kinematic range $120 < W_{\gamma p} < 250$ GeV, $p^2_{t,J/\psi} > 1$ GeV^2 and $Q^2 < 1$ GeV^2, is shown in figure 8.5. The results are compared with preliminary results from H1 [1] and the prediction of the Colour Octet model [42, 78] which has recently been updated [129]. The dashed line represents the contribution from the colour singlet channel, whilst the solid line is the contribution from the colour octet channels. The calculation has been performed at leading-order, using matrix element extracted from the Tevatron data, and includes both direct and resolved photoproduction. The input parameters were the GRV(LO) proton and photon PDF's [67, 81], $m_c = 1.5$ GeV, and a factorisation scale of $2m_c$. The calculation is for a $W_{\gamma p}$ of 170 GeV, which is close to the average $W_{\gamma p}$ of the events in data of

169.3 GeV. The shaded area shows the total differential cross-section from both channels, and the uncertainty due to the uncertainty in the CO matrix elements. The uncertainty was estimated by comparing the different values for the matrix elements obtained from the Tevatron data [129]. The matrix elements were varied in the ranges:

$$\begin{aligned} \langle \mathcal{O}_{\underline{8}}^{J/\psi}({}^3\mathrm{S}_1)\rangle &= (0.3\ -\ 2.0)\times 10^{-2}\ \mathrm{GeV}^3 \quad \text{and} \\ M_{3.5}^{J/\psi} &= (1.0\ -\ 10.0)\times 10^{-2}\ \mathrm{GeV}^3. \end{aligned}$$

The results of this analysis are in good agreement with the preliminary results and are consistent with the prediction of the Colour Octet model at leading order. The uncertainty on the prediction is large (up to a factor of 10) due to the uncertainty on the extracted matrix elements. Hence these results could be used to further constrain the matrix elements and reduce the uncertainty on the predictions of the Colour Octet model.

The results are compared with the predictions of the Colour Singlet model [42, 78], which has recently been updated [129], in figure 8.6. The predictions include both direct and resolved photoproduction, and are the result of a leading-order calculation using the same input parameters as the Colour Octet model calculation described above. The shaded area represents the uncertainty on the prediction, estimated by varying the charm quark mass (m_c) between 1.3 and 1.5 GeV and the factorisation scale (μ_R) between m_c and $2m_c$[1]. This results in an uncertainty of a factor of ~ 5 in

---

[1] There will also be an additional uncertainty due to the uncertainty on α_s. However this cannot be studied in a rigorous way at present because the photon PDF's have only been extracted for fixed α_s [129].

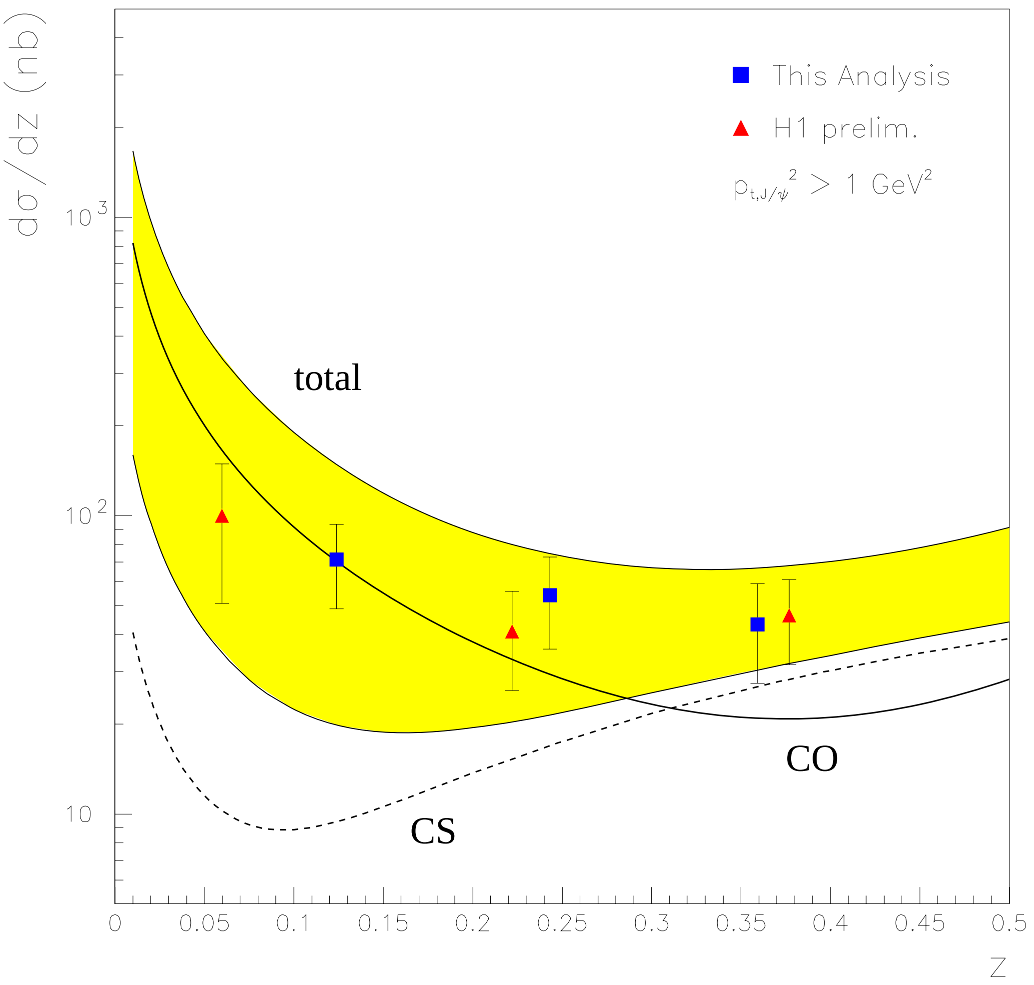

Figure 8.5: *The differential cross-section $d\sigma/dz$ measured in the kinematic range* $120 < W_{\gamma p} < 250$ GeV, $p^2_{t,J/\psi} > 1$ GeV^2 *and* $Q^2 < 1$ GeV^2. *The results are compared with preliminary results from H1 and theoretical predictions from the Colour Octet model. The dashed line is the contribution from the colour singlet channel, and the solid line is the contribution from colour octet channels. The shaded area shows the total prediction and the uncertainty due to the uncertainty in the colour octet matrix elements.*

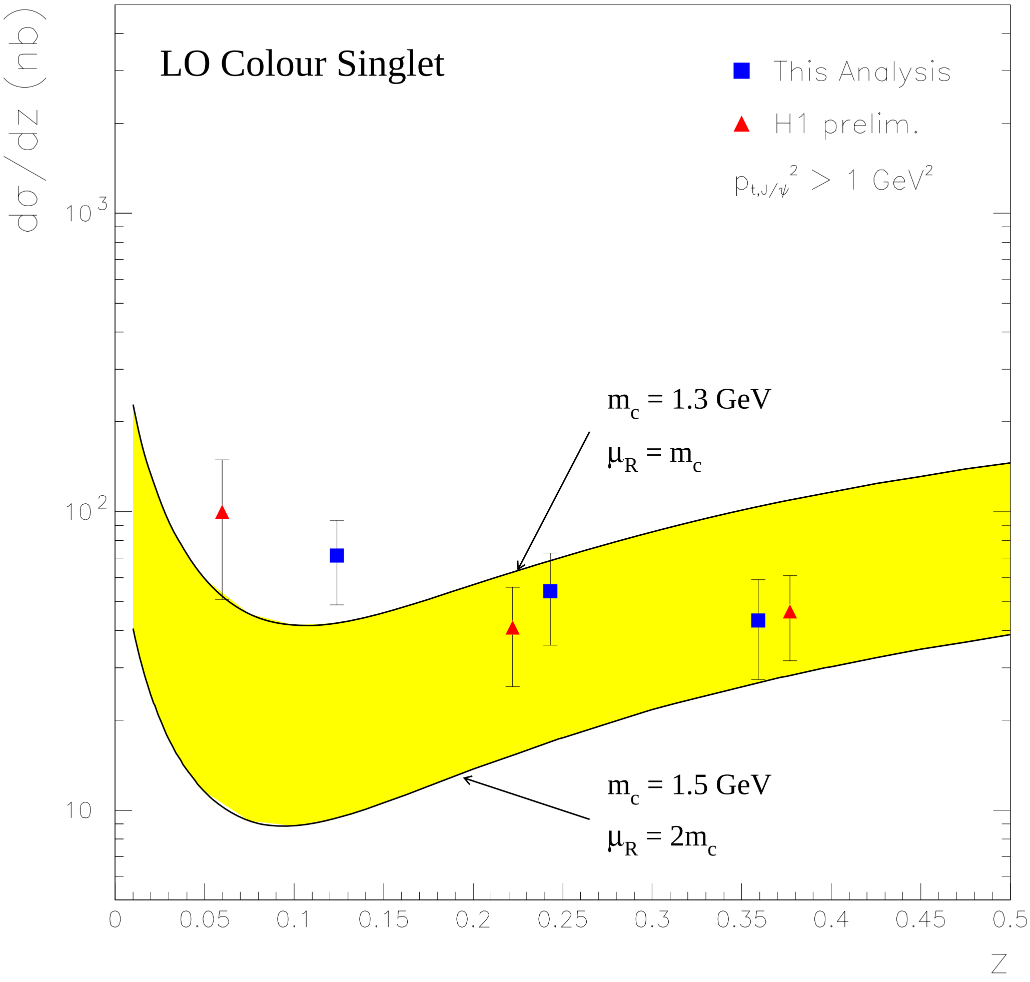

Figure 8.6: *Comparison of the differential cross-section $d\sigma/dz$ from this analysis and H1 preliminary results with the predictions of the Colour Singlet model. The predictions are from a leading-order calculation and the shaded area represents the uncertainty on the prediction, estimated by varying the charm quark mass, m_c, and the factorisation scale, μ_R.*

the normalisation. The results are almost consistent with the Colour Singlet model. In the medium-z analysis, the results were consistent with a next-to-leading order Colour Singlet model calculation (see Chapter 7). Unfortunately, no NLO CS model calculation exists for this region. It would be interesting to see if this agreed with the data.

8.3.2 Comparison with the medium-z analysis

The results here can be compared with the results of the medium-z analysis. This is done in figure 8.7, where the two analyses are also compared with the predictions of the Colour Octet model [42, 78] which has recently been updated [129]. The predictions are from a LO calculation and include both resolved and direct contributions. The input parameters were as described in section 8.3.1 and the shaded band represents the uncertainty on the predictions due to the uncertainty in the colour octet matrix elements. The solid line indicates the total prediction for $d\sigma/dz$ and the various dashed lines the contribution from each channel. Strictly, the low-z results are not comparable as the calculations is for $W_{\gamma p} = 100$ GeV, however qualitative conclusions can be drawn.

From the figure, it is clear that more data is needed in the low-z region before definitive conclusions can be drawn. The shape of the medium-z analysis is described by the CS-direct contribution. However, the contribution from the CS channels is significantly below the low-z points. This figure illustrates the significant theoretical and experimental uncertainties, showing the need for more work to clarify the picture.

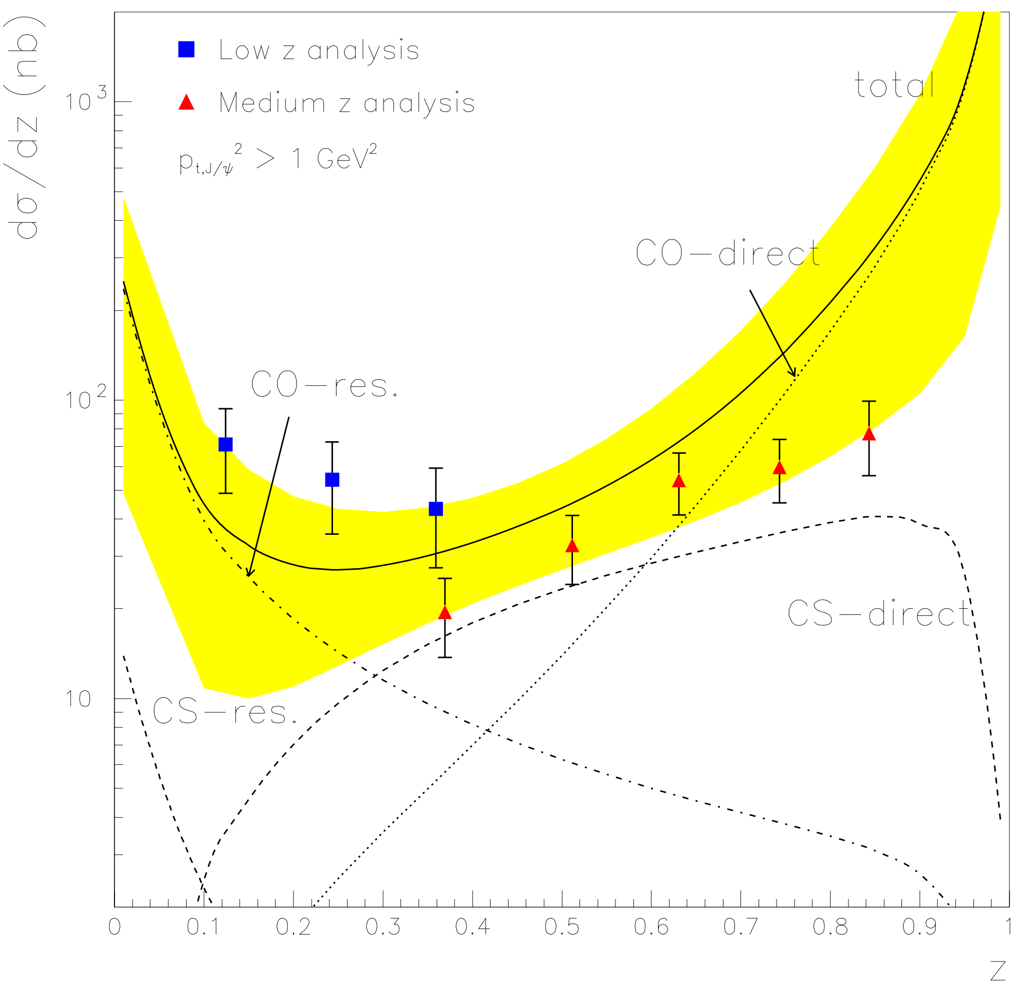

Figure 8.7: *Comparison of $d\sigma/dz$ from the medium and low-z analyses and the predictions of the Colour Octet model. The total (solid line) and the contributions from the individual channels (dashed lines) are shown. The shaded band indicates the uncertainty on the prediction due to the matrix elements.*

There is one bin which overlaps between the two analyses: $0.3 < z < 0.45$. There is a disagreement between the results of the two analyses. From the medium-z analysis, $d\sigma/dz = 19.51 \pm 5.76$ for a mean z of $\langle z \rangle = 0.37$. From the low-z analysis, $d\sigma/dz = 43.27 \pm 15.86$ for $\langle z \rangle = 0.36$. The two analyses cover overlapping but different $W_{\gamma p}$ ranges, with the low-z result expected to be higher due to it covering the higher $W_{\gamma p}$ range. Indeed, using the result of the power law fit to the medium-z data, and the mean $W_{\gamma p}$ from each analysis, an estimate of the expected change in $d\sigma/dz$ with the change in $W_{\gamma p}$ range can be obtained. This suggests that the medium-z result should rise by around 17%, which brings the results within one standard deviation of each other. Additionally, the method for correcting the data is different. In the medium-z analysis, the direct Monte Carlo is used, whilst a mixture of direct and resolved Monte Carlo's are used in the low-z analysis. Although the bin is dominated by direct events, there are resolved events present (see figure 8.4). This could account for the remaining difference. Indeed, studies of the acceptance suggest that correcting the low-z points using direct Monte Carlo events only, would cause the result to fall by around 1%.

8.4 Cross-Section as a function of $W_{\gamma p}$

The measurement of the total photon-proton cross-section, $\sigma(\gamma p \to J/\psi X)$, as a function of $W_{\gamma p}$ is performed using the method described previously. The measurement is made in the kinematic range $0.07 < z < 0.45$, $p^2_{t,J/\psi} > 1$ GeV^2 and $Q^2 < 1$ GeV^2. The invariant mass spectrum of the selected events is shown in figure 8.8. Two bins have been chosen, with a very clear signal visible in the first bin and a smaller signal in the

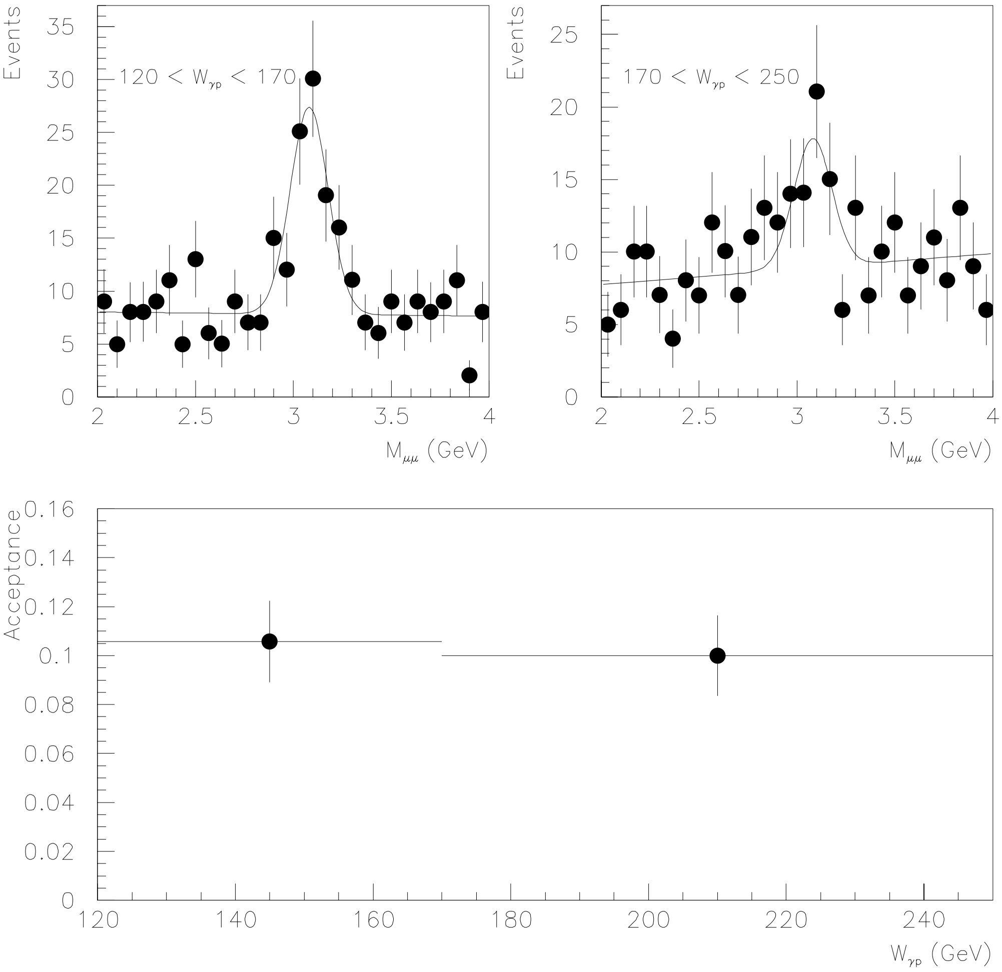

Figure 8.8: *Invariant mass spectrum of the events selected for the low-z analysis in two bins of $W_{\gamma p}$, and the acceptance for each bin.*

second. Figure 8.8 also shows the acceptance, which is $\sim 10\%$, for each bin.

The results are shown in figure 8.9, where they are compared with (a) preliminary results from H1 [1] and (b) the results from the medium-z analysis. The results agree well with the preliminary results. They are of a similar order of magnitude to the results from the medium-z analysis, being lower due to the different z range covered.

8.5 Differential Cross-Section $d\sigma/dp^2_{t,J/\psi}$

The differential cross-section $d\sigma/dp^2_{t,J/\psi}$ is measured using the procedure already described. The invariant mass spectrum of the selected events is shown in figure 8.10 for four bins in $p^2_{t,J/\psi}$, with the bin limits also indicated. A signal can be seen in each bin, although it is not as clear as was the case for the z bins. Four bins are chosen so that the shape of the $p^2_{t,J/\psi}$ distribution can be investigated. The bin limits have been chosen so that there are a similar number of events in each bin. This is illustrated by figure 8.11(a), which shows the number of events in each bin. Figure 8.11(b) shows the acceptance in each bin, which rises with $p^2_{t,J/\psi}$ as was observed in the medium-z analysis. Figure 8.11(c) shows the bin purity, which is $> 75\%$ for all bins.

The results for $d\sigma/dp^2_{t,J/\psi}$, measured in the kinematic range $120 < W_{\gamma p} < 250$ GeV, $0.07 < z < 0.45$ and $Q^2 < 1$ GeV^2, are shown in figure 8.12. The inner error bars are statistical and the outer error bars are statistical and systematic errors added in quadrature. The results are compared with the preliminary results from H1 [1] and good agreement is found. Two functions have been fitted to the results of this analysis

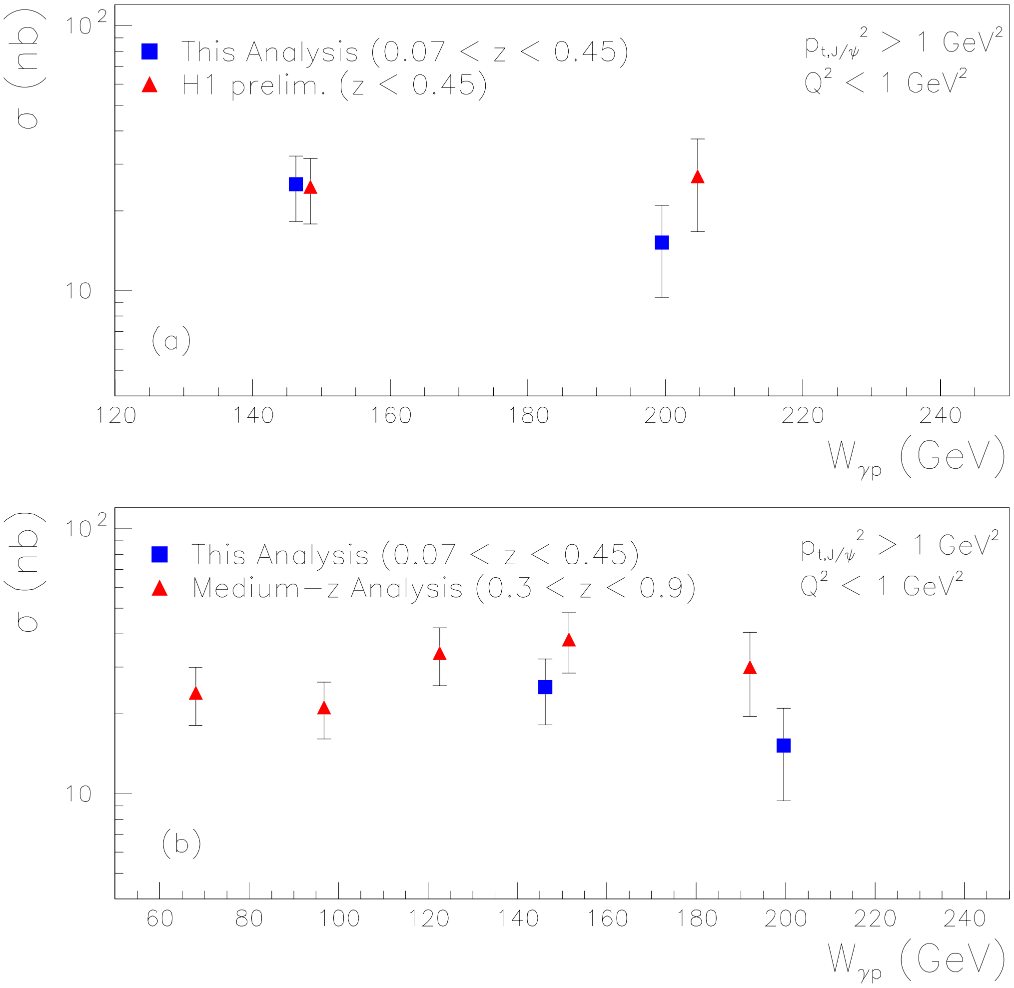

Figure 8.9: *The total photon-proton cross-section, $\sigma(\gamma p \rightarrow J/\psi X)$, as a function of $W_{\gamma p}$, measured in the kinematic range $0.07 < z < 0.45$, $p^2_{t,J/\psi} > 1$ GeV^2 and $Q^2 <$ 1 GeV^2. The results are compared with (a) preliminary results from H1 and (b) the results from the medium-z analysis.*

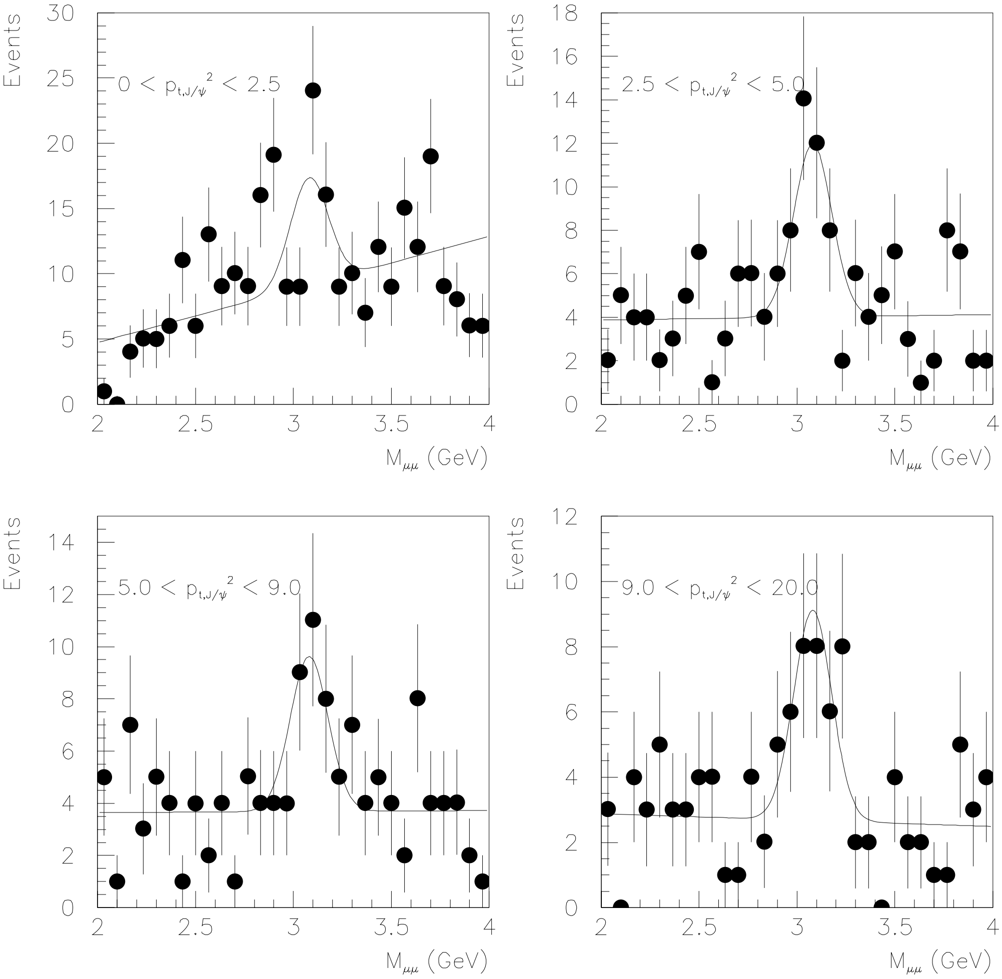

Figure 8.10: *Invariant mass spectrum of the events selected for the low-z analysis in four bins of* $p_{t,J/\psi}^2$.

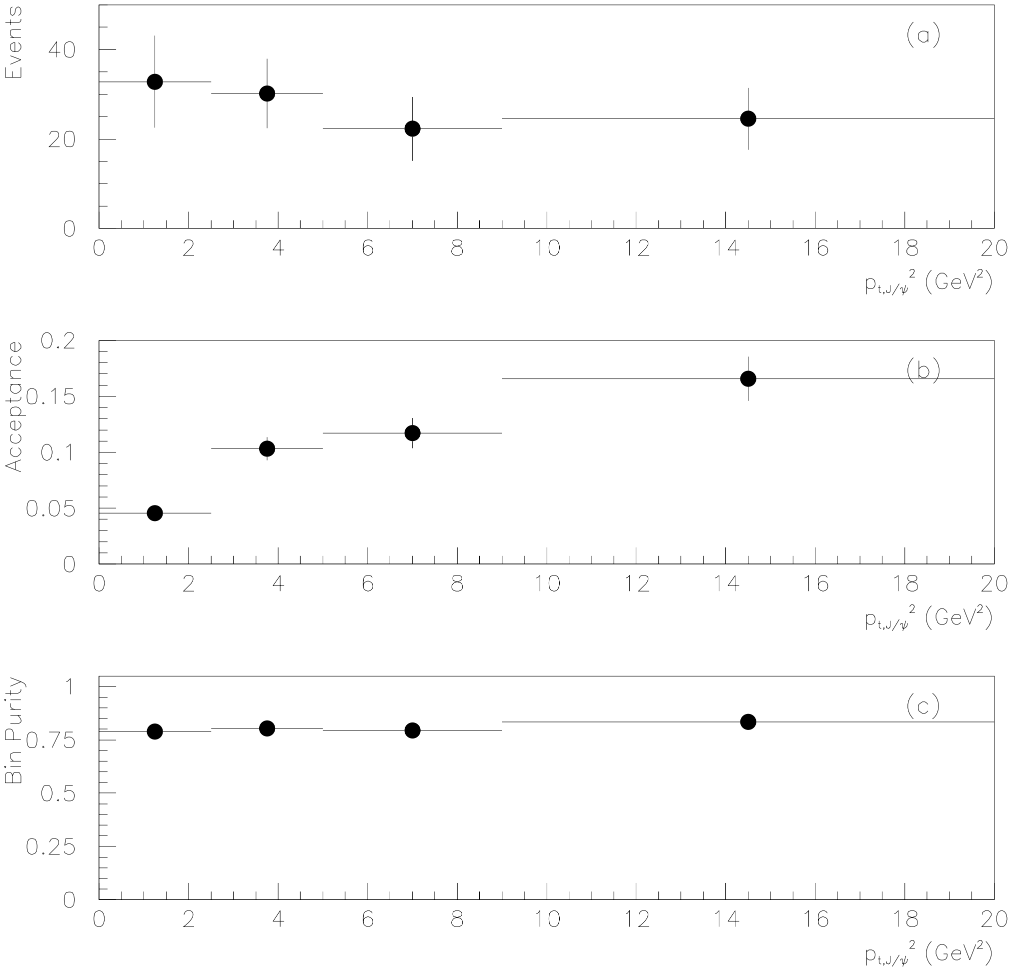

Figure 8.11: *The (a) number of events, (b) acceptance and (c) bin purity for each bin in* $p_{t,J/\psi}^2$.

in order to parameterise the shape of the $p^2_{t,J/\psi}$ distribution. They are an exponential function ($d\sigma/dp^2_{t,J/\psi} \propto e^{b.p^2_{t,J/\psi}}$) and a power law ($d\sigma/dp^2_{t,J/\psi} \propto (p^2_{t,J/\psi})^{\delta}$). Only the statistical error on the results has been taken into account due to the main systematic errors being correlated. The results of each fit are plotted in figure 8.12 and both can be seen to describe the shape of the distribution well. The parameters extracted from the fits are $b = -0.25 \pm 0.04$ and $\delta = -1.33 \pm 0.15$. In the medium-z analysis, it was found that the $p^2_{t,J/\psi}$ distribution was best described by a power law with $\delta = -1.20 \pm 0.04$ (see section 7.4). Therefore, the results of the medium and low-z analyses suggest that there is no change in the shape of the $p^2_{t,J/\psi}$ distribution with z.

8.6 Summary

The inelastic photoproduction of J/ψ mesons has been studied in the low-z kinematic region. This is a region for which there are currently no published results. Only one set of preliminary results are available, and the results presented here are in good agreement with those. The differential cross-section $d\sigma/dz$ has been measured in the region $0.07 < z < 0.45$ and is consistent with a leading-order Colour Octet model calculation. The uncertainty on the prediction for $d\sigma/dz$, due to the uncertainty in the Colour Octet matrix elements, is up to an order of magnitude. Hence these results could provide additional constraints on the Colour Octet matrix elements. However, the results are almost consistent with a leading order Colour Singlet model calculation, although this prediction also has a large uncertainty. Hence it cannot yet be concluded that there is evidence for the large colour octet contributions in the inelastic photoproduction

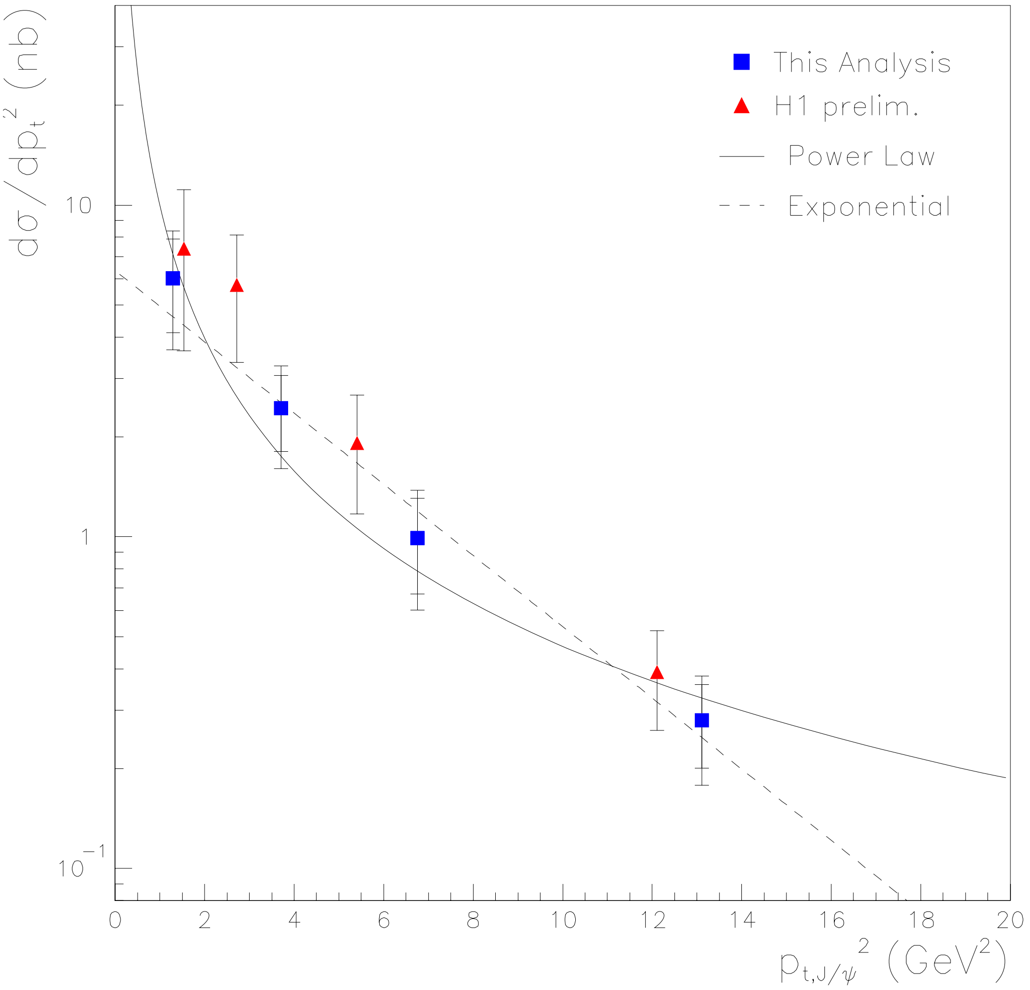

Figure 8.12: *The differential cross-section* $d\sigma/dp_{t,J/\psi}^2$ *as measured in this analysis, and from preliminary results from H1. An exponential function* ($d\sigma/dp_{t,J\psi}^2 \propto e^{b.p_{t,J\psi}^2}$) *and a power law* ($d\sigma/dp_{t,J\psi}^2 \propto (p_{t,J\psi}^2)^\delta$) *have been fitted to the results of this analysis, yielding the parameters* $b = -0.25 \pm 0.04$ *and* $\delta = -1.33 \pm 0.15$.

of J/ψ mesons that were found necessary to explain the Tevatron data.. It is clear that a next-to-leading order calculation in both models, and work to reduce the other theoretical uncertainties, is necessary before a full understanding can be reached.

The total cross-section as a function of $W_{\gamma p}$ and the differential cross-section $d\sigma/dp^2_{t,J/\psi}$ have also been measured in the low-z region. No evidence for any change in the shape of the $p^2_{t,J/\psi}$ distribution with z has been found.

Chapter 9

Summary and Conclusions

The inelastic photoproduction of J/ψ mesons has been studied in detail. Measurements have been made covering almost the full z range possible ($0.07 < z < 0.9$). It was found necessary, however, to split the z range into two regions, each covering a different $W_{\gamma p}$ range because the acceptance as a function of $W_{\gamma p}$ changes with z. The two analyses covered the kinematic ranges:

- Medium-z analysis: $0.45 < z < 0.9$, $50 < W_{\gamma p} < 220$ GeV, $p^2_{t,J/\psi} > 1$ GeV^2, and $Q^2 < 1$ GeV^2.
- Low-z analysis: $0.07 < z < 0.45$, $120 < W_{\gamma p} < 250$ GeV, $p^2_{t,J/\psi} > 1$ GeV^2, and $Q^2 < 1$ GeV^2.

In the medium-z analysis, the differential cross-sections $d\sigma/dz$ and $d\sigma/dp^2_{t,J/\psi}$, and the total photon-proton cross-section $\sigma(\gamma p \to J/\psi X)$ as a function of $W_{\gamma p}$ have been measured. Good agreement with previous results has been found and the $W_{\gamma p}$ range covered has been extended. The cross-section for the inelastic photoproduction of J/ψ's has been shown to rise more slowly with $W_{\gamma p}$ than the cross-section for the diffractive photoproduction of J/ψ's. This supports the picture of the diffractive interaction coupling more strongly to the gluon content of the proton.

Leading-order model calculations have been shown to fail in their description of the shape of the differential cross-sections. The $d\sigma/dz$ distribution is not described by a leading-order Colour Octet model calculation, whilst the $d\sigma/dp^2_{t,J/\psi}$ distribution is not described by the Colour Singlet model at leading-order. A next-to-leading order Colour Singlet model calculation does describe the shape of all three distributions ($d\sigma/dz$, $d\sigma/dp^2_{t,J/\psi}$, and $\sigma(\gamma p \rightarrow J/\psi X)$ as a function of $W_{\gamma p}$.). However there is a large uncertainty in the normalisation (a factor of ~ 3) due to the values of $\alpha_s(M_Z)$ and the charm quark mass, m_c, and the parton density functions (PDFs) used as input parameters. Whilst the results provide no evidence for large colour octet contributions of the type found necessary to explain the Tevatron data, this cannot yet be concluded as no full next-to-leading order Colour Octet model calculation exists. It would be interesting to see if this could describe the results.

The region covered by the low-z analysis is of particular interest as it is expected to have increased sensitivity to any colour octet effects. No published results exist for this region, only one set of preliminary results are currently available. The differential cross-sections $d\sigma/dz$ and $d\sigma/dp^2_{t,J/\psi}$, and the total photon-proton cross-section $\sigma(\gamma p \rightarrow J/\psi X)$ as a function of $W_{\gamma p}$ have been measured. Good agreement with the preliminary results has been found. The shape of the $d\sigma/dp^2_{t,J/\psi}$ distribution has been investigated and a power law ($d\sigma/dp^2_{t,J/\psi} \propto (p^2_{t,J/\psi})^\delta$) was found to give a good description of the distributions in both the medium and low-z analyses. The values of δ obtained were: $\delta = -1.20 \pm 0.04$ in the medium-z analysis and $\delta = -1.33 \pm 0.15$ in the low-z analysis, providing no evidence for any change in the shape of the distribution with z.

The differential cross-section $d\sigma/dz$ has been measured in the crucial low-z region. The results are consistent with the predictions from a leading-order Colour Octet model calculation. However, there is a large uncertainty on the prediction due to the uncertainty in the colour octet matrix elements. Therefore, the results presented here could be used to provide valuable constraints on the matrix elements. The results are almost consistent with the prediction from a leading-order Colour Singlet model calculation, although this is due to the large uncertainty on the prediction arising from the choice of input parameters. Hence there is no conclusive evidence for the presence of large colour octet contributions. No next-to-leading order calculation exists at low-z for either model, due to the significant contribution to the cross-section in the low-z region from resolved photon interactions. A next-to-leading order Colour Singlet model calculation could explain the data and a next-to-leading calculation is clearly necessary for both models.

Therefore it can be concluded that:

1. At leading-order, the Colour Octet model is consistent with the results at low-z but fails at medium-z.
2. At leading-order, the Colour Singlet model is almost consistent with the results at low-z but fails at medium-z.

3. At next-to-leading order, the Colour Singlet model is consistent with the results at medium-z, but is not yet available at low-z.
4. There is a clear need for a full next-to-leading order calculation covering the full z range from both models.

The inelastic photoproduction of J/ψ's is an area of active experimental and theoretical interest. The theoretical uncertainties are large and further experimental and theoretical work is necessary before a full understanding of this area of physics is obtained.

Appendix A

Summary of the Results from the Medium-z Analysis

The results of the medium-z analysis were presented in chapter 7. Here they are summarised in tabular form. The tables show the kinematic range of each bin, the number of events in the bin, the acceptance (ε), the average of the kinematic variable the measurement is as a function of, and the final result. The first error on the cross-section is statistical, the second is systematic.

z range	$N_{J/\psi}$	ε	$\langle z \rangle$	$d\sigma/dz$ (nb)
$0.3 < z < 0.45$	43.84 ± 9.31	11.3%	0.369	$19.51 \pm 4.15 \pm 4.00$
$0.45 < z < 0.57$	54.69 ± 8.72	10.6%	0.512	$32.62 \pm 5.20 \pm 6.69$
$0.57 < z < 0.69$	92.65 ± 10.32	10.8%	0.631	$53.86 \pm 6.00 \pm 11.08$
$0.69 < z < 0.8$	75.05 ± 9.07	8.7%	0.743	$59.60 \pm 7.20 \pm 12.46$
$0.8 < z < 0.9$	65.90 ± 8.49	6.4%	0.843	$77.51 \pm 9.99 \pm 19.13$

Table A.1: *Summary of the results for $d\sigma/dz$ from the medium-z analysis.*

$W_{\gamma p}$ range (GeV)	$N_{J/\psi}$	ε	$\langle W_{\gamma p} \rangle$	$\sigma_{\gamma p}$ (nb)
$50 < W_{\gamma p} < 80$	65.42 ± 8.48	5.2%	68.0 GeV	$24.00 \pm 3.11 \pm 5.00$
$80 < W_{\gamma p} < 110$	85.98 ± 10.21	13.2%	76.8 GeV	$21.19 \pm 2.52 \pm 4.44$
$110 < W_{\gamma p} < 135$	80.12 ± 9.93	13.6%	122.7 GeV	$33.89 \pm 4.20 \pm 7.20$
$135 < W_{\gamma p} < 170$	70.55 ± 9.90	10.9%	151.5 GeV	$38.28 \pm 5.37 \pm 8.18$
$170 < W_{\gamma p} < 220$	25.64 ± 6.96	5.6%	192.0 GeV	$30.09 \pm 8.16 \pm 6.60$

Table A.2: *Summary of the results for $\sigma_{\gamma p}$ from the medium-z analysis.*

$p^2_{t,j/\psi}$ range (GeV^2)	$N_{J/\psi}$	ε	$\langle p^2_{t,j/\psi} \rangle$	$d\sigma/dp^2_{t,j/\psi}$ (nb)
$0 < p^2_{t,j/\psi} < 1$	83.76 ± 10.97	3.3%	0.441 GeV^2	$19.11 \pm 2.50 \pm 6.91$
$1 < p^2_{t,j/\psi} < 1.8$	69.56 ± 9.23	6.5%	1.40 GeV^2	$10.18 \pm 1.35 \pm 2.33$
$1.8 < p^2_{t,j/\psi} < 2.7$	59.48 ± 8.69	7.5%	2.26 GeV^2	$6.67 \pm 0.97 \pm 1.39$
$2.7 < p^2_{t,j/\psi} < 4.7$	59.42 ± 8.98	9.6%	3.58 GeV^2	$2.33 \pm 0.35 \pm 0.48$
$4.7 < p^2_{t,j/\psi} < 8$	46.82 ± 8.03	11.6%	6.05 GeV^2	$0.926 \pm 0.159 \pm 0.190$
$8 < p^2_{t,j/\psi} < 12.5$	44.92 ± 7.48	16.1%	10.21 GeV^2	$0.470 \pm 0.078 \pm 0.097$
$12.5 < p^2_{t,j/\psi} < 17$	26.24 ± 5.67	15.0%	14.89 GeV^2	$0.294 \pm 0.064 \pm 0.061$

Table A.3: *Summary of the results for $d\sigma/dp^2_{t,J/\psi}$ from the medium-z analysis.*

Appendix B

Summary of the Results from the Low-z Analysis

The results of the medium-z analysis were presented in chapter 8 and are summarised here in tabular form. The tables show the kinematic range of each bin, the number of events, the acceptance (ε), the average of the kinematic variable the measurement is as a function of, and the cross-section. The first error on the cross-section is statistical, the second is systematic.

z range	$N_{J/\psi}$	Acceptance	$\langle z \rangle$	$d\sigma/dz$ (nb)
$0.07 < z < 0.18$	46.69 ± 10.30	12.4%	0.124	$71.19 \pm 15.71 \pm 16.04$
$0.18 < z < 0.3$	32.71 ± 8.33	10.5%	0.243	$54.12 \pm 13.78 \pm 12.29$
$0.3 < z < 0.45$	23.99 ± 6.94	7.7%	0.359	$43.27 \pm 12.52 \pm 9.74$

Table B.1: *Summary of the results for $d\sigma/dz$ from the low-z analysis.*

$W_{\gamma p}$ range (GeV)	$N_{J/\psi}$	ε	$\langle W_{\gamma p}\rangle$	$\sigma_{\gamma p}$ (nb)
$120 < W_{\gamma p} < 170$	71.17 ± 11.43	10.6%	146.3 GeV	$25.20 \pm 4.05 \pm 5.73$
$170 < W_{\gamma p} < 250$	32.42 ± 9.64	10.0%	199.5 GeV	$15.19 \pm 4.52 \pm 3.62$

Table B.2: *Summary of the results for* $\sigma_{\gamma p}$ *from the low-z analysis.*

$p^2_{t,j/\psi}$ range (GeV^2)	$N_{J/\psi}$	ε	$\langle p^2_{t,j/\psi}\rangle$	$d\sigma/dp^2_{t,j/\psi}$ (nb)
$0 < p^2_{t,j/\psi} < 2.5$	32.81 ± 10.30	4.5%	1.29 GeV^2	$6.01 \pm 1.89 \pm 1.39$
$2.5 < p^2_{t,j/\psi} < 5$	30.20 ± 7.78	10.3%	3.71 GeV^2	$2.44 \pm 0.63 \pm 0.55$
$5 < p^2_{t,j/\psi} < 9$	22.30 ± 7.15	11.7%	6.75 GeV^2	$0.990 \pm 0.318 \pm 0.226$
$9 < p^2_{t,j/\psi} < 20$	24.51 ± 6.88	16.6%	13.11 GeV^2	$0.280 \pm 0.079 \pm 0.064$

Table B.3: *Summary of the results for* $d\sigma/dp^2_{t,J/\psi}$ *from the low-z analysis.*

Bibliography

[1] H1 Collab., “Inelastic Photoproduction of J/psi at low z ”, contributed paper 314 to the XXX ICHEP Conference, Osaka, Japan (2000).

[2] E. Rutherford, Phil. Mag. **21** (1911) 669.

[3] M. Breidenbach *et al.*, Phys. Rev. Lett. **23** (1969) 935.

[4] S. Weinberg, Phys. Rev. Lett. **19** (1967) 1264,

A. Salem, p. 367 of “Elemetary Particle Theory”, ed. N. Svartholm (Almquist and Wiksells, Stockhom, 1969),

S. L. Glashow, J. Iliopoulos and L. Maiani, Phys. Rev. D **2** (1970) 1285.

[5] H. Fritzsch, M. Gell-Mann and H. Leutwyler, Phys. Lett. B **47** (1973) 365.

[6] M. Gell-Mann, Phys. Lett. **8** (1964) 214,

G. Zweig, “An SU(3) Model For Strong Interaction Symmetry And Its Breaking. 2,” CERN-TH-412.

[7] R. P. Feynman, Phys. Rev. Lett. **23** (1969) 1415.

[8] J. D. Bjorken and E. A. Paschos, Phys. Rev. **185** (1969) 1975.

[9] J. D. Bjorken, Phys. Rev. **179** (1969) 1547.

[10] C. G. Callan and D. J. Gross, Phys. Rev. Lett. **22** (1969) 156.

[11] V. N. Gribov and L. N. Lipatov, Yad. Fiz. **15** (1972) 781.

G. Altarelli and G. Parisi, Nucl. Phys. B **126** (1977) 298.

[12] C. Adloff *et al.* [H1 Collaboration], hep-ex/0012053.

[13] M. Arneodo *et al.* [NMC Collaboration], Phys. Lett. B **309** (1993) 222.

[14] A. C. Benvenuti *et al.* [BCDMS Collaboration], Phys. Lett. B **223** (1989) 485.

[15] C. Adloff *et al.* [H1 Collaboration], Eur. Phys. J. C **19** (2001) 269.

[16] C. Adloff *et al.* [H1 Collaboration], Z. Phys. C **76** (1997) 613.

[17] C. Adloff *et al.* [H1 Collaboration], Phys. Lett. B **467** (1999) 156.

[18] C. Adloff *et al.* [H1 Collaboration], Nucl. Phys. B **545** (1999) 21.

[19] S. Aid *et al.* [H1 Collaboration], Nucl. Phys. B **470** (1996) 3.

[20] H. L. Lai *et al.*, Phys. Rev. D **55** (1997) 1280.

[21] C. Adloff *et al.* [H1 Collaboration], Phys. Lett. B **479** (2000) 358.

[22] C. Adloff *et al.* [H1 Collaboration], Eur. Phys. J. C **5** (1998) 575.

[23] J. J. Aubert *et al.*, Phys. Rev. Lett. **33**, (1974) 1404.

[24] J. E. Augustin *et al.*, Phys. Rev. Lett. **33** (1974) 1406.

[25] G. S. Abrams *et al.*, Phys. Rev. Lett. **33** (1974) 1453.

[26] D. E. Groom *et al.* [Particle Data Group Collaboration], Eur. Phys. J. C **15** (2000) 1.

[27] G. Zweig, "An SU(3) Model For Strong Interaction Symmetry And Its Breaking. 2," CERN-TH-412,

J. Iizuka, Prog. Theor. Phys. Suppl. **37-38** (1966) 21.

[28] T. Ahmed *et al.* [H1 Collaboration], Phys. Lett. B **338** (1994) 507.

[29] S. Aid *et al.* [H1 Collaboration], Nucl. Phys. B **468** (1996) 3.

[30] S. Aid *et al.* [H1 Collaboration], Nucl. Phys. B **472** (1996) 3.

[31] C. Adloff *et al.* [H1 Collaboration], Phys. Lett. B **421** (1998) 385.

[32] C. Adloff *et al.* [H1 Collaboration], Eur. Phys. J. C **10** (1999) 373.

[33] C. Adloff *et al.* [H1 Collaboration], Phys. Lett. B **483** (2000) 23.

[34] E. L. Berger and D. Jones, Phys. Rev. D **23** (1981) 1521.

[35] B. Guberina, J. H. Kuhn, R. D. Peccei and R. Ruckl, Nucl. Phys. B **174** (1980) 317.

[36] W. Keung, Phys. Rev. D **23** (1981) 2072,

J. H. Kuhn and H. Schneider, Z. Phys. C **11** (1981) 263.

[37] G. A. Schuler, "Quarkonium production and decays," hep-ph/9403387.

[38] E. Braaten, S. Fleming and T. C. Yuan, Ann. Rev. Nucl. Part. Sci. **46** (1996) 197.

[39] S. Aid *et al.* [H1 Collaboration], "Diffractive and Non-diffractive Photo-production of J/ψ at HERA", contributed paper pa02-085 to ICHEP 1996, Warsaw.

[40] J. Breitweg *et al.* [ZEUS Collaboration], Z. Phys. C **76** (1997) 599.

[41] M. Kramer, Nucl. Phys. B **459** (1996) 3.

[42] M. Cacciari and M. Kramer, Phys. Rev. Lett. **76** (1996) 4128.

[43] R. Barbieri, R. Gatto and E. Remiddi, Phys. Lett. B **61** (1976) 465,

R. Barbieri, M. Caffo, R. Gatto and E. Remiddi, Nucl. Phys. B **192** (1981) 61.

[44] C. Albajar *et al.* [UA1 Collaboration], Phys. Lett. B **256** (1991) 112.

[45] F. Abe *et al.* [CDF Collaboration], Phys. Rev. Lett. **69** (1992) 3704.

[46] M. W. Bailey [CDF Collaboration], "Charmonium and bottomonium production in p anti-p collisions at CDF," hep-ex/9608014.

[47] A. Sansoni [CDF Collaboration], Nucl. Phys. A **610** (1996) 373C.

[48] F. Abe *et al.* [CDF Collaboration], Phys. Rev. Lett. **79** (1997) 572.

[49] F. Abe *et al.* [CDF Collaboration], Phys. Rev. Lett. **79** (1997) 578.

[50] T. Affolder *et al.* [CDF Collaboration], Phys. Rev. Lett. **85** (2000) 2886.

[51] S. Abachi *et al.* [D0 Collaboration], Phys. Lett. B **370** (1996) 239.

[52] B. Abbott *et al.* [D0 Collaboration], Phys. Rev. Lett. **82** (1999) 35.

[53] M. Beneke and M. Kramer, Phys. Rev. D **55** (1997) 5269.

[54] F. Abe *et al.* [CDF Collaboration], Phys. Rev. Lett. **75** (1995) 1451.

[55] G. T. Bodwin, E. Braaten and G. P. Lepage, Phys. Rev. D **46** (1992) 1914.

[56] G. T. Bodwin, E. Braaten, T. C. Yuan and G. P. Lepage, Phys. Rev. D **46** (1992) 3703.

[57] G. T. Bodwin, E. Braaten and G. P. Lepage, Phys. Rev. D **51** (1995) 1125.

[58] M. Beneke, "Nonrelativistic effective theory for quarkonium production in hadron collisions," hep-ph/9703429.

[59] W. E. Caswell and G. P. Lepage, Phys. Lett. B **167** (1986) 437.

[60] G. T. Bodwin, D. K. Sinclair and S. Kim, Phys. Rev. Lett. **77** (1996) 2376

[61] M. Kramer, private communication, April 2001.

[62] A. K. Leibovich, Nucl. Phys. Proc. Suppl. **93** (2001) 182.

[63] R. Barbieri, R. Gatto, R. Kogerler and Z. Kunszt, Phys. Lett. B **57** (1975) 455, Nucl. Phys. B **105** (1976) 125.

[64] P. Cho and A. K. Leibovich, Phys. Rev. D **53** (1996) 150, Phys. Rev. D **53** (1996) 6203

[65] J. K. Mizukoshi, "The paradox of charmonium production," hep-ph/9911384.

[66] A. D. Martin, R. G. Roberts and W. J. Stirling, Phys. Lett. B **387** (1996) 419.

[67] M. Gluck, E. Reya and A. Vogt, Z. Phys. C **67** (1995) 433.

[68] B. Cano-Coloma and M. A. Sanchis-Lozano, Nucl. Phys. B **508** (1997) 753 and Phys. Lett. B **406** (1997) 232.

[69] T. Sjostrand, Comput. Phys. Commun. **82** (1994) 74.

[70] A. D. Martin, W. J. Stirling and R. G. Roberts, Phys. Rev. D **47** (1993) 867.

[71] E. Braaten, B. A. Kniehl and J. Lee, Phys. Rev. D **62** (2000) 094005

[72] B. A. Kniehl and G. Kramer, Eur. Phys. J. C **6** (1999) 493.

[73] M. A. Sanchis-Lozano, Nucl. Phys. Proc. Suppl. **86** (2000) 543.

[74] A. D. Martin, R. G. Roberts, W. J. Stirling and R. S. Thorne, Eur. Phys. J. C **4** (1998) 463.

[75] H. L. Lai *et al.* [CTEQ Collaboration], Eur. Phys. J. C **12** (2000) 375.

[76] J. Botts, J. G. Morfin, J. F. Owens, J. Qiu, W. Tung and H. Weerts [CTEQ Collaboration],Phys. Lett. B **304** (1993) 159.

[77] M. Beneke and I. Z. Rothstein, Phys. Rev. D **54** (1996) 2005 [Erratum: *ibid* D **54** (1996) 7082].

[78] M. Beneke, M. Kramer and M. Vanttinen, Phys. Rev. D **57** (1998) 4258.

[79] C. G. Boyd, A. K. Leibovich and I. Z. Rothstein, Phys. Rev. D **59** (1999) 054016.

[80] A. Meyer, "Charmonium production in deep inelastic scattering at HERA," DESY-THESIS-1998-012.

[81] M. Gluck, E. Reya and A. Vogt, Phys. Rev. D **46** (1992) 1973.

[82] P. Hagler, R. Kirschner, A. Schafer, L. Szymanowski and O. V. Teryaev, Phys. Rev. Lett. **86** (2001) 1446.

[83] P. Hagler, R. Kirschner, A. Schafer, L. Szymanowski and O. V. Teryaev, Phys. Rev. D **63** (2001) 077501

[84] "GEANT - Detector Description and Simulation Tool", *CERN Program Library Long Writeup W5013*.

[85] H. Jung, "The Monte Carlo Generator EPJPSI For J/ψ Mesons In High-Energy Electron Proton Collisions," *Aachen Tech. Hochsch. - PITHA-92-10 (92/04,rec.Apr.) 10 p.*

[86] H. Jung, D. Krucker, C. Greub and D. Wyler, Z. Phys. C **60** (1993) 721.

[87] A. D. Martin, W. J. Stirling and R. G. Roberts, Phys. Lett. B **354** (1995) 155.

[88] H. Plothow-Besch, Int. J. Mod. Phys. A **10** (1995) 2901.

[89] B. List, "Diffraktive J/ψ-Produktion in Elektron-Proton-Stössen am Speicherring HERA", Diploma-Thesis, Techn. Univ. Berlin, unpublished (1993).

[90] H. Abramowicz, E. M. Levin, A. Levy and U. Maor, Phys. Lett. B **269** (1991) 465,

A. Donnachie and P. V. Landshoff, Phys. Lett. B **296** (1992) 227.

[91] J. J. Sakurai, Annals Phys. **11** (1960) 1,

J. J. Sakurai, Phys. Rev. Lett. **22** (1969) 981,

J. J. Sakurai and D. Schildknecht, Phys. Lett. B **40** (1972) 121,

T. H. Bauer, R. D. Spital, D. R. Yennie and F. M. Pipkin, Rev. Mod. Phys. **50** (1978) 261; Erratum ibid **51** (1979) 407.

[92] I. Abt *et al.* [H1 Collaboration], Nucl. Instrum. Meth. A **386** (1997) 310 and 348.

[93] [H1 Collaboration.], "Technical proposal to upgrade the backward scattering region of the H1 detector," *Hamburg DESY - PRC 93-02 (93/03,rec.Dec.) 142 p.*

[94] D. Pitzl *et al.*, "The H1 silicon vertex detector," Nucl. Instrum. Meth. A **454** (2000) 334.

[95] W. Eick *et al.*, Nucl. Instrum. Meth. A **386** (1997) 81.

[96] B. Andrieu *et al.* [H1 Calorimeter Group Collaboration], Nucl. Instrum. Meth. A **336** (1993) 460.

[97] T. Nicholls *et al.* [H1 SPACAL Group Collaboration], Nucl. Instrum. Meth. A **374** (1996) 149.

[98] R. D. Appuhn *et al.* [H1 SPACAL Group Collaboration], DESY-96-013.

[99] P. Biddulph *et al.*, Nucl. Instrum. Meth. A **340** (1994) 304.

[100] H1 Collab., S. Aid et al., "Luminosity Measurement in the H1 Experiment at HERA"', contributed paper pa17-026 to ICHEP 1996, Warsaw.

[101] H. Bethe, W. Heitler, Proc. Roy. Soc. A **146** (1934) 83.

[102] E. Elsen, "Aspects of the H1 trigger and data acquisition system," *Prepared for 2nd Annual Conference on Electronics for Future Colliders, Chestnut Ridge, N.Y., 19-21 May 1992.*

F. Sefkow, E. Elsen, H. Krehbiel, U. Straumann and J. Coughlan, IEEE Trans. Nucl. Sci. **42** (1995) 900.

[103] J. C. Bizot et al., 'Status of Simulation for a Topological Level 2 Trigger', H1 Internal Note 92-212

J. C. Bizot et al., 'Strategy Studies for the H1 Topological L2-Trigger (L2TT)'. H1 Internal Note 97-508

[104] J. K. Kohne *et al.*, Nucl. Instrum. Meth. A **389** (1997) 128.

[105] S. Eichenberger, "A Fast pipelined trigger for the H1 experiment at HERA based on multiwire proportional chamber signals," *Preprint - Eichenberger, S. (93,rec.Feb.94) 130 p.*

[106] T. Ahmed *et al.*, Nucl. Instrum. Meth. A **364** (1995) 456.

[107] [H1 Collaboration], "$e - p$ Physics Beyond 1999", H1 Internal Note **97-531**.

[108] W. Braunschweig *et al.*, [H1 Collaboration], "A Forward Silicon Tracker for H1", H1 Internal Note **99-563**.

[109] T. Greenshaw *et al.*, [H1 Collaboration], "Proposal for an Upgrade of the H1 Forward Track Detector for HERA 2000", **PRC 98/06**.

[110] M. Cuje *et al.*, [H1 Collaboration], "H1 High Luminosity Upgrade 2000 CIP and Level 1 vertex Trigger", H1 Internal Note **98-535**.

[111] Joint Institute for Nuclear Research, Dubna, "Upgrade of the H1 Hadron PLUG Calorimeter", First draft of proposal 1998.

[112] T. Carli *et al.*, [H1 Collaboration], "Proposal to Upgrade the LAr Calorimeter Trigger: The Jet Trigger", H1 Internal Note **99-560**.

[113] S. A. Baird *et al.*, [H1 Collaboration], "A Fast Track Trigger with High Resolution for H1", **PRC 99/06**.

[114] A. Campbell *et al.*, [H1 Collaboration], "Proposal to Merge Level-4 and Level-5 Systems of the H1 Experiment", **PRC 99/03**.

[115] S. Mohrdieck, "Neuronaler Netzwerk-Trigger fuer Myonen im H1-Detektor bei HERA", Diploma Thesis, Univ. Ham. 1997

[116] B. Naroska, S. Schiek, and G. Schmidt, "Lepton Identification in the H1 Detector at Low Momenta", H1 Internal Note **97-518**.

[117] S. Bentvelsen, J. Engelen and P. Kooijman, "Reconstruction of (x, Q**2) and extraction of structure functions in neutral current scattering at HERA," NIKHEF-H-92-02.

[118] A. Blondel and F. Jacquet, *In *Hamburg 1979, Proceedings, Study Of An E P Facility For Europe*, Hamburg 1979, 391.*

[119] P. Merkel, "Diffractive photoproduction of heavy vector mesons at HERA," DESY-THESIS-1999-030.

[120] S. Levonian, H1 Internal Communication, 1997.

[121] A. Schwank, "Effizienzbestimmung von Detektorkomponenten des H1-Experiments mit Hilfe kosmischer Strahlung", Diploma Thesis, Univ. Ham. 1998.

[122] K. Daum and G. Eckerlin, H1 Weekly Meeting, 22/2/2001.

[123] J. Smith, "An Experimentalist's Guide To Photon Flux Calculations", H1 Internal Note **92-259**.

[124] C. F. von Weizsacker, Z. Phys. **88** (1934) 612.

E. J. Williams, Phys. Rev. **45** (1934) 729.

[125] V. M. Budnev, I. F. Ginzburg, G. V. Meledin and V. G. Serbo, Phys. Rept. **15** (1974) 181.

[126] H1 Collab., "Inelastic Photoproduction of J/Psi and Psi(2s)", contributed paper 157aj to International Europhysics Conference on High Energy Physics (HEP99), Tampere, Finland, 1999

[127] ZEUS Collaboration, contributed paper 446 to the XXX ICHEP Conference, Osaka, Japan (2000).

[128] M. Kramer, J. Zunft, J. Steegborn and P. M. Zerwas, Phys. Lett. B **348**, 657 (1995).

[129] M. Kramer, private communication, May 2001.